MRI Fat Quantification

A Phase Sweep b-SSFP Approach

by

Sarah Larmour

A thesis submitted in partial fulfillment of the requirements for the degree of

Master of Science

Department of Biomedical Engineering
University of Alberta

Abstract

Fats are a fundamental building block of the human body, but accumulation of unwanted fat in and around tissues is a common pathology related to many disease mechanisms. Magnetic Resonance Imaging (MRI) offers a host of methods to differentiate water and fat signals in images or spectra, for both high fat content visceral and adipose fat, and the lower concentration intra-cellular fat pools. Accurate quantitative measurements of small fat concentrations and small changes in fat concentration within the heart and liver would enable the early detection of disease, evaluation of disease progression, and assessment of the effectiveness of prescribed treatments. Current methods, such as Dixon fat-water methods, have poor performance at low fat-fraction (FF), while ^{1}H Nuclear Magnetic Resonance (NMR) spectroscopy methods are difficult to apply in the heart, and are not widely available.

The goals of this thesis were primarily to develop and validate a new method called Phase Sweep b-SSFP for the simultaneous quantification of FF, water T_1 and T_2, and off-resonance frequency using multiple b-SSFP images with incremented radio frequency (RF) pulse phase (Phase Sweep b-SSFP), and secondly to characterize the effects of fat on commonly used T_1 mapping sequences and evaluate a new method for quantitative FF imaging, based on the modulation of T_1 values by the fat pool.

For the purpose of validation of these methods, the proposed work on fat quantification addressed accuracy and precision for the case of small concentrations of fat in the 0 – 10% range. Methods included numerical simulations, phantom experiments and application in skeletal muscle for validation. This range reflects the intended future clinical application of the

techniques in the heart, kidney and liver to provide early diagnosis of disease and assessment of prescribed treatment effectiveness. Skeletal muscle provides a good surrogate for the diffuse and heterogeneous fat deposits found in the heart, kidney and liver while allowing us to develop methods without the added complication of excessive movement and need for free breathing pulse sequences.

The results of this work show that 1) by using the proposed Phase Sweep b-SSFP method it is feasible to acquire quantitative results for FF, water T_1 and T_2 and off-resonance frequency, for which the variability in each parameter is largely independent of all other parameters and 2) low FF in tissues result in relatively large negative or positive shifts in native tissue T_1 measured with MOLLI and SASHA T_1 mapping methods as a function of off-resonance frequency, and that these resulting T_1 shifts can be used to accurately quantify FF.

Preface

This thesis is an original work by Sarah Larmour. All research subjects provided written informed consent and the study was approved by the University of Alberta Health Research Ethics Board, Development of Cardiovascular Magnetic Resonance Imaging, Pro00001460.

Chapter 3 of this thesis will be submitted for publication as S. Larmour, K. Chow, P. Kellman, and R.B. Thompson, "Simultaneous Quantification of Fat Fraction, Water T_1 and T_2, and Off Resonance Frequency Using Phase Sweep b-SSFP" to the Journal of Magnetic Resonance in Medicine. I was responsible for the data collection and analysis as well as the manuscript composition. K. Chow assisted with the data collection of spin echo phantom data and contributed to manuscript edits, P. Kellman assisted with VARPRO data analysis and manuscript edits, and R.B. Thompson was the senior author and was involved with concept formation and manuscript composition.

Chapter 4 of this thesis has been submitted for publication as S. Larmour, K. Chow, P. Kellman, and R.B. Thompson, "Characterization of T_1 Bias from Fat in MOLLI and SASHA Pulse Sequences: Quantitative Fat-Fraction Imaging with T_1 Mapping" to the Journal of Magnetic Resonance in Medicine. I was responsible for the data collection and analysis as well as the manuscript composition. K. Chow contributed to manuscript edits, P. Kellman assisted with VARPRO data analysis and manuscript edits, and R.B. Thompson was the senior author and was involved with concept formation and manuscript composition.

Acknowledgments

I would like to acknowledge financial support provided throughout my degree by the Natural Sciences and Engineering Research Council (NSERC), the province of Alberta, the University of Alberta, and the Department of Biomedical Engineering. Funding for operational grants has been provided by CIHR, MOP 106551 and NSERC, RGPIN 327499.

I would also like to acknowledge the many volunteers without whom this work would not be possible. Thank-you for taking valuable time out of your schedules to forward this research.

Over the two years of my MSc. program I have been very lucky to be surrounded by many friendly and helpful peers. This positive environment greatly contributed to my experience and the quality of my research as I knew a listening ear, sharp mind, and often even a solution to my latest problem were only a few paces away. I would especially like to mention those within my lab whom I have spent the most time getting to know – Joe Pagano, Kelvin Chow, and Kory Mathewson, to whom I am eternally grateful for helping me every step of the way from simulation to data collection to paper revisions.

I would also like to thank my supervisor Dr. Richard Thompson who saw potential in me, despite my lack of MRI background, and was able to help me slowly build up a foundation of MRI knowledge, as well as develop research, scientific writing, and MATLAB programing skills. I will carry these skills with me into my future endeavors and am extremely grateful for your mentorship, trust, and genuine excitement about my project all the way through. Thank you also to the other members of my supervisory committee, Nicola De Zanche and Atiyah Yahya, whom provided many insights and helpful feedback on this work as well as Dr. Peter Kellman who directly collaborated with me on this work; your involvement and expertise have greatly influenced the quality and impact of this research.

I also need to thank my family. Thank-you to my two sisters and to my parents for always asking about my research, for listening to the long version even though they may have preferred the short one, for sending me home time and again with plates of delicious homemade food, and for always supporting me in every decision I make and challenge I face. Finally, a colossal thank-you to my husband Donny for all the faith he has had in me, for the sacrifices he has made, and for always being my best friend and greatest support through the best and worst of times.

Table of Contents

List of Figures

List of Abbreviations

AFD - Anderson Fabry Disease

b-SSFP - Balanced Steady State Free Precession

CMR - Cardiac Magnetic Resonance

ECG - Electrocardiogram

ECV - Extracellular Volume fraction

EMCF - Extra-myocellular Fat

FF - Fat Fraction

GAS - Gastroc

GRE - Gradient Echo Imaging

IMCF - Intra-myocellular Fat

MOLLI - MOdified Look-Locker Inversion

MR - Magnetic Resonance

MRI - Magnetic Resonance Imaging

MRS - Magnetic Resonance Spectroscopy

NMR - Nuclear Magnetic Resonance

RF - Radio Frequency

ROI - Region Of Interest

SASHA - SAturation recovery single-SHot Acquisition

SAT - Subcutaneous Adipose Tissue

SNR - Signal to Noise Ratio

SOL - Soleus

TA - Tibialis Anterior

TE	- Echo Time
TI	- Inversion Time
TR	- Repetition Time
TS	- Saturation Recovery Time
VARPRO	- VARiable PROjection water/fat estimation
VAT	- Visceral Adipose Tissue
VFA	- Variable Flip Angle

List of Symbols

B_0 - Main magnetic field

I - Image

f - Frequency (Hz)

M - Magnetization

M_0 - Equilibrium Magnetization

n - Integer

P - Simulated Signal

r - Spatial position

R_1 - Longitudinal relaxation rate

R_2 - Transverse relaxation rate

S - Acquired Signal

t - Time

T_1 - Longitudinal relaxation time constant

T_1* - Apparent longitudinal relaxation time constant

T_2 - Transverse relaxation time constant

α - Magnetization flip angle

Δf_{cs} - Chemical shift (Hz)

$\Delta\delta$ - Chemical shift (ppm)

η - Saturation efficiency

γ - Gyromagnetic ratio

ω - Frequency (rad/s)

ϕ - Phase

τ - Molecular motion correlation time

Subscripts

z - Longitudinal

xy - Transverse

F - Fat

W - Water

Chapter 1. Introduction

1.1 Overview

Cardiac Magnetic Resonance (CMR) is routinely used in the diagnosis of disease, and monitoring disease progression through analysis of heart function and morphology. However, many diseases do not result in visually apparent abnormalities in structure or function until the later stages of disease progression. This realization has led to a recent focus on Magnetic Resonance (MR) studies that aim to provide information on the microscopic myocardial tissue environment in the early stages of disease progression. MR signal intensities are governed by intrinsic tissue characteristics that are dependent on their environment and can change with disease. The microscopic myocardial tissue environment may be characterized with Magnetic Resonance Imaging (MRI) by in-vivo quantification of relaxation time constants (T_1 and T_2), and changes in FF.

For example, quantitative imaging of myocardial T_1 is increasingly used in clinical research to evaluate pathology related to edema (1) and fibrosis (2), where changes in T_1 values reflect changes in the water mobility in these environments. Quantitative imaging of T_2 is also being used in identifying edema and hemorrhage (3).

The hydrogen atoms (protons) in our bodies which give rise to the observed NMR signal are contained largely in water molecules, however, fats and proteins also contain hydrogen atoms and can contribute to this signal and allow us to investigate the dependence of disease on tissue composition. Fat accumulation in tissues is a feature related to common diseases such as obesity (4), and type 2 diabetes (4) which is apparent in the early stages of disease progression.

The focus of this thesis is the development of new MRI sequences capable of quantifying fat fraction (FF). The methods developed are specifically designed so that they can be used for analysis of low FF in organs such as the heart (5), kidney(6), pancreas (7), and liver (8) where the early identification of fat accumulation will have the greatest clinical impact on diagnosing and monitoring disease progression.

Chapter 2 provides background information on: body fat and why it is important in the analysis of disease, relaxation parameters T_1 and T_2, the rapid pulse sequence called balanced Steady State Free Precession (b-SSFP) used in the proposed methods, as well as current water-fat imaging and T_1 mapping methods. Chapter 3 describes and validates a new multi-parameter imaging method that provides quantitative measurement of FF, tissue T_1 and T_2, and off-resonance. Chapter 4 investigates errors in conventional T_1 mapping methods due to the presence of fat signals, which gone unnoticed may lead to erroneous interpretation and diagnosis, as well as a new method for the quantification of FF from the effects of fat on the T_1 values.

The presented methods have been designed with a full consideration of the NMR physics that govern the response of the complex water and fat spin systems to NMR pulse sequences. While all in-vivo data presented is from skeletal muscle (a good model for organs with low FF) all methods were designed to be compatible with free breathing techniques that may be implemented in the heart and other organs that have significant motion with breathing and/or cardiac cycle motion. All developmental and validation work took place on clinical-style MRI scanner in the Peter S Allen MRI Centre at the University of Alberta MRI Facility, which will accommodate the translation of these methods to the clinical environment.

1.2 Thesis Statement

The primary aim of my thesis was to develop and validate a robust and accurate method for the quantification of relatively low (0-10%) fat fractions in and around tissues using a b-SSFP pulse sequence. This sequence offers high signal yield and rapid imaging which are enabling features for the detection of low fat density signals in moving organ systems. Further goals were the additional and simultaneous quantification of water T_1 and T_2, and off-resonance frequency, using similar b-SSFP based methods. A final aim of my thesis was to quantify biases in conventional MOLLI and SASHA T_1 mapping methods due to the presence of fat and develop and validate a new method of FF quantification based on the characterized T_1 bias.

1.3 Chapter 1 References

1. Ferreira VM, Piechnik SK, Dall'Armellina E, Karamitsos TD, Francis JM, Choudhury RP, Friedrich MG, Robson MD, Neubauer S. Non-contrast T1-mapping detects acute myocardial edema with high diagnostic accuracy: a comparison to T2-weighted cardiovascular magnetic resonance. Journal of Cardiovascular Magnetic Resonance 2012;14(1):42-42.

2. Bull S, White SK, Piechnik SK, Flett AS, Ferreira VM, Loudon M, Francis JM, Karamitsos TD, Prendergast BD, Robson MD, Neubauer S, Moon JC, Myerson SG. Human non-contrast T1 values and correlation with histology in diffuse fibrosis. Heart 2013;99(13):932-937.

3. Zia MI, Ghugre NR, Connelly KA, Strauss BH, Sparkes JD, Dick AJ, Wright GA. Characterizing Myocardial Edema and Hemorrhage Using Quantitative T2 and T2* Mapping at Multiple Time Intervals Post ST-Segment Elevation Myocardial Infarction. Circulation: Cardiovascular Imaging 2012;5(5):566-572.

4. Goodpaster BH, Wolf D. Skeletal muscle lipid accumulation in obesity, insulin resistance, and type 2 diabetes. Pediatric Diabetes 2004;5(4):219-226.

5. Burke AP, Farb A, Tashko G, Virmani R. Arrhythmogenic Right Ventricular Cardiomyopathy and Fatty Replacement of the Right Ventricular Myocardium: Are They Different Diseases? Circulation 1998;97(16):1571-1580.

6. Foster MC, Hwang SJ, Porter SA, Massaro JM, Hoffmann U, Fox CS. Fatty kidney, hypertension, and chronic kidney disease: the Framingham Heart Study. Hypertension 2011;58(5):784-790.

7. Calculli L, Festi D, Pezzilli R. Enlarged pancreas: not always a cancer. Hepatobiliary & pancreatic diseases international : HBPD INT 2015;14(1):107-108.

8. Farrell GC, Larter CZ. Nonalcoholic fatty liver disease: From steatosis to cirrhosis. Hepatology 2006;43(S1):S99-S112.

Chapter 2. Background

2.1 Body Fat Distribution

Total body fat can be broken into two main categories. The first category is adipose tissue and the second category is ectopic fat. White adipose tissue includes subcutaneous adipose tissue (SAT), and interstitial or visceral adipose tissue (VAT) which is found intra-abdominally often around organs. Ectopic fat is fat that accumulates in the cells of non-adipose tissues such as in the heart, pancreas, liver, and skeletal muscle. Ectopic fat deposits form when, due to increased fatty acids in systemic circulation, triglycerides accumulate in fat droplets in non-adipose tissues (9). These non-adipose tissues normally contain small amounts of fat and can become dysfunctional when excessive amounts of fat accumulate (10).

Extra-myocellular fat (EMCF) is adipose tissue typically found around groups of muscle cells (11) and in fasciae (12). While all muscle has some amount of EMCF, the accumulation of excess fat in this pool is found in important and common pathologies. For example increased EMCF deposition has been observed in advanced cases of Duchenne muscular dystrophy (13), obesity (4), type 2 diabetes (4) and aged muscle (14). In addition to disease, intramuscular extracellular fat deposits have also been observed in response to human injury such as the fatty degeneration seen in the muscle around tendon fibers and vessels following rotator cuff tears (15,16) and have been associated with a decrease in the function (retraction) of tendon fibers (16). With MRI we cannot distinguish between EMCF that accumulates in the muscle and intra-myocelular fat (IMCF) which exists as tiny liquid droplets of fat in the cytoplasm of muscle cells (12). While IMCF is accessible for mitochondrial aerobic metabolism and plays an important part in supplying energy to our muscle cells during exercise (4,11) EMCF is relatively metabolically inert (12). Both EMCF and IMCF can lead to negative health effects when excessive fat deposits accumulate (9).

As obesity and metabolic diseases such as type 2 diabetes, cardiovascular disease, and liver disease are characterized by abnormal body fat distribution and myocellular fat deposition (10,17), the development of reliable methods of body and organ fat quantification is a continued focus as the incidence of obesity (18,19), and disease conditions involving excess fat accumulation (20-24) remain a public health and socioeconomic concern.

EMCF typically exists heterogeneously and has historically been measured in terms of a fat percentage via Magnetic Resonance Spectroscopy (MRS) while imaging sequences have been limited to the visualization of subcutaneous and visceral fat. Due to the uncertainty of spectroscopy voxel placement and the heterogeneity of EMCF and IMCF deposits in moving organs such as the heart there is great interest in the development of MR imaging methods that can provide accurate quantification of the combined EMCF and IMCF concentration.

As a research and clinical tool, quantitative MRI allows for improved pathophysiological understanding, risk assessment, diagnosis, and analysis of patient response to therapies and interventions. This work develops and validates practical MR imaging methods that focus on fat quantification, applicable in the heart and other organ systems, in combination with quantification of water relaxation parameters.

2.2 Relaxation Parameters T_1 and T_2

Hydrogen atoms have net non-zero quantum spin angular momentum, giving rise to a magnetic moment, which enables interaction with external magnetic fields, allowing energy to be absorbed and radiated at the characteristic Larmor frequency. These nuclear spins initially align parallel and anti-parallel to the main magnetic field, B_0, when in thermal equilibrium in the MRI scanner. The number of spins parallel to B_0 slightly exceeds the number of anti-parallel spins, resulting in a net magnetic moment, or magnetization, parallel to B_0. Following excitation of this magnetization from its equilibrium position towards the transverse plane the spin system will return to its equilibrium position, parallel to B_0, through a process defined as relaxation that includes both T_1 relaxation and T_2 relaxation.

Spin-lattice or T_1 relaxation occurs as an excited spin system exchanges energy with its surroundings or lattice, returning to its equilibrium position at a rate (R_1) proportional to the difference between the original equilibrium magnetization (M_0), and the current longitudinal magnetization (M_z) (Eqn. 2-1). Spin-spin relaxation or T_2 relaxation occurs as excited spins exchange energy with surrounding spins and the lattice. This spin-spin interaction causes the original spin system, which immediately following excitation had coherent phase, to lose coherence resulting in a net decrease in transverse magnetization (M_{xy}) as the spin dipoles destructively interfere. Spin-spin relaxation occurs at a rate (R_2) proportional to the M_{xy} (Eqn. 2-2).

$$\frac{dM_z(t)}{dt} = -(M_z - M_0)R_1 \qquad \text{[Equation 2-1]}$$

$$\frac{dM_{xy}(t)}{dt} = -(M_{xy})R_2 \qquad \text{[Equation 2-2]}$$

These differential rate equations can be integrated to describe the longitudinal and transverse magnetization with respect to time (t) as shown in Eqn. 2-3 and Eqn. 2-4 respectively:

$$M_z(t) = M_0 - [M_0 - M_z(0)]e^{-t/T_1} \qquad \text{[Equation 2-3]}$$

$$M_{xy}(t) = M_{xy}(0)e^{-\frac{t}{T_2}} \qquad \text{[Equation 2-4]}$$

where the T_1 relaxation, in seconds, is equal to R_1^{-1} and the T_2 relaxation is equal to R_2^{-1}.

Following a saturation pulse ($M_z = 0$) T_1 is the time required for M_z to recover to 63% of M_0. Following an excitation pulse, T_2 is the time required for M_{xy} to decay to 37% of the original $M_{xy}(0)$.

The relaxation properties of biological tissues, can be generally understood by considering how three states of water, free water, hydration water, and crystalline water experience different rates of relaxation as a consequence of differences in mobility (25). In any system molecules undergo random Brownian motion and based on the temperature of the system and its physical structure the duration that any two spins are close enough such that their local magnetic fields affect one another changes. This motion can conveniently be expressed as a frequency, $\omega_c = 1/\tau_{c,}$ where τ_c is the duration the two spins are close enough for their magnetic fields to interact. When ω_c is approximately equal to the Larmour frequency it will induce energy transitions allowing for T_1 and T_2 relaxation. Unrestricted motion, such as that observed in free water, leads to a low probability of interaction and a wide distribution of ω_c resulting in a low probability of motion at the Larmour frequency and therefore long T_1 and T_2 relaxation time constants. Conversely, crystalline water is tightly bound to macromolecules and thus has restricted motion much like a solid would. This restricted motion leads to a high probability of narrowly distributed long interactions resulting in long T_1 values and short T_2 values. Hydration water is loosely bound to macromolecules, much like a viscous fluid, and results in a moderate number of moderate duration interactions, short T_1 and T_2 values.

Differences in biological tissue T_1 and T_2 can therefore provide contrast in MRI, as each proton provides an indication of its environment. For example, an area with swelling will have a long T_2 as the amount of free water in the tissue increases.

2.3 Water-Fat Magnetic Resonance Imaging

Most clinical MRI methods detect signal from hydrogen atoms in the human body. The vast majority of this signal comes from the hydrogen atoms found in water, which comprises ~60% of our bodies. However, some signal also arises from hydrogen atoms bound to proteins, carbohydrates and fats. Because of this source of signal from fat, MRI has emerged as a direct approach to the in-vivo visualization and quantification of fat. MRI water-fat pulse sequences, as further described in the following sections, depend on either a chemical shift, or a difference in relaxometry (T_1, T_2) between water and fat. The third chapter of this thesis develops a chemical shift based method for the simultaneous quantification of fat, water T_1 and T_2, and off-resonance while the fourth chapter develops a combined relaxometry and chemical shift based approach to fat quantification. The goal of both chapters was to develop new methods for the characterization of the combined water and fat environment, with quantification of both water T_1 values and FF (for low fat fractions and in moving organs due to cardiac and respiratory motion).

2.3.1 Chemical Shift Based Fat Quantification

Hydrogen atoms in a triglyceride molecule of fat experience more electronic shielding than the hydrogen atoms in a water molecule and therefore have different resonance frequencies. Due to the complex structure of the triglyceride molecule (i.e. the different shielding effects of different hydrogen atoms) its NMR spectrum is composed of multiple resonant frequency peaks (Fig. 2-1). At body temperature the resonance frequency of the principal fat peak (peak 1), corresponding to the long CH_2 chains (26), is shifted -210Hz ($\Delta\boldsymbol{\delta}$ = 3.3ppm) from the water peak when subjected to a 1.5T magnetic field (27). The difference in resonance frequency is known as a chemical shift where the negative sign indicates that the triglyceride hydrogen atoms will precess more slowly than the water hydrogen atoms. Chemical shift, Δf_{cs}, is dependent on field strength (B_0):

$$\Delta f_{cs} = \gamma B_0 \cdot \Delta\delta[ppm] \cdot 10^{-6} \qquad \text{[Equation 2-5]}$$

where $\boldsymbol{\gamma}$ is the gyromagnetic ratio in MHz/T which is equal to 42.58MHz/T for hydrogen atoms at 1.5T. The most commonly used water-fat separation methods rely on the phase shifts ($\Delta\phi$) created by the different resonance frequencies of fat and water at a given echo time (TE) following excitation, $\Delta\phi$ = TE·off-resonance frequency, to separate the fat and water signal, which are collectively referred to as “Dixon” water-fat separation methods.

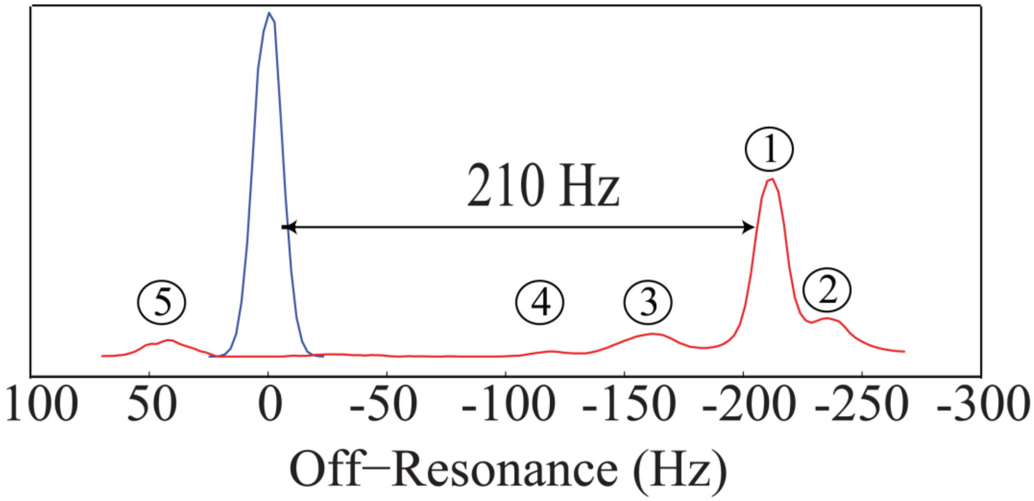

Figure 2.1 Water and Fat Spectra. Water (blue) and 5 peak fat (red) spectral line shapes, normalized to a unity area for 1.5T.

The theory behind the original “Dixon” method (28), the two point method, is easily envisioned by picturing two signal vectors for fat and water. By selectively setting the echo TE of the gradient-echo sequence, the Dixon method can produce an in-phase image and an out of phase image, referring to the complex transverse magnetization water and fat signals as adding constructively, or destructively. The resultant vector is the observed signal and by acquiring these two in phase and out of phase images the fat and water signals can be separated by adding and subtracting the two images. Specifically, Fat = $(S_{\text{in-phase}} - S_{\text{out-phase}})/2$ and Water = $(S_{\text{in-phase}}+S_{\text{out-phase}})/2$.

Over the years many adjustments and improvements have been made to this original two-point method. A three-point method (29) was developed to allow for simultaneous background field estimation and correction, and phase unwrapping (30) was proposed to deal with phase ambiguities arising from large field variation which otherwise often resulted in the erroneous assignment of water and fat pixels. More recent methods eliminate phase ambiguities by applying spatial constraints in the process of field map estimation which is more robust and has allowed for the development of cardiac water-fat imaging applications (which were previously inhibited due to the high field inhomogeneity and relatively low signal to noise ratio (SNR) of CMR) (31). One such method, which is used for validation in this work, is the VARiable PROjection water-fat estimation (VARPRO) method (32). VARPRO formulates the solution as a separable non-linear least squares problem, and finds the globally optimum maximum-likelihood solution (31). VARPRO was found to be very robust (32) in terms of correct classification of water and fat for cardiac applications with large background field variation and low SNR, and was therefore used throughout the study as a reference method for fat quantification in skeletal muscle.

2.3.2 Relaxometry Based Fat Quantification

The signal from any given hydrogen atom is a function of spin density, and longitudinal (T_1) and transverse (T_2) relaxation (among other factors such as flip angle and receiver coil efficiency). Differences in these parameters, in different tissue types and in health and disease, provide the excellent soft tissue contrast credited to MRI. For example, fat has a relatively short T_1 as compared to water and appears bright in many common clinical sequences including SSFP imaging which is of particular interest to this work (see section 2.4).

Originally, the bright signal seen from fat was often perceived as a nuisance as it could obstruct underlying pathologies and lead to artifacts. However, as the visualization of fat has become desirable as a measure of pathology a number of relaxometry-based approaches have been designed. T_1-weighted sequences have been developed to quantify abdominal subcutaneous adipose tissue (33,34), asses fat in neuromuscular disorders (21,35), and measure bone marrow in adipose tissue (36). Further, increased T_2 values in healthy muscle are indicative of the presence of fat but may be confounded by edema, which also increases T_2.

Currently relaxometry based fat quantification has focused on the visualization of gross subcutaneous and visceral adipose depots without the ability to quantify fat content, particularly in the case of low FF. No relaxometry based method, to the knowledge of the author, is currently being used for the clinical quantification of ectopic fat.

2.3.3 Spectroscopy Fat Quantification

Single voxel MRS allows one to non-invasively asses the concentration of various metabolites in tissue and has been the standard for the quantification of in-vivo ectopic fat. A triglyceride molecule is composed of a glycerol backbone and three fatty acid chains. The three fatty acid chains vary in length and structure resulting in varying degrees of electronic shielding about the hydrogen atoms resulting in multiple resonance frequencies or spectral peaks (Figure 2.1). By acquiring water suppressed and non-water suppressed spectra and comparing the relative areas under the fat and water spectra the concentration of fat can be determined.

While accurate, MRS is often not available on clinical MR scanners and is limited by spatial resolution, with large voxels and several signal averages required to produce clean spectra. Further, in organs such as the heart or liver, which are subject to motion caused by the beating of the heart and respiration, localization can be challenging and can result in spatial misalignments. In regions where ectopic fat is diffusely and heterogeneously dispersed or at fat tissue boundaries, small changes in voxel location could lead to highly variable results.

For the above stated reasons, this thesis focused on the development of rapid imaging methods that could be applied in moving organs in the clinical setting to accurately quantify low FF.

2.4 Balanced Steady State Free Precession (b-SSFP)

b-SSFP is a rapid, high SNR performance method (i.e. high signal yield with short acquisition duration) commonly used in CMR imaging. CMR is particularly challenging due to motion caused by the beating of the heart and respiration. Breath holds and gated imaging can be used to help decrease motion due to respiration, but breath holds are often difficult in sick patients and are subject to mis-registration errors while respiratory-gated methods will significantly increase scan time due to data loss during the unwanted respiratory phase. Cardiac motion is even more difficult to overcome; most commonly electrocardiogram (ECG) gated, segmented acquisitions are used which collect an image over multiple heart beats by acquiring a small piece of the image at a defined cardiac phase each heartbeat. Segmented imaging assumes no motion between segments and is degraded when respiratory motion, or poor cardiac triggering invalidates this condition. b-SSFP however has sufficient SNR to enable parallel imaging (which comes at an SNR cost) and sufficiently short repetition times (TR, Figure 2.2) such that it enables image acquisitions in a single shot during diastasis (a quiescent period during which the heart is relaxed and there is a relatively long period (~ 200 ms) with little motion). While this imaging approach does not enable the imaging of heart function (i.e. motion over a cardiac cycle), it is sufficient for freezing the motion of heart, to enable the collection of other targeted imaging information (e.g. imaging of fat).

The b-SSFP pulse sequence is composed of a train of excitation pulses separated by TR (Figure 2.2). Over the course of each TR, RF excitation pulses rotate the magnetization by the flip angle α and field inhomogeneities result in rotation, ϕ, about the B_0 axis. In addition to these rotations T_1 and T_2 relaxation results in in an increase in longitudinal and decrease in transverse magnetization, respectively. For the balanced b-SSFP sequence the net gradient induced dephasing within every TR is zero, due to matching gradient pulses of opposite polarity, such that the gradients have no net effect on the magnetization (Figure 2.2). These balanced gradients preserve much of the transverse magnetization, which is rotated by the subsequent RF pulse, resulting in high signal intensity. By starting with an α/2 RF preparation pulse followed by an alternating train of ±α pulses (i.e. 180 phase shift between each sequential pulses) the magnetization will form an "α/2 cone" as the transverse magnetization slowly and smoothly converges to steady state (Figure 2.3).

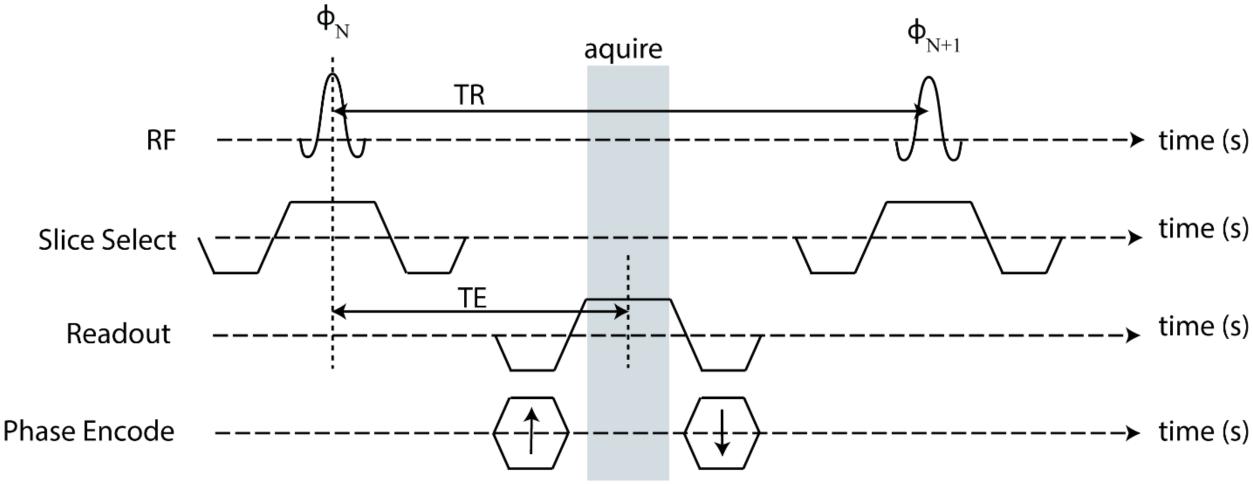

Figure 2.2 Balanced Steady State Free Precession Pulse Sequence.

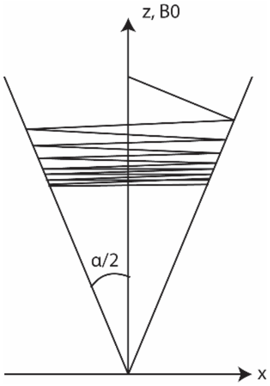

Figure 2.3 b-SSFP magnetization visualization. Oscillation about the z-axis by means of an initial α/2 preparation pulse and a train of alternating ±α excitations.

When the magnetization reaches steady state, the b-SSFP signal contrast depends on the ratio T_2/T_1 and has therefore received considerable attention as a method for cardiac fat visualization (37) as the relatively long T_2 and short T_1 of fat results in high b-SSFP image intensity. As discussed further in Chapter 3, b-SSFP signal has a characteristic and repeating "pass-band" behavior with periodic (every 1/TR) magnitude and phase behavior (Figure 2.4). In a typical b-SSFP pulse sequence, as shown in Figure 2.2, signal is acquired with on resonance excitation whenever possible (with RF phase increment ($\Delta\phi$) of 180^o such that $\phi_{N+1} = \phi_N + \Delta\phi$) to avoid the unwanted signal minima (Figure 2.4). For a TE = TR/2, the most commonly used b-SSFP TE, the phase in adjacent bands will differ by 180^o such that if water and fat resonances fall within adjacent bands (dependent on TR and off-resonance frequency), their opposing phase will result in the "India ink" artifact commonly seen at water-fat interfaces (38,39).

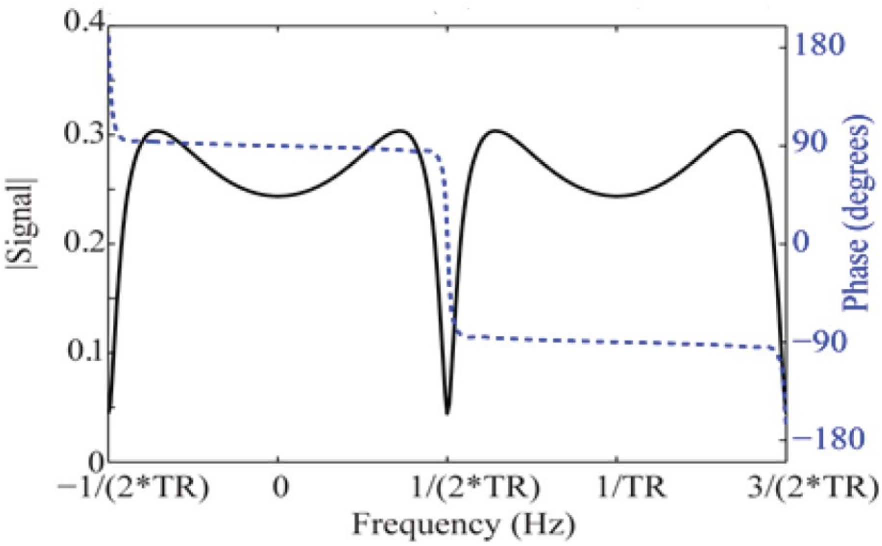

Figure 2.4 b-SSFP magnitude and phase signal profile.

In this work we aim to take advantage of the frequency response of the b-SSFP signal to develop two fat quantification methods.

2.5 T_1 Mapping

The longitudinal relaxation (T_1) of the myocardium is a time constant that reflects the water environment in tissues, with longer values typically reflecting a less restricted motion environment (see section 2.2). In numerous myocardial disease states either swelling (inflammation) (1) or changes in extracellular volume fraction (ECV) (e.g. with myocardial fibrosis(2)) can increase the T_1 of the myocardium from its typical value of ~1175 ms (at 1.5T) (40). Further, reduced T_1 values have been measured in diseases such as Anderson-Fabry disease (23,24) and iron overload (41). As a result, quantitative myocardial T_1 mapping sequences are gaining recognition in the non-invasive assessment of tissue characteristics. The use of contrast agents to further probe the ECV using pre-contrast and post-contrast T_1 values is also now widely used in clinical research (42-44). However, this work focuses on native (non-contrast) T_1 mapping.

The following discussion on T_1 quantification will focus on two pixel-wise mapping methods; MOdified Look-Locker Inversion (MOLLI) (45) and SAturation recovery single-SHot Acquisition (SASHA) (46). This discussion is intended to relay the fundamentals of these two methods, while a more comprehensive review detailing the accuracy and precision of each method has been recently published by Kellman and Hansen (42). The SASHA method, in particular, forms the foundation of the proposed combined fat and T_1 imaging methods detailed in Chapters 3 and 4. Both MOLLI and SASHA methods are based on the b-SSFP acquisition with three key steps: 1) preparation of the longitudinal magnetization through inversion (MOLLI) or saturation (SASHA), 2) a sampling of the recovery of the longitudinal magnetization, and 3) fitting of the recovery data with a mono-exponential curve to estimate T_1. Simplified schematics comparing the SASHA and MOLLI pulse sequences are shown in Figure 2.5.

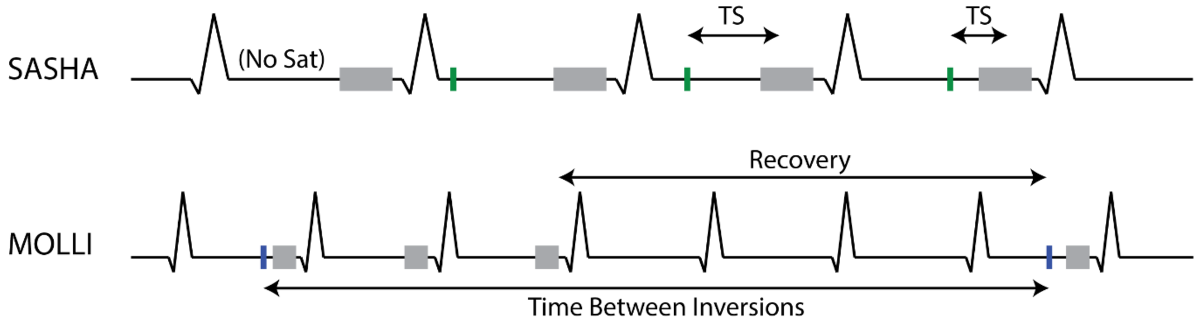

Figure 2.5 SASHA and MOLLI schematic diagrams. The SASHA pulse sequence shows the collection of an initial non-sat image followed by variable saturation recovery times (TS) between the saturation pulse (green) and the imaging readout (grey). The MOLLI pulse sequence shows an inversion pulse (blue) followed by three imaging readouts (grey) before allowing the magnetization to recover before the second inversion pulse.

2.5.1 MOLLI

The MOdified Look-Locker Inversion (MOLLI) recovery sequence consists of an initial inversion recovery pulse followed by several ECG-triggered single-shot images acquired at the same cardiac phase in sequential heartbeats (45). Additional MOLLI "Look-Locker sets", with different trigger times, can be combined to more effectively sample the initial steep region of the recovery curve. With every sequential image acquisition the magnetization is perturbed causing images acquired more than one heartbeat after the inversion pulse to have a magnetization history. This magnetization history leads to errors causing the MOLLI sequence to significantly underestimate T_1 values, specifically in tissues with short T_2 relaxation times (46). The result of this perturbation is the measurement of an apparent recovery time denoted as T_1^* which is shorter than the true T_1. The recovery data is fit with a three-parameter exponential model,

$$S(t) = A - B\exp(-TI/T_1^*), \qquad \text{[Equation 2-6]}$$

from which the true T_1 is then approximated as

$$T_1 \approx T_1^*\,(B/A-1), \qquad \text{[Equation 2-7]}$$

where (B/A-1) is known as the "Look-Locker correction factor". This correction factor is only effective at very low flip angles (MOLLI is typically performed with a 35 degree flip angle), but still results in significant underestimation of T_1 (42). Numerous alterations of the MOLLI method have been published to reduce scan time (47), or improve precision (48). A discussion of these methods, and several other variants is beyond the scope of this work.

2.5.2 SASHA

In an effort to avoid errors associated with MOLLI, Chow et al. proposed the SAturation recovery single-SHot Acquisition (SASHA) sequence in 2014 (46). This method largely overcomes T_2 dependencies, as well as heart rate, off-resonance, blood flow and magnetization transfer dependencies associated with MOLLI T_1 calculations (42).

The SASHA pulse sequence consists of an initial non-sat image followed by 10 saturation recovery ECG-triggered single-shot images acquired at the same cardiac phase in sequential heartbeats with incremented saturation recovery (TS) times. By applying a saturation pulse before every image acquisition, the magnetization history is eliminated and it was shown that the resulting saturation-recovery curve is not effected by the readout and therefore gives a true T_1 value not a shortened apparent value (46). The result is a 3-parameter model:

$$S(t) = A - B \exp(-TS/T_1). \qquad \text{[Equation 2-8]}$$

Subsequently it was shown that 2-parameter fitting (assuming ideal saturation, Eqn. 2-9) significantly reduced variability in the best fit T_1 values for a given SNR (42).

$$S(t) = A(1 - \exp(-TS/T_1)) \qquad \text{[Equation 2-9]}$$

The optimized SASHA experiment, using a variable flip angle approach (49) with a 2-parameter fitting model (42) results in similar variability as MOLLI (49) but with much better accuracy.

2.6 Multi-Parameter Quantification

Quantitative MRI provides absolute measures of tissue properties, overcoming inter-site and inter-observer biases while multi-parameter fitting offers more comprehensive tissue characterization and can expose confounders of each parameter. By simultaneously measuring multiple parameters, chapter four evaluates the dependence of inversion and saturation recovery T_1 measurements on off-resonance and FF. In this case, if T_1 was quantified without the simultaneous quantification of fat and off-resonance one would be unsure if/how their results were affected by these confounding variables. Both methods proposed in this work, while focusing of the quantification of fat, provide multi-parameter quantification.

2.7 Chapter 2 References

1. Ferreira VM, Piechnik SK, Dall'Armellina E, Karamitsos TD, Francis JM, Choudhury RP, Friedrich MG, Robson MD, Neubauer S. Non-contrast T1-mapping detects acute myocardial edema with high diagnostic accuracy: a comparison to T2-weighted cardiovascular magnetic resonance. Journal of Cardiovascular Magnetic Resonance 2012;14(1):42-42.

2. Bull S, White SK, Piechnik SK, Flett AS, Ferreira VM, Loudon M, Francis JM, Karamitsos TD, Prendergast BD, Robson MD, Neubauer S, Moon JC, Myerson SG. Human non-contrast T1 values and correlation with histology in diffuse fibrosis. Heart 2013;99(13):932-937.

4. Goodpaster BH, Wolf D. Skeletal muscle lipid accumulation in obesity, insulin resistance, and type 2 diabetes. Pediatric Diabetes 2004;5(4):219-226.

9. Bray GA. Handbook of Obesity --: Epidemiology, Etiology, and Physiopathology, Third Edition: Taylor & Francis; 2014.

10. Hu HH, Kan HE. Quantitative proton MR techniques for measuring fat. NMR in biomedicine 2013;26(12):1609-1629.

11. Gillies AR, Lieber RL. Structure and function of the skeletal muscle extracellular matrix. Muscle & nerve 2011;44(3):318-331.

12. Boesch C, Slotboom J, Hoppeler H, Kreis R. In vivo determination of intra-myocellular lipids in human muscle by means of localized 1H-MR-spectroscopy. Magnetic Resonance in Medicine 1997;37(4):484-493.

13. Leroy-Willig A, Willig TN, Henry-Feugeas MC, Frouin V, Marinier E, Boulier A, Barzic F, Schouman-Claeys E, Syrota A. Body composition determined with MR in patients with Duchenne muscular dystrophy, spinal muscular atrophy, and normal subjects. Magnetic resonance imaging 1997;15(7):737-744.

14. Visser M, Goodpaster BH, Kritchevsky SB, Newman AB, Nevitt M, Rubin SM, Simonsick EM, Harris TB, Study ftHA. Muscle Mass, Muscle Strength, and Muscle Fat Infiltration as Predictors of Incident Mobility Limitations in Well-Functioning Older Persons. The Journals of Gerontology Series A: Biological Sciences and Medical Sciences 2005;60(3):324-333.

15. Goutallier D, Postel JM, Bernageau J, Lavau L, Voisin MC. Fatty muscle degeneration in cuff ruptures. Pre- and postoperative evaluation by CT scan. Clinical orthopaedics and related research 1994(304):78-83.

16. Nakagaki K, Ozaki J, Tomita Y, Tamai S. Fatty degeneration in the supraspinatus muscle after rotator cuff tear. Journal of shoulder and elbow surgery / American Shoulder and Elbow Surgeons [et al] 1996;5(3):194-200.

17. Samara A, Ventura EE, Alfadda AA, Goran MI. Use of MRI and CT for fat imaging in children and youth: what have we learned about obesity, fat distribution and metabolic disease risk? Obesity reviews : an official journal of the International Association for the Study of Obesity 2012;13(8):723-732.

18. Katherine M Flegal MDC, Cynthia L. Ogden, Lester R. Curtin. Prevalence and Trends in Obesity Among US Adults, 1999-2008. Journal of American Medical Association (JAMA) 2010;303(3):235-241.

19. Ogden CL, Carroll MD, Kit BK, Flegal KM. Prevalence of obesity and trends in body mass index among US children and adolescents, 1999-2010. Jama 2012;307(5):483-490.

20. Rutger W. van der Meer HJL, Johannes W.A. Simit, Albert de Roos. MR Imaging Evaluation of Cadiovascular Risk in Metabolic Syndrome. Radiology 2012;264(1).

21. Wattjes MP, Kley RA, Fischer D. Neuromuscular imaging in inherited muscle diseases. European radiology 2010;20(10):2447-2460.

22. Reeder SB, Cruite I, Hamilton G, Sirlin CB. Quantitative assessment of liver fat with magnetic resonance imaging and spectroscopy. Journal of magnetic resonance imaging : JMRI 2011;34(4):729-749.

23. Sado DM, White SK, Piechnik SK, Banypersad SM, Treibel T, Captur G, Fontana M, Maestrini V, Flett AS, Robson MD, Lachmann RH, Murphy E, Mehta A, Hughes D, Neubauer S, Elliott PM, Moon JC. Identification and assessment of Anderson-Fabry disease by cardiovascular magnetic resonance noncontrast myocardial T1 mapping. Circulation Cardiovascular imaging 2013;6(3):392-398.

24. Thompson RB, Chow K, Khan A, Chan A, Shanks M, Paterson I, Oudit GY. T(1) mapping with cardiovascular MRI is highly sensitive for Fabry disease independent of hypertrophy and sex. Circulation Cardiovascular imaging 2013;6(5):637-645.

25. Bloembergen N, Purcell EM, Pound RV. Relaxation Effects in Nuclear Magnetic Resonance Absorption. Physical Review 1948;73(7):679-712.

26. Hamilton G, Yokoo T, Bydder M, Cruite I, Schroeder ME, Sirlin CB, Middleton MS. In vivo characterization of the liver fat 1H MR spectrum. NMR in biomedicine 2011;24(7):784-790.

27. Bley TA, Wieben O, Francois CJ, Brittain JH, Reeder SB. Fat and water magnetic resonance imaging. Journal of magnetic resonance imaging : JMRI 2010;31(1):4-18.

28. Dixon WT. Simple proton spectroscopic imaging. Radiology 1984;153(1):189-194.

29. Glover GH, Schneider E. Three-point dixon technique for true water/fat decomposition with B0 inhomogeneity correction. Magnetic Resonance in Medicine 1991;18(2):371-383.

30. Szumowski J, Coshow WR, Li F, Quinn SF. Phase unwrapping in the three-point Dixon method for fat suppression MR imaging. Radiology 1994;192(2):555-561.

31. Kellman P, Hernando D, Shah S, Zuehlsdorff S, Jerecic R, Mancini C, Liang Z-P, Arai AE. Multi-echo Dixon Fat and Water Separation Method for Detecting Fibro-fatty Infiltration in the Myocardium. Magnetic Resonance in Medicine 2009;61(1):215-221.

32. Hernando D, Haldar JP, Sutton BP, Ma J, Kellman P, Liang ZP. Joint estimation of water/fat images and field inhomogeneity map. Magnetic Resonance in Medicine 2008;59(3):571-580.

33. JC Seidell CB, K van der Kooy. Imaging techniques for measuring adipose-tissue distribution-a comparison between computed tomography and 1.5-T magnetic resonance. . Am J Clin Nutr 1990;51:953-957.

34. Machann J, Thamer C, Schnoedt B, Haap M, Haring HU, Claussen CD, Stumvoll M, Fritsche A, Schick F. Standardized assessment of whole body adipose tissue topography by MRI. Journal of magnetic resonance imaging : JMRI 2005;21(4):455-462.

35. Mercuri E, Pichiecchio A, Allsop J, Messina S, Pane M, Muntoni F. Muscle MRI in inherited neuromuscular disorders: past, present, and future. Journal of magnetic resonance imaging : JMRI 2007;25(2):433-440.

36. Shen W, Chen J, Gantz M, Punyanitya M, Heymsfield SB, Gallagher D, Albu J, Engelson E, Kotler D, Pi-Sunyer X, Gilsanz V. MRI-measured pelvic bone marrow adipose tissue is inversely related to DXA-measured bone mineral in younger and older adults. European journal of clinical nutrition 2012;66(9):983-988.

37. Goldfarb JW, Arnold-Anteraper S. Water-fat separation imaging of the heart with standard magnetic resonance bSSFP CINE imaging. Magnetic Resonance in Medicine 2014;71(6):2096-2104.

38. Aquaro GD, Todiere G, Strata E, Barison A, Di Bella G, Lombardi M. Usefulness of India ink artifact in steady-state free precession pulse sequences for detection and quantification of intramyocardial fat. Journal of magnetic resonance imaging : JMRI 2014;40(1):126-132.

39. Hargreaves BA, Vasanawala SS, Nayak KS, Hu BS, Nishimura DG. Fat-suppressed steady-state free precession imaging using phase detection. Magnetic Resonance in Medicine 2003;50(1):210-213.

40. Kellman P, Bandettini WP, Mancini C, Hammer-Hansen S, Hansen MS, Arai AE. Characterization of myocardial T1-mapping bias caused by intramyocardial fat in inversion recovery and saturation recovery techniques. Journal of Cardiovascular Magnetic Resonance 2015;17(1):33.

41. Wood JC, Otto-Duessel M, Aguilar M, Nick H, Nelson MD, Coates TD, Pollack H, Moats R. Cardiac Iron Determines Cardiac T2*, T2, and T1 in the Gerbil Model of Iron Cardiomyopathy. Circulation 2005;112(4):535-543.

42. Kellman P, Hansen MS. T1-mapping in the heart: accuracy and precision. Journal of Cardiovascular Magnetic Resonance 2014;16(1):2-22.

43. Pennell DJ, Sechtem UP, Higgins CB, Manning WJ, Pohost GM, Rademakers FE, van Rossum AC, Shaw LJ, Yucel EK. Clinical indications for cardiovascular magnetic resonance (CMR): Consensus Panel report. European heart journal 2004;25(21):1940-1965.

44. Hunold P, Schlosser T, Vogt FM, Eggebrecht H, Schmermund A, Bruder O, Schuler WO, Barkhausen J. Myocardial late enhancement in contrast-enhanced cardiac MRI: distinction between infarction scar and non-infarction-related disease. AJR American journal of roentgenology 2005;184(5):1420-1426.

45. Messroghli DR, Radjenovic A, Kozerke S, Higgins DM, Sivananthan MU, Ridgway JP. Modified Look-Locker inversion recovery (MOLLI) for high-resolution T1 mapping of the heart. Magnetic Resonance in Medicine 2004;52(1):141-146.

46. Chow K, Flewitt JA, Green JD, Pagano JJ, Friedrich MG, Thompson RB. Saturation recovery single-shot acquisition (SASHA) for myocardial T1 mapping. Magnetic Resonance in Medicine 2014;71(6):2082-2095.

47. Piechnik SK, Ferreira VM, Dall'Armellina E, Cochlin LE, Greiser A, Neubauer S, Robson MD. Shortened Modified Look-Locker Inversion recovery (ShMOLLI) for clinical myocardial T1-mapping at 1.5 and 3 T within a 9 heartbeat breathhold. Journal of cardiovascular magnetic resonance : official journal of the Society for Cardiovascular Magnetic Resonance 2010;12:69.

48. Schelbert EB, Testa SM, Meier CG, Ceyrolles WJ, Levenson JE, Blair AJ, Kellman P, Jones BL, Ludwig DR, Schwartzman D, Shroff SG, Wong TC. Myocardial extravascular extracellular volume fraction measurement by gadolinium cardiovascular magnetic resonance in humans: slow infusion versus bolus. Journal of cardiovascular magnetic resonance : official journal of the Society for Cardiovascular Magnetic Resonance 2011;13:16.

49. Chow K, Spottiswoode BS, Pagano JJ, Thompson RB. Improved precision in SASHA T1 mapping with a variable flip angle readout. Journal of Cardiovascular Magnetic Resonance 2014;16(Suppl 1):M9.

Chapter 3. Simultaneous Quantification of Fat Fraction, Water T_1 and T_2, and Off-Resonance Frequency Using Phase Sweep b-SSFP

3.1 Abstract

Purpose: The goals of this study were to describe and validate a new method called Phase Sweep b-SSFP for the simultaneous quantification of FF, water T_1 and T_2, and off-resonance frequency for low FF (0-10%).

Methods: Bloch equation and Monte Carlo simulations, as well as phantom and in-vivo (skeletal muscle) experiments were used to characterize the response of the b-SSFP phase sweep profile, to mixed water-fat systems at 1.5T. The phase sweep profile is obtained by acquiring multiple b-SSFP images with incremented RF pulse phase. By fitting this profile with a predefined dictionary of water and fat profiles, the aforementioned parameters can be quantified. Fat fractions were compared with single voxel spectroscopy and a Dixon imaging method that also provided a measure of off-resonance, while water T_1 and T_2 were compared with spin echo and single voxel spectroscopy experiments.

Results: Variability in the quantification of the above mentioned parameters is largely independent with no bias observed a function of SNR in Monte Carlo simulations. Phantom and in-vivo results are in strong agreement with their respective FF, T_1, T_2, and off-resonance validation methods.

Conclusions: The proposed Phase Sweep b-SSFP imaging method allows for rapid multi-parameter quantification of FF, water T_1 and T_2, and off-resonance.

Keywords: Fat, b-SSFP, quantification, T_1, T_2

3.2 Introduction

Many diseases do not result in visually apparent abnormalities in function or morphology until the later stages of disease progression. MRI offers potential early detection of pathology based on its sensitivity to changes in the microscopic tissue environment by being sensitive to the longitudinal and transverse relaxation time constants (T_1, and T_2) and FF. Quantitative imaging of myocardial T_1 is increasingly used to evaluate pathology related to edema (1) and fibrosis (2), while quantitative imaging of T_2 is being used to identify edema and hemorrhage (3). Further, the excess accumulation of fat in tissues is a common feature related to multiple diseases such as obesity (4), type 2 diabetes (4) and fatty liver disease (8), among many other, and has motivated the development of new methods to quantify fat content in the clinical setting.

The goals of the current study were to develop a quantitative multi-parameter MRI method to provide simultaneous quantification of FF, water T_1 and T_2, and off-resonance frequency, with applicability to challenging moving organs systems (e.g. heart and liver). There are currently no existing methods that are applicable for simultaneous quantification of these parameters, particularly for the case of lower FF and the limitations imposed by cardiac and respiratory motion. The proposed method, termed Phase Sweep b-SSFP, is based on the acquisition of multiple single-shot b-SSFP images acquired with different off-resonance frequencies, or equivalently, different phase-increments between sequential radio frequency (RF) pulses.

3.3 Theory

The b-SSFP pulse sequence is composed of a train of excitation pulses separated by a time interval TR within which the net gradient-induced is zero, and with a 180 degree phase increment between sequential RF pulses. The evolution of the magnetization within a single TR period can therefore be fully described by simple RF pulse rotations and T_1 and T_2 relaxation (neglecting the effects of off-resonance caused by magnetic field in-homogeneities) which will oscillate about the B_0 vector forming an α/2 cone as the transverse magnetization slowly decays towards a steady state value, as was shown in Figure 2.3 in the previous chapter (50).

The phase of the transverse magnetization that is accumulated over a single TR is given by

$$\emptyset = 2\pi f TR \qquad \text{[Equation 3-1]}$$

where *f* is the off-resonance frequency. For $\emptyset = 2n\pi$, where n is any integer, the refocusing mechanism of the b-SSFP method breaks down resulting in a steep drop in signal and the characteristic shape of the signal profile shown in Figure 3.1a. Since a phase accrual of $\emptyset$ is indistinguishable from a phase accrual of $\emptyset + n360°$, where n is any integer, the b-SSFP signal is periodic with increasing off-resonance frequency. From equation 3-1 the period of the signal profile is TR^{-1} Hz. When TE=TR/2 a phase inversion of the b-SSFP signal from 90^o to -90^o will occur in sequential bands of the periodic signal profile causing the sign of the transverse magnetization to alternate between positive and negative (dashed blue line in below Figure 3.1a) (27).

Critically, the use of single shot b-SSFP for the proposed methods enable the acquisition of images with short acquisition times (~200-300 ms) which are compatible with cardiac imaging. Images acquired with this method are routinely used in T_1-mapping applications (45,46) to freeze the negative effects of cardiac and respiratory motion

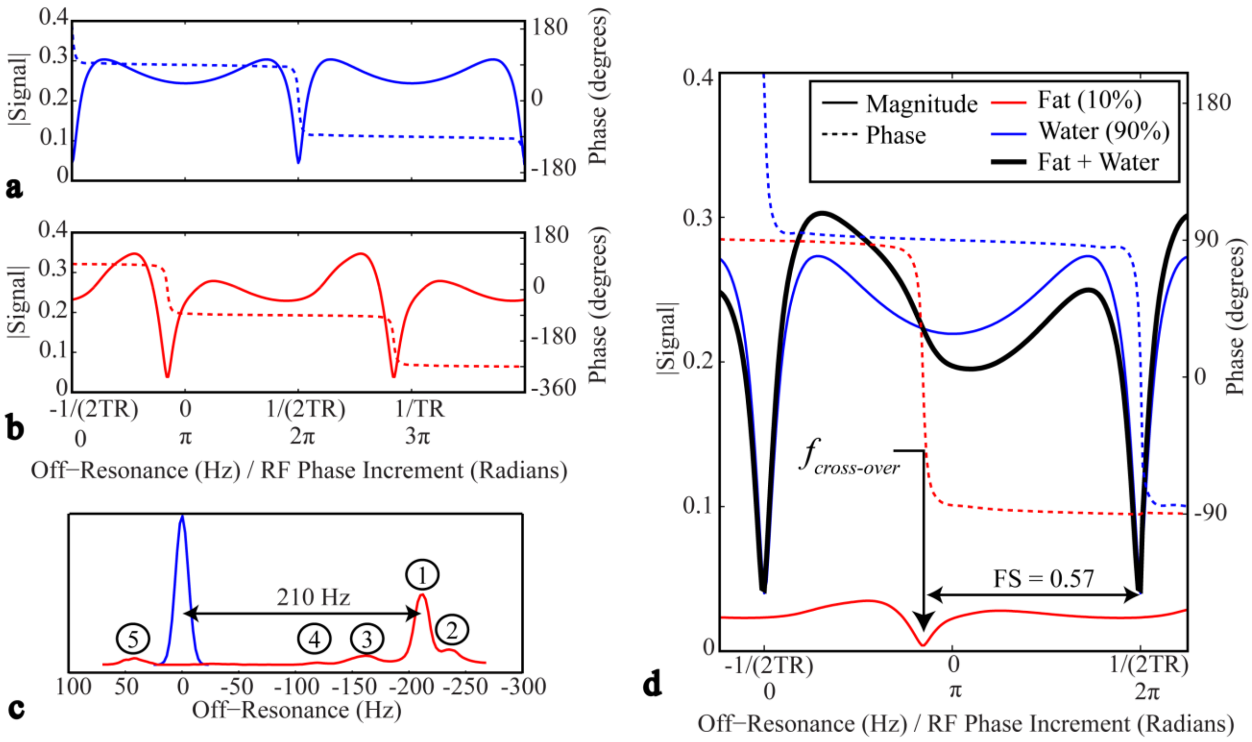

Figure 3.1 Phase sweep profile interference. Sample b-SSFP phase sweep profiles (solid = magnitude, dashed=phase) for water **(a)** and fat **(b)**. **c:** Water (blue) and fat (red) spectral line shapes, normalized to a unity area. 5 fat peaks were considered. **d:** Sample b-SSFP phase sweep profile for water (blue), fat (red), and their sum (black), showing bands of constructive and destructive interference in the combined profile (10% fat fraction). The fractional shift (FS) between the water and fat profiles is 0.57, where FS = 1 is the distance between black bands. All plots are for 1.5T and a TR of 2.7 ms.

3.3.1 Dependence of the Phase Sweep Profile on Flip Angle, T_2 and T_1

In a typical b-SSFP experiment a single image would be acquired as close to on-resonance (0 Hz) as possible and with a phase-increment of 180 degrees between each sequential RF pulse. However, the shape and magnitude of the entire signal profile as a function of off-resonance frequency contains valuable information. As shown in Figure 3.2a and b the shape of the profile is dependent on flip angle and T_2, where the stated flip angle refers to the target flip but includes a distribution of flip angles over the slice profile. Figure 3.2c also shows that the magnitude of the profile is dependent on T_1.

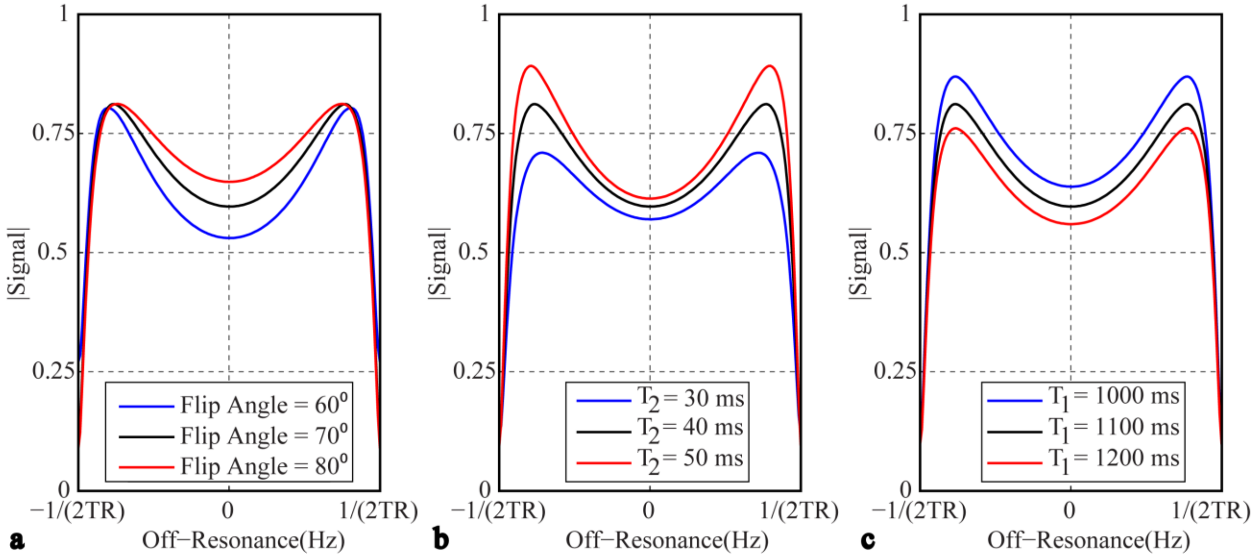

Figure 3.2 Phase sweep profile dependence on flip angle, T_2 and T_1. All plots are for a water phase sweep profile where the default flip angle, T_2 and T_1 values are 70°, 40 ms and 1100 ms respectively.

It is hypothesized that because the shape of the profile contains information regarding T_1 and T_2, it is possible to determine these values by collecting data spanning the entire frequency range of the profile. While the profile can be sampled by acquiring images with different off-resonance frequencies, the same data can be acquired by changing the phase-increment between the sequential RF pulses (Figure 3.1). This phase increment interpretation of the signal profile has been previously published by Karla L Millar (51). In this interpretation, off-resonance is described as the phase offset between the defined carrier frequency and the RF pulse; which can be changed by incrementing the phase of the RF pulse and effectively changing how far off-resonance the carrier frequency appears. By collecting multiple images in which the phase of the RF pulse is incremented from 0 to 2π rad one can systematically generate the characteristic signal profile shown in Figure 3.1a. The systematic acquisition of this profile will be referred to as Phase Sweep b-SSFP. To aid in describing the b-SSFP profile we have adopted terminology proposed by Karla L. Millar where signal which varies sharply with frequency (near multiples of 2π) is referred to as the "transition band" and signal which is relatively insensitive to frequency (near odd multiples of π) is referred to as the "pass band" (51).

3.3.2 Chemical Shift and Frequency Distribution Effects on the b-SSFP Profile

The primary effect of the different magnetic susceptibilities of our heterogeneous tissues is a distribution of static magnetic fields, even within a uniform B_0 field, and a resulting distribution of resonant frequencies. The effects of asymmetric frequency distributions on the phase sweep profile have been previously described (51), however, the effects of the complex frequency distribution of fat spectra on the phase sweep profile have not previously been considered.

While a symmetric Gaussian shape can be used to simulate a water spectrum, the fat spectrum contains multiple resonant frequency peaks (Figure 3.1c) due to complex electronic shielding of the triglyceride hydrogen atoms and was modeled based on an empirically measured peanut oil spectrum, where peanut oil has been shown to be a good model for in-vivo fat (52). In this study five main spectral peaks of fat were accounted for, with the principal peak (peak 1) shifted 3.3ppm (-210Hz) from the water peak when subjected to a 1.5T magnetic field at body temperature. Due to this asymmetric frequency distribution the resulting fat phase sweep signal profile becomes asymmetric about the resonant frequency (Figure 3.1b).

With a TR of 2.7 ms, which is common for applications in cardiac imaging, the period of the b-SSFP profile becomes 370 Hz and the fat and water b-SSFP signal profiles are shifted by $FS = 42.576\ MHz\, T^{-1} * 3.3\ ppm * B_0 * TR = 140.5\ Hz\, T^{-1}\ * 1.5\ T * 0.0027\, \mathrm{sec} = 0.57$, where FS stands for fractional shift (FS = 1 is the distance between transition bands). As a result of the phase inversion in sequential b-SSFP bands this FS leads to the constructive and destructive interference between fat and water signals observed in the black asymmetric profile shown in Figure 3.1d. The location of the phase cross-over, where the fat signal profile has a phase inversion, can be defined as $f_{\text{cross-over}} = (0.5 \cdot \text{TR}^{-1} - 42.576\ \text{MHz}\ \text{T}^{-1} \cdot 3.3\ \text{ppm} \cdot \text{B}_0)$ where the term $0.5 \cdot \text{TR}^{-1}$ corresponds to the frequency shift from the center of a b-SSFP band to the closest transition or black band.

At 1.5T a TR of 7.1ms results in a FS = 1.5 which would again result in the constructive and destructing interference seen in Figure 3.1d. However, at this TR the smaller bandwidth resulted in the fat being shifted by more than a pixel. At our shorter TR of 2.7ms the bandwidth is high enough that fat-water shift artifact is negligible.

The characteristic response of such composite water-fat systems (with variable relaxation constants, FF and off-resonance) to the phase sweep b-SSFP pulse sequence is considered below.

3.4 Methods

3.4.1 Method Development

3.4.1.1 Quantification of Tissue Characteristics from the Phase Sweep b-SSFP Profile

The b-SSFP signal in a mixed water-fat system, S_{w+F}, can be defined as a sum of the weighted signals of water, S_w, and fat, S_F, (Figure 3.1d):

$$S_{w+F} = (1 - FF) \cdot S_w(f) + FF \cdot S_F(f), \qquad \text{[Equation 3-2]}$$

where FF is the fat fraction and f is the off-resonance frequency. From this equation it was hypothesized that by using simulated phase sweep profiles for water and fat the FF could be determined. However, in order to account for all of the parameters that effect the shape of the phase sweep profile, tissue parameters T_1 and T_2 had to be considered (Figure 3.2):

$$S_{w+F} = (1 - FF) \cdot S_w\left(T_{1,w}, T_{2,w}, f\right) + \; FF \cdot S_F\left(T_{1,F}, T_{,2F}, f\right). \qquad \text{[Equation 3-3]}$$

Further, in order to achieve highly independent quantification of water T_1 it was found that two data acquisitions (one with and one without saturation recovery weighting) were required such that the T_1 of water would be determined largely by the difference in signal magnitude between the saturation recovery and non-saturation images. Sufficiently long TS times ensure identical fat signals in both acquisitions. In this way, the variability in each parameter becomes largely independent; FF is determined by profile asymmetry, $T_{2,w}$ by the depth of the profile dip in the pass band, $T_{1,w}$ by saturation recovery weighting, and off-resonance frequency by a global profile shift. Hence by solving the Eqn. 3-4:

$$rss(S_{w+F}|_{TS=700ms} - P_{w+F}|_{TS=700\,ms}) + \; rss(S_{w+F}|_{TS=\infty} - P_{w+F}|_{TS=\infty}) \;\approx 0.$$

[Equation 3-4]

where P_{w+F} is an asymmetric simulated profile with weighted water and fat signal profiles from predefined dictionaries, the T_1, T_2, and f each acquired profile (S_{w+F}) and their relative weightings (FF) can be determined offline by using the Nelder Mead search algorithm *fminsearch* in MATLAB R2013a (The MathWorks; Natick, MA).

3.4.1.2 Dictionary Design

A dictionary of simulated basis signal profiles for fat and water were created using the Bloch equation Matlab MEX function created by Brian Hargreaves and shared at http://mrsrl.stanford.edu/~brian/blochsim/. The basis sets span a large range of $T_{1,w}$ (250:5:1505) ms, $T_{2,w}$ (20:1:60, 62:4:82, 92:10:212) ms, $T_{1,f}$ (210:5:220, 240:10:260) ms and $T_{2,f}$ (40:10:90) ms values, and incorporate the exact pulse sequence parameters.

A variable flip angle (VFA) readout was used to minimize signal oscillations in the approach to steady-state and associated artifacts (49). For the VFA readout the flip angle, α, of the first 29 RF pulses were scaled by sin(x) where $\pi/90 < x < \pi/2$. Data was not acquired for the first 5 pulses and an $\alpha/2$ closer pulse was used at the end of the image readout.

Flip angle distribution observed across the slice was accounted for by generating a single signal profile from a weighted histogram of flip angles (27). The signal intensity weighting of each flip angle is determined by the excited transverse magnetization. A saturation recovery and a non-saturation basis profile were generated for every combination of the above stated $T_{1,w}$, $T_{2,w}$, $T_{1,f}$, and $T_{2,f}$ parameters. A single TS time of 700 ms was used as it ensures near full recovery of the fat signal and is compatible with cardiac imaging in most subjects.

3.4.1.3 Fitting

Fitting of the acquired saturation recovery and non-saturation asymmetric profiles (50 phase sweep RF frequency offsets spanning 463Hz) with the weighted sum of fat and water basis profiles from the bank is performed offline using the Nelder Mead direct search algorithm *fminsearch* in MATLAB R2013a. Off resonance is accounted for by allowing a simple shift in the frequency dimension for both fat and water basis profiles in the fitting process (same shift in both), and the T_1 and T_2 of the fat basis profile are specified to increase processing efficiency ($T_{1,F}$ = 250ms, $T_{2,F}$ = 80ms), and because these values are not expected to vary person to person or with pathology. Thus, the unknown parameters of the fitting algorithm are reduced to FF, water T_1 and T_2, water and fat spectral linewidth, and off-resonance. $T_{1,F}$ and $T_{2,F}$ can be modified as needed but are not currently optimized by the minimization function.

The error in the fit is calculated as the root sum square of the difference between the acquired and simulated saturation and non-saturation curves. Based on the best saturation and non-saturation water basis profiles the T_1 and T_2 of water can be determined. The relative weighting of the fat and water profiles defines the FF and the common shift of the fat and water profiles defines off-resonance. Fitting can be performed on prescribed regions of interest (ROIs) or pixel by pixel to generate a map.

A generalized schematic of the fitting process described above is shown in Figure 3.3. To increase efficiency of the fitting algorithm the initial off-resonance guess is defined by determining the maximum correlation coefficient between a simulated profile and the acquired profile. Off-resonance could also be estimated using an acquired off resonance map.

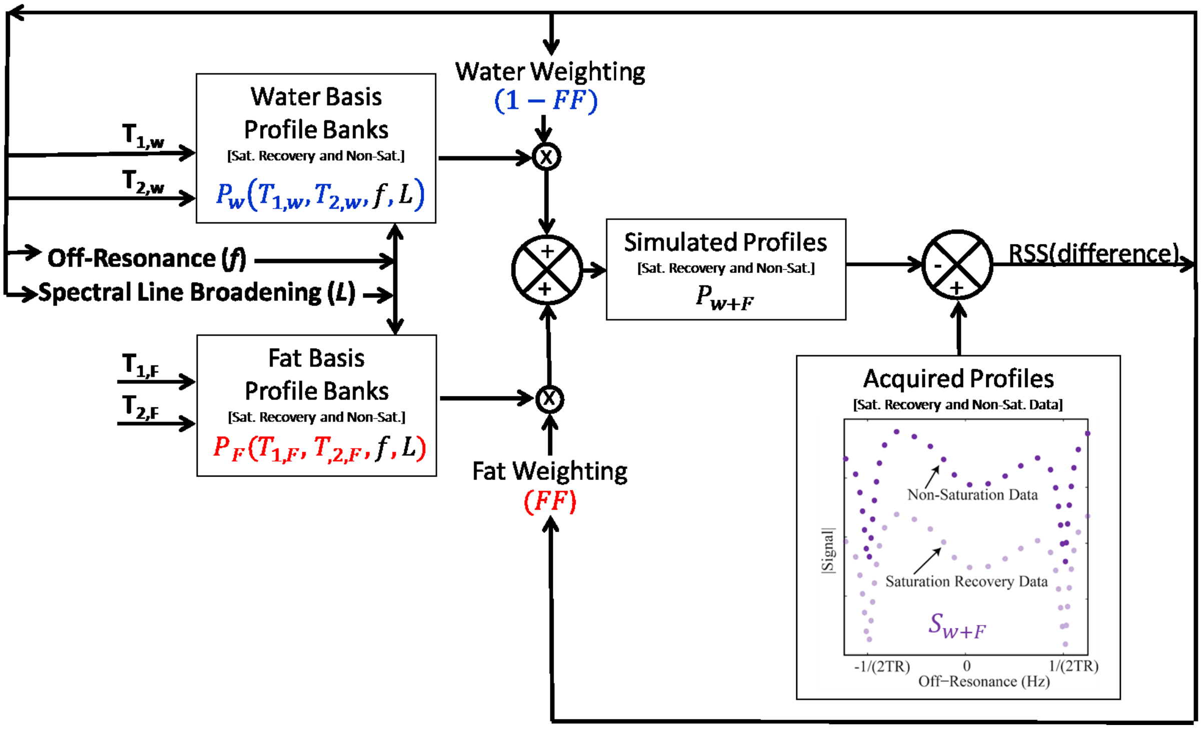

Figure 3.3 Simplified Flow Diagram of the Phase Sweep b-SSFP Fitting Algorithm.

The fitting process outlined in Figure 3.3 is performed in two steps. In the first step all data points (50 phase sweep RF frequency offsets spanning 463Hz) across the saturation recovery phase sweep profile period are used to achieve initial off-resonance, T_1,w T_2,w and FF values. In step two, points in the transition regions of the saturation recovery phase sweep profile are excluded from the fit so that T_1,w T_2,w and FF values can be fine-tuned. In the second step of the fitting 14 non-saturation phase sweep images (every second data point in the passband) are used to uniquely quantify$T_{1,w}$. In this way, the number of non-saturation images that needs to be acquired is decreased, greatly reducing scan time. The scan time required to collect 50 satureation recovery and 50 non-saturation recovery images is 5 min 44 sec. By reducing the number of non-saturation images to 14, 7, 3 or 1 this time can be reduced to 2 min 23 sec, 1 min 44 sec, 1 min 22 sec, or 1 min 11 sec respectively.

3.4.2 Pulse Sequence Design

All data was acquired on a 1.5T whole body Siemens Sonata MRI scanner (Avanto; Siemens Healthcare; Erlangen, Germany), via a custom single-shot Phase Sweep b-SSFP pulse sequence.

During the b-SSFP sequence T_1 and T_2 relaxation occurs between consecutive excitation pulses resulting in a smooth damping of the magnetization and convergence to a final steady state signal. To decrease acquisition time and maximize SNR, signal was acquired in the transient state. Further, a constant initial magnetization for each image was achieved by applying a saturation pulse (fat and water saturation) at the ECG R wave and allowing 700ms of recovery before imaging. The recovery time of 700ms was chosen to facilitate future application of the method in the heart by allowing one image to be collected every heartbeat during diastole. To increase the recovery time beyond 700ms would double the scan time as one would only be able to image every second heart beat. Saturation prepared transient imaging provides us with increased signal, shorter acquisition time, and also simplifies the T_1 dependence of our characteristic signal profile shape to a simple saturation recovery weighting described by:

$$M_z(t)= M_0*(1- \exp(-t/T_1)) \qquad \text{[Equation 3-5]}$$

where t is the time of recovery after the saturation pulse and M_z is the longitudinal magnetization. At 700ms the fat signal is ~95% recovered; therefore we expect, at most, a small (0.05% for the case of 1% fat fraction) and systematic decrease in the estimated fat.

In order to uniquely quantify $T_{1,w}$, non-saturation images were collected in addition to the saturation recovery image at every RF phase increment. However, the number of non-saturation images required may be greatly reduced in future experiments to save time, and resulting effects on the accuracy and precision of the method have been investigated.

The following acquisition parameters were kept constant for all simulation, phantom and in-vivo phase sweep experiments. TE/TR = 1.35/2.7 ms, 5 mm slice thickness, 192 x 72 acquisition matrix size, 360 x 135 mm field of view, 100% phase resolution, 6/8 partial Fourier, 37.5% fractional phase FOV, 24 lines to the center of k-space (including 5 dummy pulses), flip angle = 70°, 50 phase sweep RF frequency offsets spanning 463Hz, and 700 ms (5 sec) recovery time for saturation prepared (non-saturation) acquisitions. Acquisitions incorporated a variable flip angle (VFA) readout for improved precession (49) and a custom five-pulse saturation train (53) was used (>99% saturation efficiency). Phantom experiments used a 3 cm diameter surface coil for signal reception and in-vivo imaging was performed using a single-element knee coil for excitation and reception.

3.4.3 Monte Carlo Simulations

Monte Carlo simulations (500 repetitions) were conducted in MATLAB to investigate the effects of SNR (20:10:100) on FF, water T_1 and T_2, and off-resonance, for input parameters of FF = [1 5 10] %, water T_1 = [1000 1100 1200] ms, and water T_2 = [30 35 40] ms, and incorporated the exact pulse sequence parameters used in phantom and in-vivo experiments including the distribution of flip angles, and a fat spectral line shape based on an empirically measured peanut oil spectrum (Figure 3.1c). Simulations assumed complete saturation.

Additional Monte Carlo simulations (500 repetitions) were conducted to investigate the sensitivity of the proposed method to the number of non-saturation images collected. The number of non-saturation images used in the fitting of all acquired phantom and in-vivo data was

14 (every second RF pulse phase increment in the pass band). Monte Carlo simulations evaluate the effects of using only 7, 3, and 1 non-saturation images for input FF = 1 %, $T_{1,w}$ = 1100 ms, and $T_{2,w}$ = 35ms.

3.4.4 Phantom Experiments

The dependence of the Phase Sweep b-SSFP method on water T_1 and T_2 was evaluated in eight $NiCl_2$/agarose phantoms with a wide range of water T_1 (340-1130 ms) and T_2 (42-75 ms) values, while the dependence on FF was evaluated in six fat-agarose phantoms doped with $NiCl_2$ (54). Phantoms with FF of [0.09 1.22 3.49 5.77 9.02 11.54]% (as measured with ^{1}H NMR single voxel spectroscopy), included 1% hand soap as an emulsifier and 0.001% $NiCl_2$ by mass to target water T_1 and T_2 values similar to those found in muscle. A more detailed recipe for the construction of the six fat-agarose phantoms is included in Appendix A.

Spin Echo experiments and were used for standard water T1 and T2 measurements. Fat measurements were performed using gradient-echo imaging (GRE) combined with variable projection water/fat estimation (VARPRO) (32) and 1H NMR single voxel spectroscopy experiments. Spin Echo experiments were single echo experiments with 7 TE = [25:25:100 150 200 250] ms, and TR = 10 s. GRE experiments consisted of 6 echo times, TE = [2.55:1.00:7.55] ms, TR=925 ms, 15^0 flip angle, 360 x 135 mm field of view, 192 x 72 matrix and 100% phase resolution performed in a single slice (6 min 40 s acquisition time, with flip angle and TR selected to eliminate T1 weighting for the water signal). Each echo was acquired in a separate TR to minimize eddy-current contamination of phase in sequential echoes and enable the tighter 1 ms inter-echo spacing. VARPRO processing incorporated 6 fat peaks with frequencies of [-3.80, -3.40, -2.60, -1.94, -0.39, 0.60] ppm and respective weightings of [0.087 0.693 0.128 0.004

0.039 0.048]. Single voxel spectroscopy experiments (stimulated echo acquisition mode) with TE = 16 ms, TR = 10 s, 16 averages, 5mm x 5 mm x 5 mm voxel, were repeated with and without water suppression, and the FF was evaluated as the ratio of fat and water peak areas, with correction for the missing fat area in the peaks obscured by water. From the empirically measured peanut oil fat spectra the area of the fat spectra obscured by water is ~6% of the total area under the fat spectra.

3.4.5 In-Vivo Studies

In-vivo experiments were conducted in a single axial slice through the calf muscle of 10 healthy individuals. All study subjects provided written informed consent and the study was approved by the University of Alberta Health Research Ethics Board. Phase sweep b-SSFP experiments, identical to those used for simulations and phantom studies, were acquired with 50 RF phase offsets spanning 460 Hz (1.25 phase sweep profiles) of off-resonance. Full single pixel maps (excluding the tibia, fibula and regions of visceral fat) and regional analysis in the tibialis anterior (TA), soleus (SOL), and gastroc (GAS) muscles were conducted.

VARPRO experiments (identical to phantom studies) were also conducted in all subjects to measure FF and off resonance frequency.

1H NMR single voxel spectroscopy experiments were used for water T_1 and T_2 evaluation and a double angle B_1 map (60^0 and 120^0) was acquired to prevent the dependence of fit parameters on B_1 excite errors. The double angle method acquires 2 images (I_1 and I_2) with flip angles ($\alpha 1$ and $2 \cdot \alpha 1$) respectively while keeping all other sequence parameters the same. The ratio of the magnitude images is given by Eqn. 3-6 where r is the spatial position. Neglecting T_1 and T_2 relaxation the spatially varying flip angle map can be calculated from Eqn. 3.7.

$$\frac{I_{2(r)}}{2I_1(r)} = \frac{\sin(2\alpha_1(r)) f_2(T_1,TR)}{\sin(\alpha_1(r)) f_1(T_1,TR)} = \frac{sin(\alpha_1(r))\cos(\alpha_1(r))}{sin(\alpha_1(r))} = \cos(\alpha_1(r)) \qquad \text{[Equation 3-6]}$$

$$\alpha(r) = \arccos\left(\left|\frac{I_{2(r)}}{2I_1(r)}\right|\right) \qquad \text{[Equation 3-7]}$$

3.5 Results

3.5.1 Monte Carlo Simulations

Monte Carlo results (500 repetitions) in Figure 3.4 show the bias and standard deviations for FF, water T_1 and water T_2 as a function of SNR. No bias is observed, and variability in the fitting shows no dependence on the true FF, T_1, or T_2 value over the range studied. At an SNR of 50/1 the coefficients of variation for water percentage, T_1, and T_2 are approximately 0.003, 0.012 and 0.038 respectively.

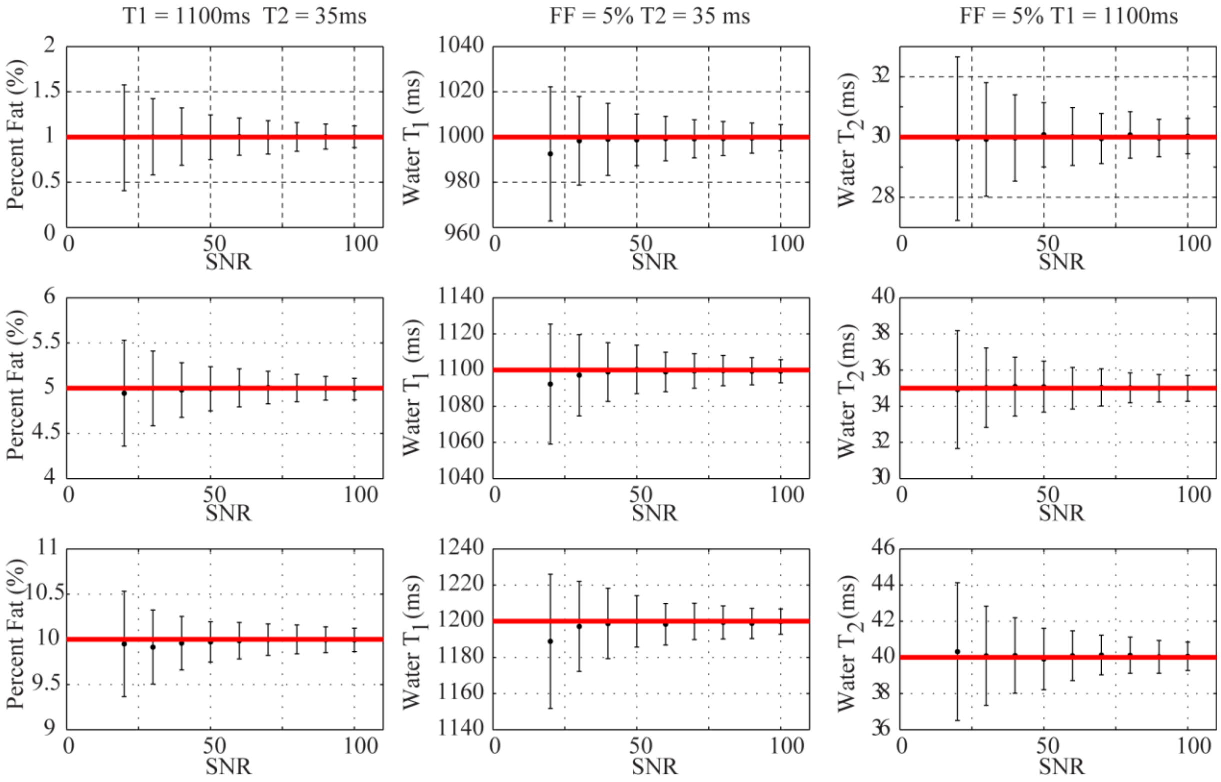

Figure 3.4 Phase Sweep b-SSFP Monte Carlo Simulations. Graphs show mean ± std values for best fit FF (column 1), water T_1 (column 2), and water T_2 (column 3) as a function of SNR (20:10:100). Red lines show the input (true) values.

Monte Carlo results (500 repetitions) in Figure 3.5 show the bias and standard deviations for FF, water T_1 and T_2, and the number of non-saturation images acquired as a function of SNR. As expected FF and water T_2 values are relatively independent of the number of non-saturation phase sweep images acquired. However, variability in the fitting of water T_1 increases as the number of non-saturation images decreases but no bias is observed over the range studied. At an SNR of 50/1 the standard deviations in water T_1 for 7, 3, and 1 non-saturation images are approximately 15, 20, and 30 ms respectively.

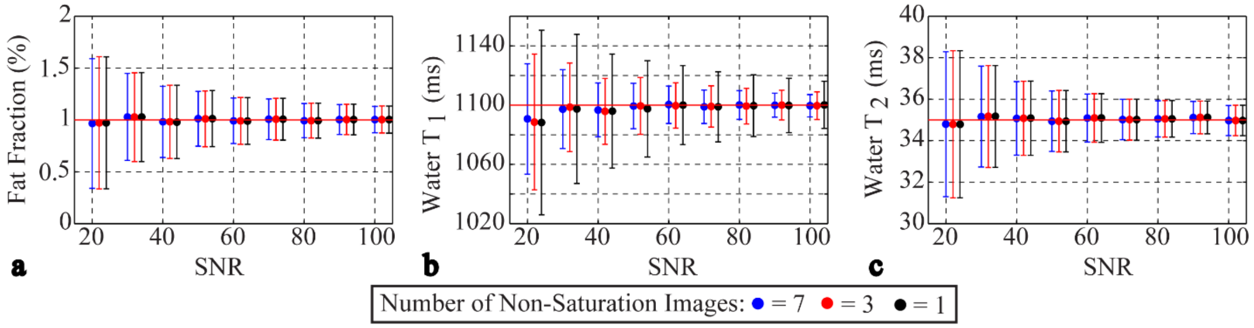

Figure 3.5 Phase Sweep b-SSFP dependence on the number of non-saturation images. Monte Carlo Simulations showing mean ± std values for best fit FF **(a)**, water T_1 **(b)**, and water T_2 **(c)** as a function of SNR (20:10:100) and the number of non-saturation images used in the fitting algorithm. Horizontal red lines show the input (true) values of fat fraction = 1%, water T_1 = 1100 ms, and water T_2 = 35 ms. Data has been shifted relative to the 7 non-saturation image data for improved readability.

3.5.2 Phantom Experiments

Bland and Altman plots of the percent error between Spin Echo and Phase Sweep b-SSFP T_1 and T_2 values are shown in Figure 3.6 for the 8 $NiCl_2$/agarose phantoms. The Phase Sweep b-SSFP method systematically underestimates T_1 by approximately 1.5% but is precise with a standard deviation of only 0.5%. The fitting of T_2 is less precise with a standard deviation of approximately 6%, and a mean overestimation of 2%.

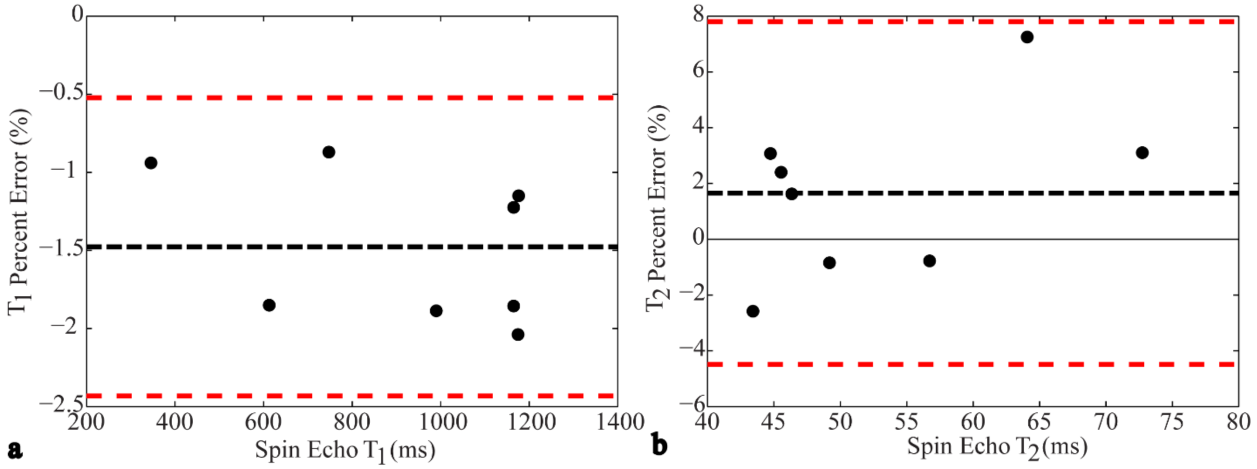

Figure 3.6 T_1 and T_2 Phantom study Bland and Altman Plots. Graphs show percent error of Spin Echo and Phase Sweep water T_1 **(a)** and T_2 **(b)** values for 8 $NiCl_2$/agarose phantoms. Percent Error is defined as (Phase Sweep – Spin Echo)/Spin Echo*100 . Black dashed lines show the mean value, and red dashed lines show ± two standard deviations from the mean.

Spectroscopy and phase sweep values for FF in the 6 fat phantoms are in good agreement (Figure 3.7a) over the range considered. VARPRO was found to overestimate FF at concentrations below 2%. Spectroscopy and phase sweep water T_1 values were also in good agreement (Figure 3.7b) with an R^2 value of 0.96 and the phase sweep values systematically underestimating the water T_1 by ~20 ms. A correlation between phase sweep water T_1 and FF was also observed in the fat phantoms, with higher FF resulting in lower T_1 values. To prove that this correlation was not due to the presence of fat, but instead due to the concentration of agarose (dissolved only in water) being higher in the higher FF phantoms spectroscopy T_1 values were compared to FF in all phantoms and the same correlation was observed.

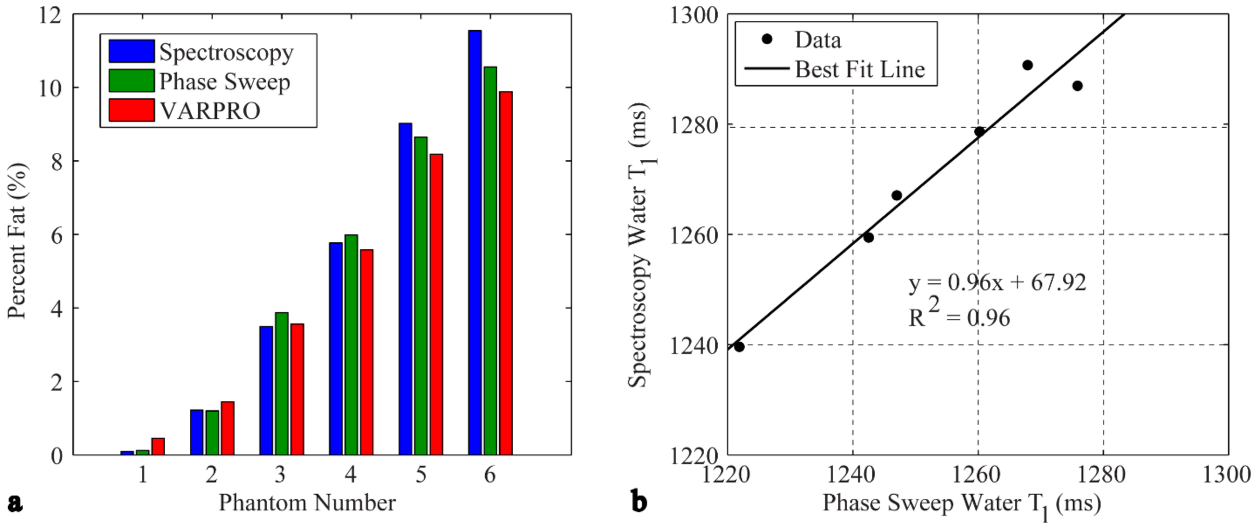

Figure 3.7 **a:** Histogram of Phase Sweep, Spectroscopy and VARPRO fat fraction. **b:** Phase Sweep vs Spectroscopy water T_1 correlation.

3.5.3 In-Vivo Studies

Phase Sweep b-SSFP single pixel maps of water T_1 and T_2, FF, and off-resonance were generated in an axial slice through the calf for all ten subjects. The total acquisition time required to collect all 50 saturation recovery and 50 non-saturation images was 5 min and 43 s.

Figure 3.8a shows the anatomical phase sweep image for a subject at a single off resonance. Figure 3.8b shows the B_1 scaling factor acquired via the double angle method (60° and 120°). As it is known that B_1 varies smoothly over space, the B_1 map has been smoothed by fitting the data with a 2nd order polynomial in two dimensions. B_1 scaling factors across the slice for all subjects ranged from [0.73 to 1.26]. Figure 3.8c and d show the single pixel phase sweep maps of the best fit water T_1 and T_2 values. The larger T_1 values in the SOL and GAS as compared to the TA are in agreement with values previously reported in the calf (55).

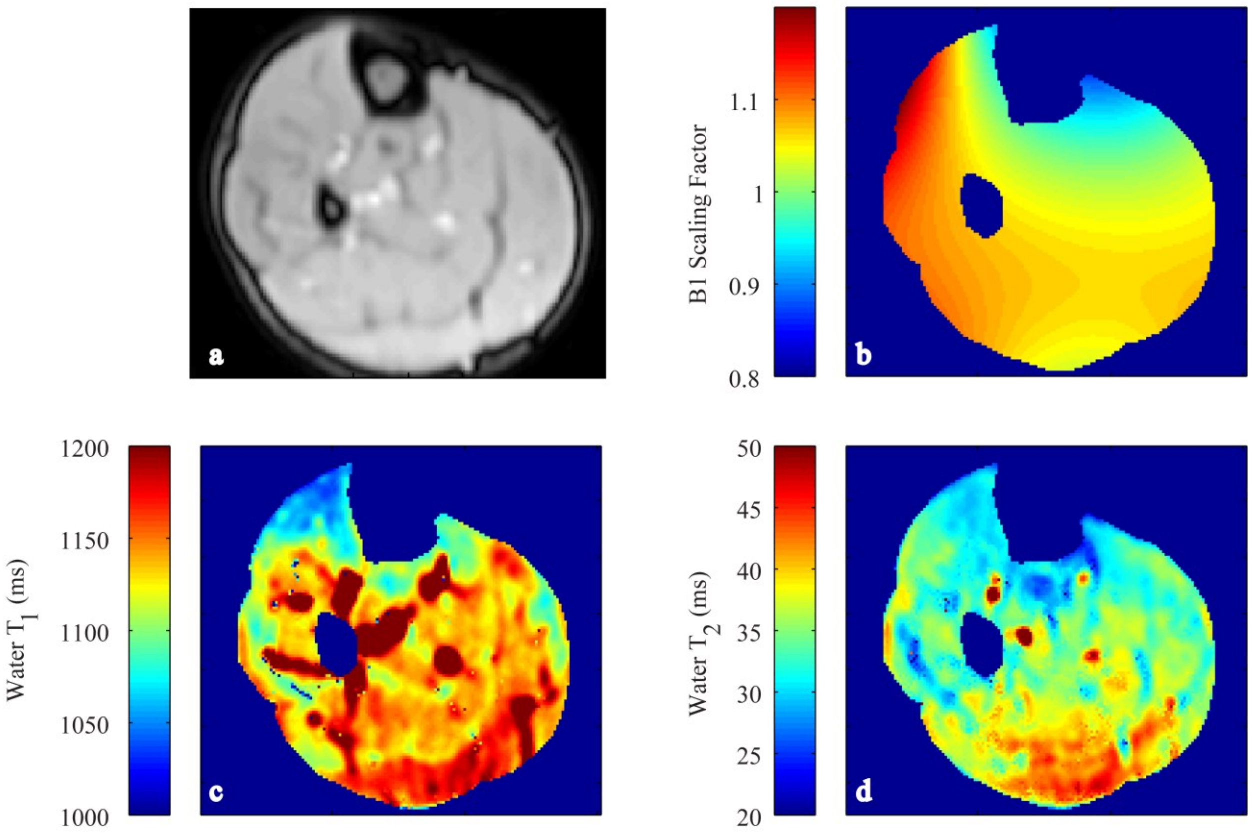

Figure 3.8 Phase Sweep b-SSFP axial calf slice showing the anatomical image **(a),** the double angle b1 map **(b)**, and the water T_1 **(c)** and T_2 **(d)** Phase Sweep pixel maps in a single volunteer.

The mean phase sweep water T_1 and T_2 values in three ROIs located in TA, SOL, and GAS, which correspond to spectroscopy ROIs (5 x 5 x 5 mm voxel), have been calculated for all ten subjects and are compared to the corresponding spectroscopy data in the bland and Altman plot shown in Figure 3.9a and b.

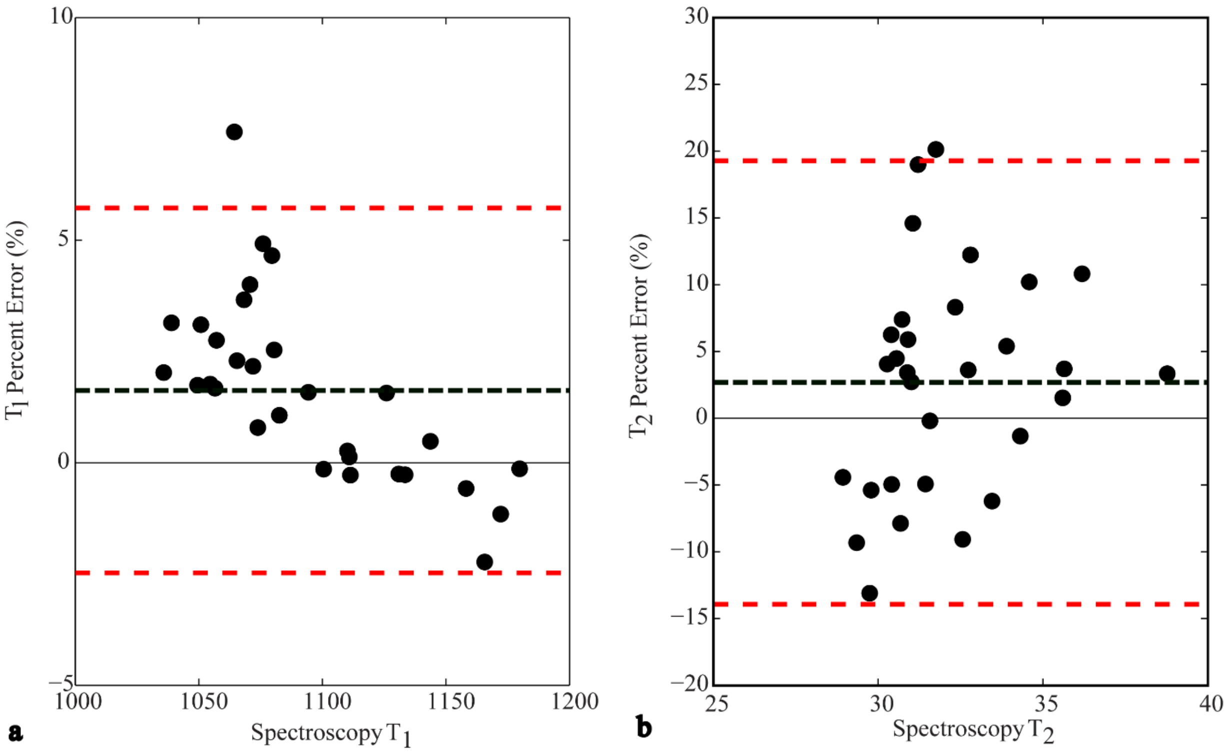

Figure 3.9 TA, SOL and GAS water T_1 and T_2 Bland Altman plots. **a:** the % difference between Spectroscopy and Phase Sweep water T_1 **(a)** and T_2 **(b)** values measured in all ten patients. Percent Error is defined as (Phase Sweep-Spectroscopy)/Spectroscopy·100.

Figure 3.10 compares phase sweep FF and off-resonance measurements to VARPRO measurements. The three main muscle regions (TA, SOL, GAS) are easily differentiated by fat content with the SOL having the highest FF and the TA being the most homogeneous and lowest FF region. As previously observed in the fat phantom experiments VARPRO overestimates areas of low FF (<2%). Off- resonance patterns are similar for both methods, with small discrepancies most likely due to changes in the shim or small shifts in patient positioning between scans.

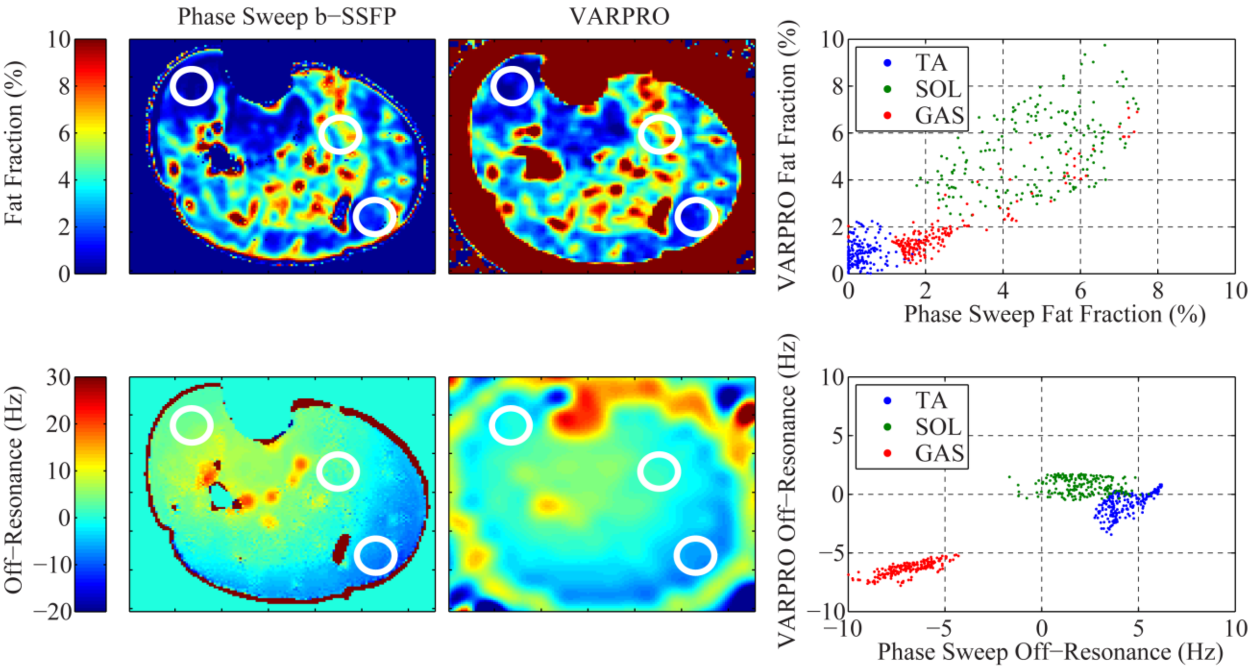

Figure 3.10 Phase Sweep b-SSFP fat fraction and off-resonance vs VARPRO. Phase Sweep b-SSFP (column 1) vs VARPRO (column 2) FF and Off-Resonance maps in rows 1 and 2 respectively. Column 3 shows Phase Sweep vs VARPRO FF and off-resonance frequency correlation plots, where each point is a pixel in the ROIs defined in the pixel maps by white circular regions of interest.

3.6 Discussion

The shape and magnitude of the phase sweep b-SSFP signal profile contains valuable information regarding FF, water T_1, water T_2, and off resonance which can be collected by methodically incrementing the phase of the RF pulse between b-SSFP acquisitions.

The collection of a non-saturation phase-sweep profile reduces the inter-dependency of the fit parameters such that water T_1 is mainly dependent on the difference in signal magnitude between the non-saturation and saturation phase sweep profiles, FF is dependent on the asymmetry observed across the profile, Off-resonance is dependent on the global shift of the profile and water T_2 is dependent on the shape of the profile.

In order to be feasible in the heart, the method must be made into a free breathing sequence. As imaging time is dominated by the number of non-saturation images that are acquired to uniquely characterize water T_1 and because multiple phase sweeps must be acquired to ensure enough data is usable from the free breathing acquisition, the dependence of the multi-parameter fitting on the number of phase sweep points was investigated with Monte Carlo simulations. By reducing the number of non-saturation images from 32 to 3 images in the pass band, the imaging time required can be drastically decreased, with little consequence on results other than a decrease in precision of the water T_1. The resonance frequency of the non-saturation images will be known from the saturation recovery images. From Figure 3.5 we can see that above SNRs of 30/1 the mean T_1 is unaffected, and standard deviations go from [37 45 62] at an SNR of 20/1, to [16 20 33] at an SNR of 50/1, to [8 10 18] at an SNR of 100/1 for 7, 3 and 1, non-sat data points in the pass band respectively.

No in-vivo data from the heart was shown, and thus the viability of using the proposed method in the heart; overcoming confounders such as motion and magnetic field inhomogeneity and transitioning the sequence to a free breathing sequence, has yet to be determined.

3.7 Preliminary Work in Moving Organs

Saturation recovery phase sweep profiles have been collected in the heart and the liver of a single healthy volunteer (Figure 3.11). The data was collected as a free breathing acquisition with three full phase sweeps of data acquired so that there was sufficient data to characterize the profile once data with unmatched respiratory phase was discarded.

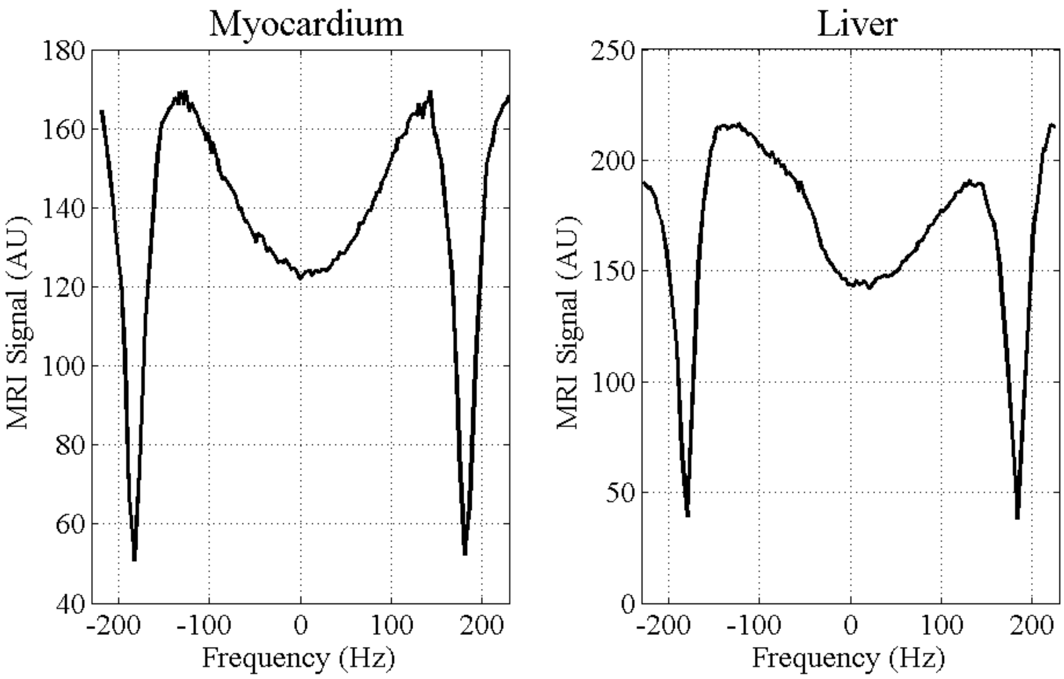

Figure 3.11 Preliminary Phase Sweep b-SSFP data collected using a free breathing acquisition in the Myocardium and Liver of a heathly subject.

Based on the asymmetry of the profiles the FF of the Myocardium was calculated to be 0.4% while the FF in the liver was calculated at 4%. This data is preliminary but shows promise that the transition of the Phase Sweep method to moving organ systems is feasible.

3.8 Conclusions

This study has described and validated a new approach to the simultaneous quantification of FF, water T_1 and T_2, and off-resonance frequency using a saturation-recovery prepared Phase Sweep b-SSFP method. The variability in each parameter is largely independent due to the features of the saturation-recovery phase sweep profile. Specifically, FF is determined by profile asymmetry, T_2 by profile depth (shape), T_1 by saturation recovery weighting, and off-resonance by a global profile shift enabling unique quantification of all parameters. Multi-parameter fitting offers comprehensive tissue characterization in a single acquisition and is relevant in tissues containing fats but in which T_1 and T_2 of the water signal, relative fat content, or off-resonance frequency are targeted.

3.8 Chapter 3 References

1. Ferreira VM, Piechnik SK, Dall'Armellina E, Karamitsos TD, Francis JM, Choudhury RP, Friedrich MG, Robson MD, Neubauer S. Non-contrast T1-mapping detects acute myocardial edema with high diagnostic accuracy: a comparison to T2-weighted cardiovascular magnetic resonance. Journal of Cardiovascular Magnetic Resonance 2012;14(1):42-42.

2. Bull S, White SK, Piechnik SK, Flett AS, Ferreira VM, Loudon M, Francis JM, Karamitsos TD, Prendergast BD, Robson MD, Neubauer S, Moon JC, Myerson SG. Human non-contrast T1 values and correlation with histology in diffuse fibrosis. Heart 2013;99(13):932-937.

3. Zia MI, Ghugre NR, Connelly KA, Strauss BH, Sparkes JD, Dick AJ, Wright GA. Characterizing Myocardial Edema and Hemorrhage Using Quantitative T2 and T2* Mapping at Multiple Time Intervals Post ST-Segment Elevation Myocardial Infarction. Circulation: Cardiovascular Imaging 2012;5(5):566-572.

4. Goodpaster BH, Wolf D. Skeletal muscle lipid accumulation in obesity, insulin resistance, and type 2 diabetes. Pediatric Diabetes 2004;5(4):219-226.

8. Farrell GC, Larter CZ. Nonalcoholic fatty liver disease: From steatosis to cirrhosis. Hepatology 2006;43(S1):S99-S112.

27. Bley TA, Wieben O, Francois CJ, Brittain JH, Reeder SB. Fat and water magnetic resonance imaging. Journal of magnetic resonance imaging : JMRI 2010;31(1):4-18.

32. Hernando D, Haldar JP, Sutton BP, Ma J, Kellman P, Liang ZP. Joint estimation of water/fat images and field inhomogeneity map. Magnetic Resonance in Medicine 2008;59(3):571-580.

45. Messroghli DR, Radjenovic A, Kozerke S, Higgins DM, Sivananthan MU, Ridgway JP. Modified Look-Locker inversion recovery (MOLLI) for high-resolution T1 mapping of the heart. Magnetic Resonance in Medicine 2004;52(1):141-146.

46. Chow K, Flewitt JA, Green JD, Pagano JJ, Friedrich MG, Thompson RB. Saturation recovery single-shot acquisition (SASHA) for myocardial T1 mapping. Magnetic Resonance in Medicine 2014;71(6):2082-2095.

49. Chow K, Spottiswoode BS, Pagano JJ, Thompson RB. Improved precision in SASHA T1 mapping with a variable flip angle readout. Journal of Cardiovascular Magnetic Resonance 2014;16(Suppl 1):M9.

50. Scheffler K, Lehnhardt S. Principles and applications of balanced SSFP techniques. European radiology 2003;13(11):2409-2418.

51. Miller KL. Asymmetries of the balanced SSFP profile. Part I: theory and observation. Magnetic Resonance in Medicine 2010;63(2):385-395.

52. Yu H, Shimakawa A, McKenzie CA, Brodsky E, Brittain JH, Reeder SB. Multiecho water-fat separation and simultaneous R2* estimation with multifrequency fat spectrum modeling. Magnetic Resonance in Medicine 2008;60(5):1122-1134.

53. Chow K, Kellman P, Spottiswoode BS, Nielles-Vallespin S, Thompson RB. Optimized saturation pulse trains for SASHA T(1) mapping at 3T. Journal of Cardiovascular Magnetic Resonance 2015;17(1):W20.

54. Kraft KA, Fatouros PP, Clarke GD, Kishore PRS. An MRI phantom material for quantitative relaxometry. Magnetic Resonance in Medicine 1987;5(6):555-562.

55. Machann J, Bachmann OP, Brechtel K, Dahl DB, Wietek B, Klumpp B, Haring HU, Claussen CD, Jacob S, Schick F. Lipid content in the musculature of the lower leg assessed by fat selective MRI: intra- and interindividual differences and correlation with anthropometric and metabolic data. Journal of magnetic resonance imaging : JMRI 2003;17(3):350-357.

Chapter 4. Characterization of T_1 Bias from Fat in MOLLI and SASHA Pulse Sequences: Quantitative Fat-Fraction Imaging with T_1 Mapping

4.1 Abstract

Purpose: Characterize the effects of fat on commonly used T_1 mapping sequences and evaluate a new method for quantitative fat-fraction imaging, for low fractions (0-10%), based on the modulation of T_1 values by the fat pool.

Methods: Bloch equation simulations, phantom and in-vivo (skeletal muscle) experiments were used to characterize the response of commonly used T_1 mapping sequences (SASHA and MOLLI) to fat-water systems with known fat-fractions (0-10%), at 1.5T. Fat-fractions were measured with single voxel spectroscopy and Dixon imaging methods. A new T_1-based fat-fraction imaging method was evaluated using Monte Carlo simulations and phantom/in-vivo experiments.

Results: SASHA and MOLLI have similar T_1 dependence on fat-fraction, with characteristic under- or overestimation of T_1 values as a function of off-resonance frequency (30-70ms variation in native T_1 per 1% fat-fraction). Fat-fraction maps generated from the 2-parameter SASHA method yielded a low variability of ±0.25% for a signal to noise ratio of 150 to 1 in the non-saturation image with good agreement to spectroscopy.

Conclusions: Low fat-fractions result in relatively large negative or positive shifts in native tissue T_1 measured with MOLLI and SASHA over a narrow range of off-resonance frequencies; T_1 shifts from fat can be used to accurately quantify fat-fraction.

4.2 Introduction

Quantitative imaging of the myocardial longitudinal relaxation time constant (T_1) is increasingly used to evaluate pathology related to edema (1) and fibrosis (2), where changes in T_1 values reflect changes in the water mobility. However, when fat is a signal source in the voxel of interest, the resulting apparent T_1 value will be a complex function of water and fat content and the methods used for T_1 acquisition and processing. The complex response of mixed water and fat systems to the commonly used MOdified Look-Locker Inversion recovery (MOLLI) (45) and SAturation recovery single-SHot Acquisition (SASHA) (46) methods has recently been described in skeletal muscle (56) and for high concentration extracellular fat pools, in myocardial scar (e.g. lipomatous metaplasia in replacement fibrosis) and endocardial fat (57). These studies illustrated the potential for either increased or decreased best-fit T_1 values in mixed water-fat systems as a function of off-resonance frequency when using MOLLI and SASHA methods. These characteristic responses were shown to be a consequence of the b-SSFP readout used in these sequences.

However, the effects of lower FF, in the 0-10% range, and their relationship with the best-fit T_1 values for the commonly used variations of T_1 mapping methods remains to be characterized. The potential for relatively large shifts in T_1 values per FF, as much as 50 ms per 1% FF (56), suggest that increased intracellular FF found in common conditions such as diabetes, and obesity could have important effects (i.e. tens of ms) on globally measured native myocardial T_1 values. The expected shift in T_1 values as a function of FF, pulse sequence parameters, SNR, and post-processing methods (e.g. two-parameter or three-parameter fitting in saturation recovery imaging) remains unknown. The primary goals of the current study were to characterize the dependence of MOLLI and SASHA T_1 mapping sequences on FF for low FF values (0-10%) and to illustrate a novel sensitive method for FF quantification using these T_1 mapping sequences.

4.3 Theory

SASHA (46) and MOLLI (45) T_1 mapping sequences consist of preparation pulses followed by sampling of the T_1 recovery curve with multiple ECG-triggered single-shot images acquired at the same cardiac phase in sequential heartbeats. Despite differences in patterns of preparation pulses and how the recovery data is sampled with these methods, they are both based on a b-SSFP image acquisition. Thus, in order to evaluate the effects of fat on the best-fit T_1 values, the response of mixed water and fat spin systems to the b-SSFP pulse sequence must first be considered. In particular, the off-resonance frequency response of water and fat to the b-SSFP sequence is required, given the chemical shift difference between the water and fat spin systems and the broad range of frequencies in the fat spectrum. Even for the simple water spin system, the b-SSFP signal intensity varies strongly as a function of off-resonance frequency (Figure 4.1) (51,58). Note that Figure 4.1 is identical to Figure 3.1, duplicated here for ease of reference. The signal profile exhibits a phase inversion in sequential "b-SSFP bands" every 1/TR Hz, where TR is the repetition time between sequential excitations. Equivalently, this signal profile can be acquired by collecting multiple b-SSFP images with different RF pulse phase increments, where the conventional 180° increment per sequential RF pulse corresponds to the on-resonance excitation (51).

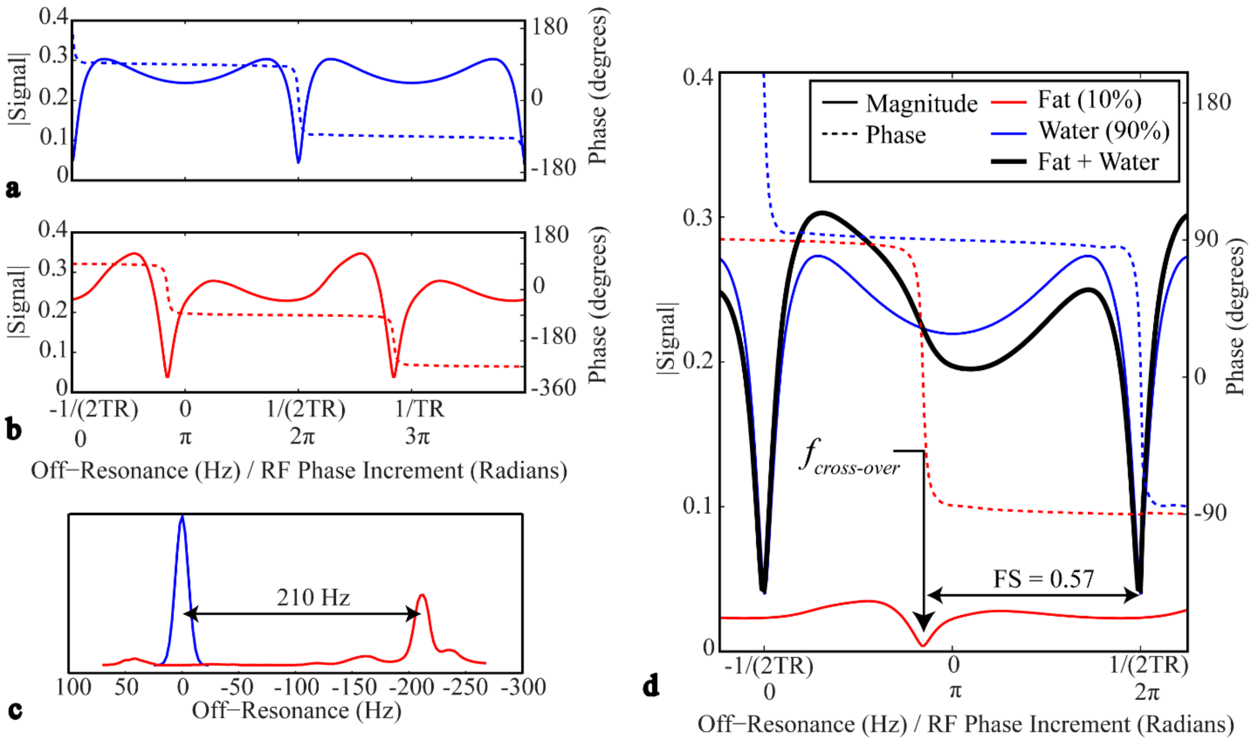

Figure 4.1. Phase sweep profile interference. Sample b-SSFP phase sweep profiles (solid = magnitude, dashed=phase) for water **(a)** and fat **(b)**. **c:** Water (blue) and fat (red) spectral line shapes, normalized to a unity area. **d:** Sample b-SSFP phase sweep profile for water (blue), fat (red), and their sum (black), showing constructive and destructive interference in the combined profile (10% fat fraction). The fractional shift (FS) between the water and fat profiles is 0.57, where FS = 1 is the distance between black bands. All plots are for 1.5T and a TR of 2.7 ms.

In Figure 4.1b, the fat signal profile in response to the b-SSFP sequence exhibits asymmetry due to the multiple resonance frequencies in the fat spectrum. The total signal profile is a weighted sum of profiles from each frequency in the spectrum. Water and fat spectra used to generate these b-SSFP signal profiles are shown in Figure 4.1c. A symmetric Gaussian shape was used for the water spectrum and the fat spectrum was modeled on an empirically measured peanut oil spectrum, which has been shown to be a good model for in-vivo fat (52). Importantly, the fat and water spectra are offset in the frequency direction by the chemical shift difference of 3.3 ppm (-210 Hz) between the water (4.7 ppm) and fat spectra (main peak at 1.4 ppm). The relative frequency shift between water and fat b-SSFP signal profiles is a function of field strength and TR, where the fractional shift (FS) is given by FS = 42.576 MHz T^{-1} · 3.3 ppm · B_0 ·TR = 140.5 Hz T^{-1} · B_0 · TR, where FS = 1 corresponds to the two profiles being completely out of phase (i.e. black bands aligned but with a 180° phase shift). The example in Figure 4.1 is for FS = 140.5 Hz T^{-1} · 1.5T· 0.0027 s = 0.57, as indicated in Figure 4.1d. When combined, the relative shifts of the water and fat b-SSFP signal profiles yields constructive or destructive interference between the water and fat due to the phase inversion in sequential bands (Figure 4.1d). The location of the phase cross-over, where the fat signal profile has a phase inversion, can be defined as $f_{\text{cross-over}}$ = (0.5 · TR^{-1} - 42.576 MHz T^{-1} · 3.3 ppm · B_0 -) = -26 Hz for TR = 2.7 ms, relative to the water resonance frequency, with repeated patterns every 1/TR Hz. The term 0.5 · TR^{-1} corresponds to the frequency shift from the center of a b-SSFP band to the closest black band. The response of such composite water-fat systems to MOLLI and SASHA pulse sequences, as a function of off-resonance frequency, is considered below.

4.4 Methods

Bloch equation simulations, phantom and in-vivo experiments were used to evaluate the response of fat and water systems (0-10% FF) to the SASHA and MOLLI pulse sequences. Phantom data and in-vivo data from skeletal muscle (calf) were acquired to determine the relationship between FF and the resulting T_1 offsets (i.e. the change in best-fit T_1 as a result of the FF), with standard FF values measured using ^{1}H NMR spectroscopy and a Dixon-based method (VARPRO) (32), for ranges of FF from near zero to ~10%. Based on the relationship between the fat-induced T_1 offsets and FF, a new method for FF imaging using the SASHA T_1 mapping method is proposed and validated. Monte Carlo simulations of the SASHA pulse sequence were used to evaluate the effect of the saturation recovery sampling scheme on the derived FF, and to characterize FF variability as a function of SNR, with further validation of FF quantification in phantoms and in-vivo, in skeletal muscle.

All experiments were conducted on a 1.5T Siemens Sonata MRI Scanner (Avanto; Siemens Healthcare; Erlangen, Germany). An identical b-SSFP readout was used for all simulation, phantom and in-vivo experiments for both SASHA and MOLLI. Specifically, TE/TR = 1.35/2.7 ms, 5 mm slice thickness, 192 x 72 acquisition matrix size, 360 x 135 mm field of view, 100% phase resolution, 6/8 partial Fourier, 37.5% fractional phase FOV, 24 lines to the center of k-space (including 5 dummy pulses), and 35° flip angle (MOLLI) or 70° flip angle (SASHA). SASHA acquisitions and simulations used a non-saturation image and 9 saturation recovery (TS) times, with TS = 144 ms in steps of 71 ms to 712 ms, and incorporated a variable flip angle (VFA) readout (49). A custom five-pulse saturation train (53) was used for SASHA experiments (to ensure >99% saturation efficiency). MOLLI acquisitions and simulations included a single Look-Locker set with an initial inversion delay of 32.6 ms imaging delay and an effective heart rate of 66 beats per minute for TI times of 95.3 ms in steps of 910.15 ms to 3735.90 ms. Phantom experiments used a 3 cm diameter surface coil for signal reception and in-vivo imaging was performed using a single-element knee coil for excitation and reception.

4.4.1 Bloch Equation Simulations

SASHA and MOLLI Bloch equation simulations were conducted in MATLAB R2013a (The MathWorks; Natick, MA) using the Matlab MEX function created by Brian Hargreaves and shared at http://mrsrl.stanford.edu/~brian/blochsim/ for FF = 0%, 2%, 4%, 6%, 8% and 10% and incorporated the exact pulse sequence parameters used in phantom and in-vivo experiments, including the distribution of flip angles (slice profile effects), and a fat spectral line shape based on an empirically measured peanut oil spectrum (Figure 4.1c). The same peanut oil was used for the construction of fat-agarose phantoms. For simulations, T_1 and T_2 values of fat were specified at 250 and 50 ms respectively while the T_1 and T_2 of water were specified at 1100 and 35 ms, similar to skeletal muscle values (59,60).

SASHA Bloch equation simulations assumed complete saturation following the saturation pulse. A VFA readout was used to minimize signal oscillations in the approach to steady-state and associated artifacts (49). For the VFA readout, the flip angle, α, of the first 29 RF pulses were scaled by sin(x) where $\pi/90 < x < \pi/2$. Data was not acquired for the first 5 pulses and an $\alpha/2$ closer pulse was used at the end of the image readout. The 10 ms adiabatic inversion pulse (hyperbolic secant) used for the MOLLI experiments was numerically simulated with Bloch equation simulations to determine the initial longitudinal magnetization following inversion preparation (61).

4.4.2 T_1 Calculation

The calculation of T_1 values for simulation, phantom and in-vivo experiments was performed offline using MATLAB. All SASHA and MOLLI simulations and experimental acquisitions were repeated with 30 different off-resonance frequencies, spanning 460 Hz of off-resonance (~15 Hz increments), which is 1.25 times the frequency difference between sequential b-SSFP dark bands for TR = 2.7 ms (to ensure full frequency sampling of the central b-SSFP band). For these, and all experiments in this study, the effects of off-resonance frequency were implemented by modulating the phase-increment between sequential RF pulses. For each experiment, at a given off-resonance frequency, T_1 values were calculated by fitting signal intensities with the standard Look-Locker correction (Eqn. 4-1) (45,62) (MOLLI) and both 2- and 3-parameter exponential models (Eqn. 4-2) (46) (SASHA). SASHA 2-parameter (SASHA-2p) fitting assumed ideal saturation ($\eta = 1$) while SASHA three parameter (SASHA-3p) fitting included saturation efficiency as a fitting variable. SASHA-2p fitting is of particular interest as it significantly reduces the variability in best-fit T_1 values as compared to SASHA-3p (42). The mono-exponential equations used for calculating MOLLI and SASHA T_1 values are defined, respectively, as:

$$signal = A - Be^{-\frac{TI}{T_1^*}}, \text{ where } T_1 = \left(\frac{B}{A} - 1\right) T_1^*, \text{ and} \qquad \text{[Equation 4-1]}$$

$$signal = A\left(1 - \eta e^{-\frac{TS}{T_1}}\right). \qquad \text{[Equation 4-2]}$$

where $(BA^{-1} - 1)$ is the Look-Locker correction factor, TI is the inversion recovery time, and TS is the saturation recovery time (from the end of preparation pulse to central line of k-space). A Levenberg-Marquardt algorithm (63) was used to determine the best fit values independently for each frequency increment across the band.

4.4.3 Phantom Experiments

The dependence of SASHA and MOLLI sequences on FF was evaluated in six fat-agarose phantoms doped with $NiCl_2$ (54). Phantoms with fat concentrations of 0.09%, 1.22%, 3.49%, 5.77%, 9.02% and 11.54% (as measured with ^1H NMR single voxel spectroscopy) included 1% hand soap as an emulsifier, 2.5% agarose and 0.001% $NiCl_2$ by mass to target water T_1 and T_2 values similar to those found in muscle. A more detailed recipe for the construction of the six fat-agarose phantoms is included in Appendix A.

SASHA and MOLLI experiments, with sequence parameters identical to Bloch equation simulations described above, were performed in all phantoms. Additionally, fat measurements were performed using gradient-echo imaging (GRE) combined with variable projection water/fat estimation (VARPRO) (32) , and ^{1}H NMR single voxel spectroscopy experiments. GRE experiments consisted of 6 echo times, TE = 2.55 ms in 1.0 ms steps to 7.55 ms, TR = 925 ms, 15° flip angle, 360 x 135 mm field of view, 192 x 72 matrix and 100% phase resolution performed in a single slice (6 min 40 s acquisition time, with flip angle and TR selected to eliminate T_1 weighting for the water signal). Each echo was acquired in a separate TR to minimize eddy-current contamination of phase in sequential echoes and enable the tighter 1 ms inter-echo spacing. VARPRO processing incorporated 6 fat peaks with frequencies of [-3.80, -3.40, -2.60, -1.94, -0.39, 0.60] ppm and respective weightings of [0.087 0.693 0.128 0.004 0.039 0.048]. Single voxel spectroscopy experiments (stimulated echo acquisition mode) with TE = 16 ms, TR = 10 s, 16 averages, 5 x 5 x 5 mm voxel, were repeated with and without water suppression, and the FF was evaluated as the ratio of fat and water peak areas, with correction for the missing fat area in the peaks obscured by water. From the empirically measured peanut oil fat spectra the area of the fat spectra obscured by water is ~6% of the total area under the fat spectra.

4.4.4 In-Vivo Studies

In-vivo experiments were conducted in a single axial slice through the calf muscle in 10 healthy individuals. All study subjects provided written informed consent and the study was approved by the University of Alberta Health Research Ethics Board. SASHA and MOLLI experiments, identical to those used for simulations and phantom studies, were performed in all subjects.

SASHA and MOLLI T_1 pixel maps were generated at 30 frequency offsets spanning 460 Hz of off-resonance, as described in the simulations sections. The tibia, fibula and regions of visceral fat were excluded prior to T_1 fitting. The total acquisition time required to collect SASHA and MOLLI data at the 30 frequency offsets was 8 min 22 s for SASHA and 8 min 43 s for MOLLI. VARPRO experiments (identical to phantom studies) were also conducted in all subjects. For data analysis, several small circular regions of interest (0.9 cm^2) were selected in each subject, in all muscle groups, which were copied to all SASHA, MOLLI and VARPRO images, to allow direct comparison between methods. All images were registered to correct for subject shifting between acquisitions.

4.4.5 Monte Carlo Simulations

Monte Carlo simulations (500 repetitions) were performed for SASHA-2p and 3p methods to investigate the effects of noise and different TS sampling schemes on the modulation of T_1 values associated with increasing FF (0-10%). Signal to noise ratios, defined as the SNR for the non-saturation b-SSFP image, ranging from 20 to 300 were considered. In addition to the TS sampling scheme used in all simulations and experiments above (TS = 144 ms in steps of 71 ms to 712 ms), additional schemes varied the maximum TS times (from 800 ms down to 300 ms in 100 ms increments), corresponding to an increase in heart rate up to 120 BPM. For all cases, 9 saturation recovery images with equally spaced TS times from 100 ms up to maximum TS were used in combination with a non-saturation prepared image. Additionally, the SASHA-2p approach with a single TS (repeated 9 times), as opposed to a range of TS times, was also considered as it has been shown to decrease variability in best-fit T_1 values with the SASHA method (64). Specifically, for native T_1 values in the range of skeletal and cardiac muscle, 1100-

1200 ms, the optimum TS times for a single-TS acquisition of 600 ms (for 60 BPM heart rate) and 350 ms (120 BPM), were evaluated (64). Additionally, the effects of the underlying water T_1 (1000 to 1300 ms) and fat T_1 values (200 to 300 ms) as well as offsets in resonance frequency due to imperfect B_0 shimming (-50 to +50 Hz) were evaluated. The MOLLI method was not evaluated with Monte Carlo simulations or as a method for quantitative FF imaging in the current study due to the much more complex T_1 dependence of this method on factors such as inversion pulse efficiency, magnetization transfer and other effects (42), including off-resonance frequency (65).

4.4.6 Fat-Fraction Imaging with T_1 Mapping

The proposed FF imaging method is based on the characteristic response of mixed fat and water systems to b-SSFP based T_1 mapping method, where both positive and negative T_1 shifts are observed, as a function of off-resonance frequency. Figure 4.2 shows a schematic of the proposed method, where the maximum T_1 difference measured for a given FF, defined as ΔT_1, is used to quantify the underlying FF giving rise to the frequency dependent T_1 variations. A minimum of two repeated T_1 mapping experiments, at targeted off-resonance frequencies, are required to calculate ΔT_1. Monte Carlo simulations, described above, were used to determine the relationship between ΔT_1 and FF for SASHA-2p and 3p, for the wide range of SNR values and experimental parameters outlined above, for the purpose of evaluating precision and accuracy of this proposed method.

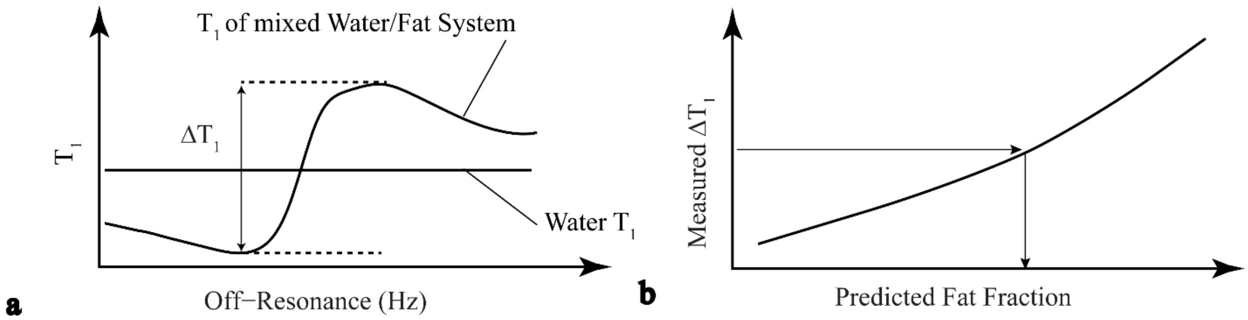

Figure 4.2. Fat Fraction Quantification with T_1 mapping. **a:** The off-resonance dependence of T_1 values in mixed water and fat systems gives rise to a positive and negative offsets from the water T_1 and a total difference, ΔT_1, between minimum and maximum values. **b:** The proposed fat fraction (FF) imaging method using T_1 mapping is based on a predicted relationship between ΔT_1 and FF which allows measured ΔT_1 values to be converted to FF values.

4.5 Results

4.5.1 Bloch Equation Simulations and Phantom Experiments

Figure 4.3 summarizes the simulation and phantom T_1 responses as a function of FF and off-resonance frequency for SASHA and MOLLI sequences. Spectroscopy data was used to define FF for the phantoms. For all cases, the offset in best-fit T_1 from the true water T_1 is negative when water and fat b-SSFP signals are in-phase and positive when water and fat are out of phase, with larger T_1 offsets with increasing FF, as indicated in Figure 4.3. The proposed parameter for imaging of FF, ΔT_1, is defined in the upper left panel. Note that the underlying water T_1 from the phantoms is ~1300 ms, as compared to 1100 ms in the simulations.

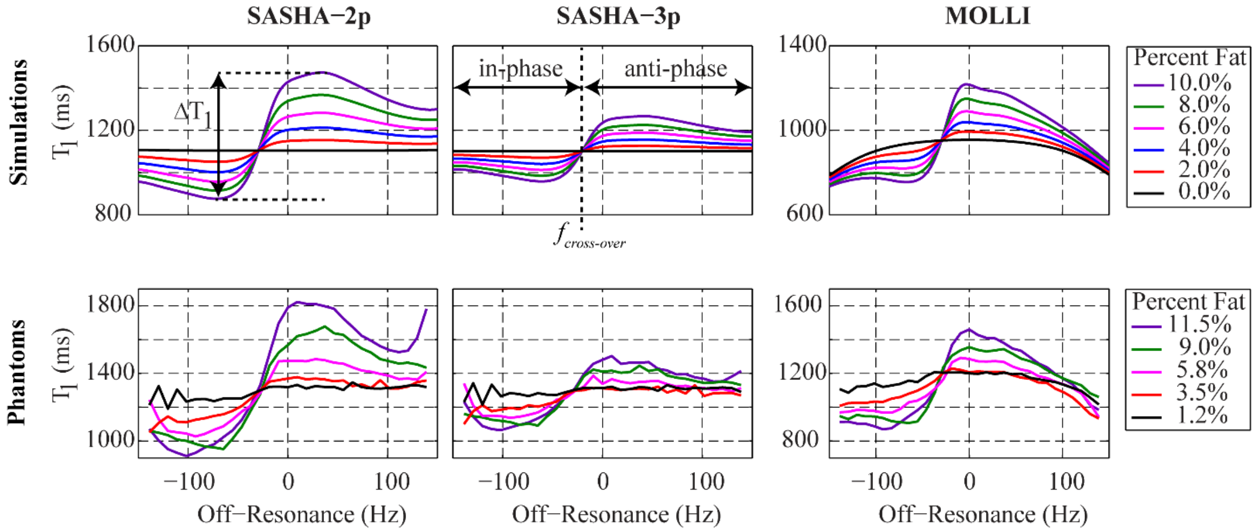

Figure 4.3. SASHA and MOLLI T_1 vs off-resonance. Characterization of T_1 vs off-resonance for SASHA and MOLLI as a function of fat percentage for Bloch equation simulations and phantom experiments. Phantom fat percentages were measured via spectroscopy. Note that simulated water T_1 values were 1100 ms while the water T_1 in the phantoms was ~1300 ms.

The best-fit T_1 values have similar frequency responses for simulation and phantom data for all sequences, and the $f_{\text{cross-over}}$, between negative and positive T_1 offsets for all simulations and phantom data occurs at ~ -26 Hz, as expected. Note that off-resonance values were used to define the zero point of the frequency axis. The SASHA-2p fitting has a larger T_1 shift per FF than the SASHA-3p fitting, with MOLLI values in between these two SASHA variants. MOLLI T_1 values have an additional and previously characterized intrinsic dependence on off-resonance resulting in an underlying domed shape with reduced T_1 values with increasing off-resonance frequency (Figure 4.3) (66). Figure 4.4a compares the measured ΔT_1, the difference in T_1 at -70 Hz and +30 Hz, for SASHA and MOLLI phantom data, for FF values of 0.1%, 1.2%, 3.5%, 5.8%, 9.0% and 11.5% in phantoms 1 to 6, respectively.

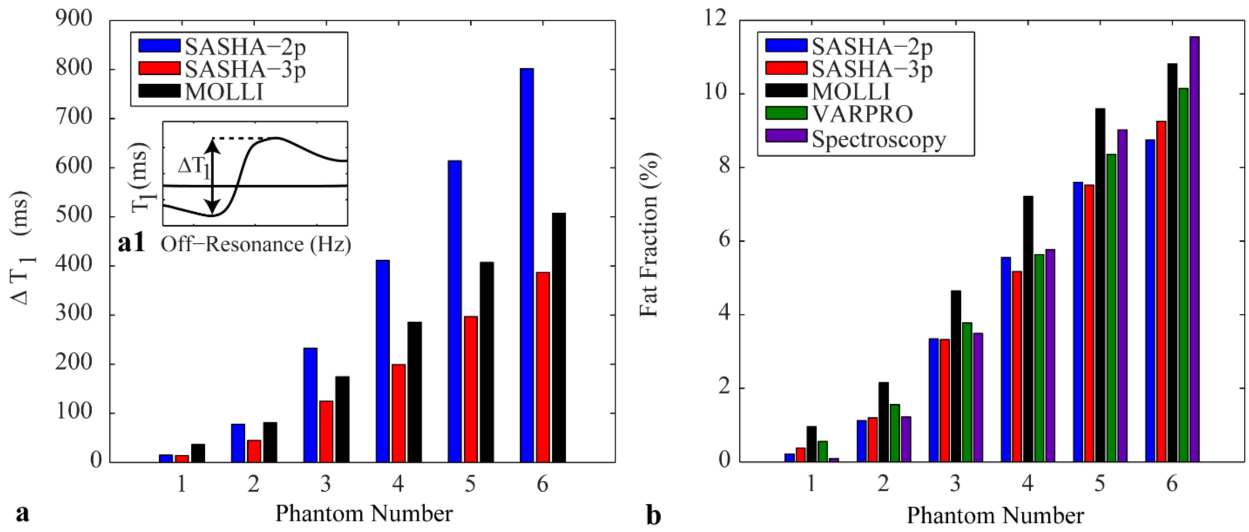

Figure 4.4. Phantom ΔT_1 and Fat Fraction. **a:** Comparison of ΔT_1 for SASHA-2p, SASHA-3p and MOLLI methods in the six fat phantoms, for which FF = [0.1 1.2 3.5 5.8 9.0 11.5]%. **b:** Comparison of FF, derived from ΔT_1 values, for SASHA-2p, SASHA-3p and MOLLI methods as well as single voxel spectroscopy and VARPRO.

4.5.2 In-Vivo Studies

Skeletal muscle experiments show similar patterns to simulations and phantoms, with the same sigmoidal T_1 response to off-resonance frequency. Columns 1 and 2 in Figure 4.5 show calf T_1 pixel maps in a representative subject at the acquired off-resonance frequencies of -70 and +30 Hz, for SASHA-2p, SASHA-3p and MOLLI, in rows 1 to 3, respectively. Columns 3 and 4 show the T_1 frequency responses from two sample regions of interest, in the tibialis anterior and soleus, respectively. MOLLI underestimates water T_1 values, by ~250 ms, as a consequence of non-ideal inversion pulse efficiency, magnetization transfer and other effects (42), and has a characteristic domed response to off-resonance frequency (66). The much larger range of T_1 values, ΔT_1, in the soleus relative to the tibialis anterior are in agreement with the higher FF values previously reported in the soleus (55).

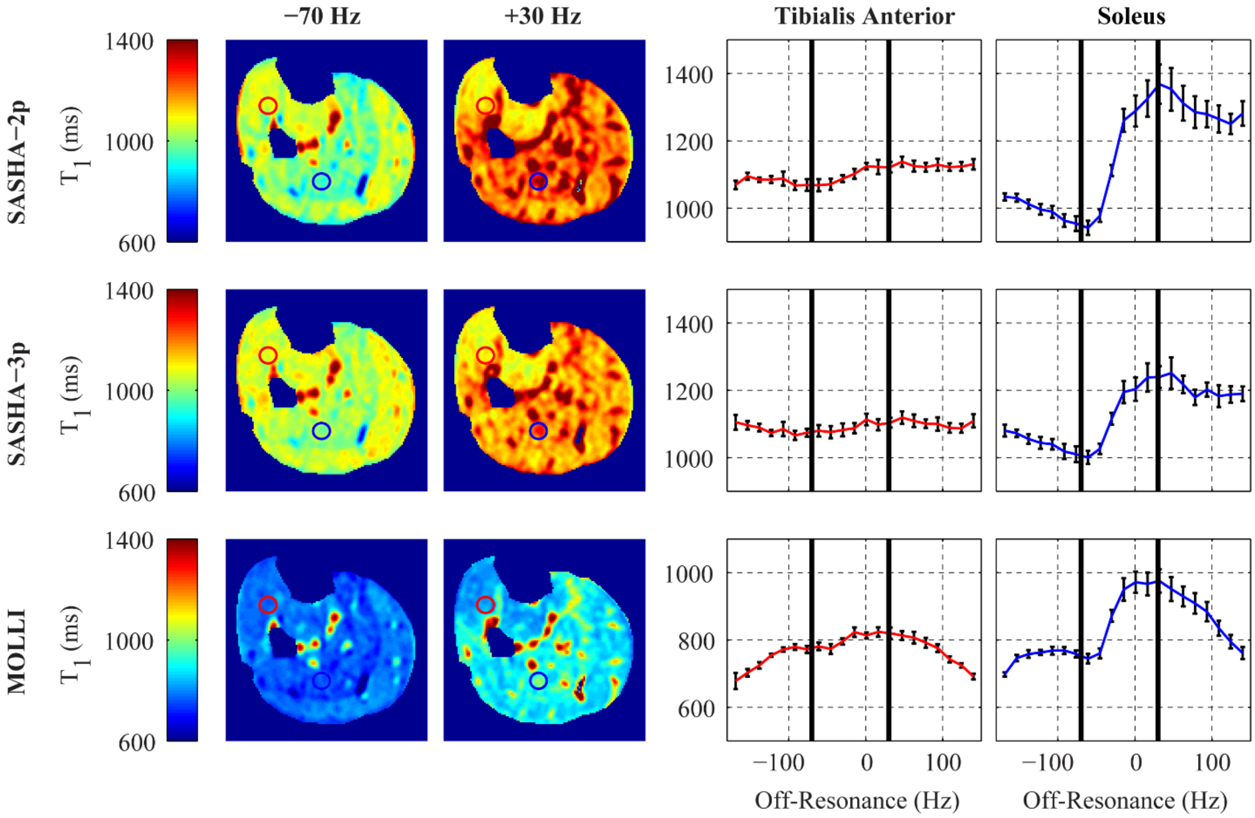

Figure 4.5. In-vivo T_1 maps for different off-resonance frequencies. In-Vivo pixel T_1 maps of an axial slice through the calf for off-resonance frequencies of -70 and +30 Hz. The circles indicate the regions of interest used to generate the T_1 vs off-resonance frequency curves shown in columns 3 (tibialis anterior) and 4 (soleus). Vertical black lines show the frequencies -70 and +30 Hz, at which the images are measured.

Multi-echo GRE data with VARPRO processing was used for in-vivo FF estimation, as a reference for comparison with ΔT_1. VARPRO FF and T_1-mapping derived ΔT_1 were measured in multiple regions of interest in all 10 subjects, with results shown in Figure 4.6a and b, for SASHA-2p, SASHA-3p and MOLLI experiments. The predicted relationship between FF and ΔT_1, for water T_1 = 1100 ms and fat T_1 = 250 ms, are plotted as solid lines in Figure 4.6a and b. There is good overall agreement for SASHA-2p and SASHA-3p experiments and a similar linear trend for MOLLI but with a significant bias which presented as a downward shift in ΔT_1 by ~30 ms as compared to numerical simulations. The theoretical line for MOLLI does not pass through the origin due to MOLLI's intrinsic dependence on off-resonance (66).

4.5.3 Monte Carlo Simulations

The variability in T_1 and ΔT_1 as a function of SNR for SASHA is summarized in Figure 4.7, for the case of 1% FF. SASHA-2p fitting yields a larger ΔT_1 as well as smaller variability in the calculated T_1 values, relative to SASHA-3p calculations. The mean ΔT_1 (i.e. the difference between minimum and maximum T_1 values) calculated by both methods is independent of SNR for the range of values considered. However, as shown in Figure 4.8, the magnitude of the calculated ΔT_1 per FF is dependent on the TS sampling scheme. Figure 4.8 shows the simulated $\Delta T_{1,}$ using T_1 maps at two off-resonance frequencies (-70 Hz, +30Hz), vs. FF for variations in the TS times, for SASHA-2p and SASHA-3p methods. For all sequence variants, smaller maximum TS times give rise to larger ΔT_1 values for a given FF, but also have increased variability in ΔT_1. The resulting variability in derived FF for SASHA-2p is largely independent of the maximum TS time (Figure 4.8d), while SASHA-3p is dominated by increased variability in ΔT_1 at shorter maximum TS times causing the uncertainty in FF to be increased with reduced

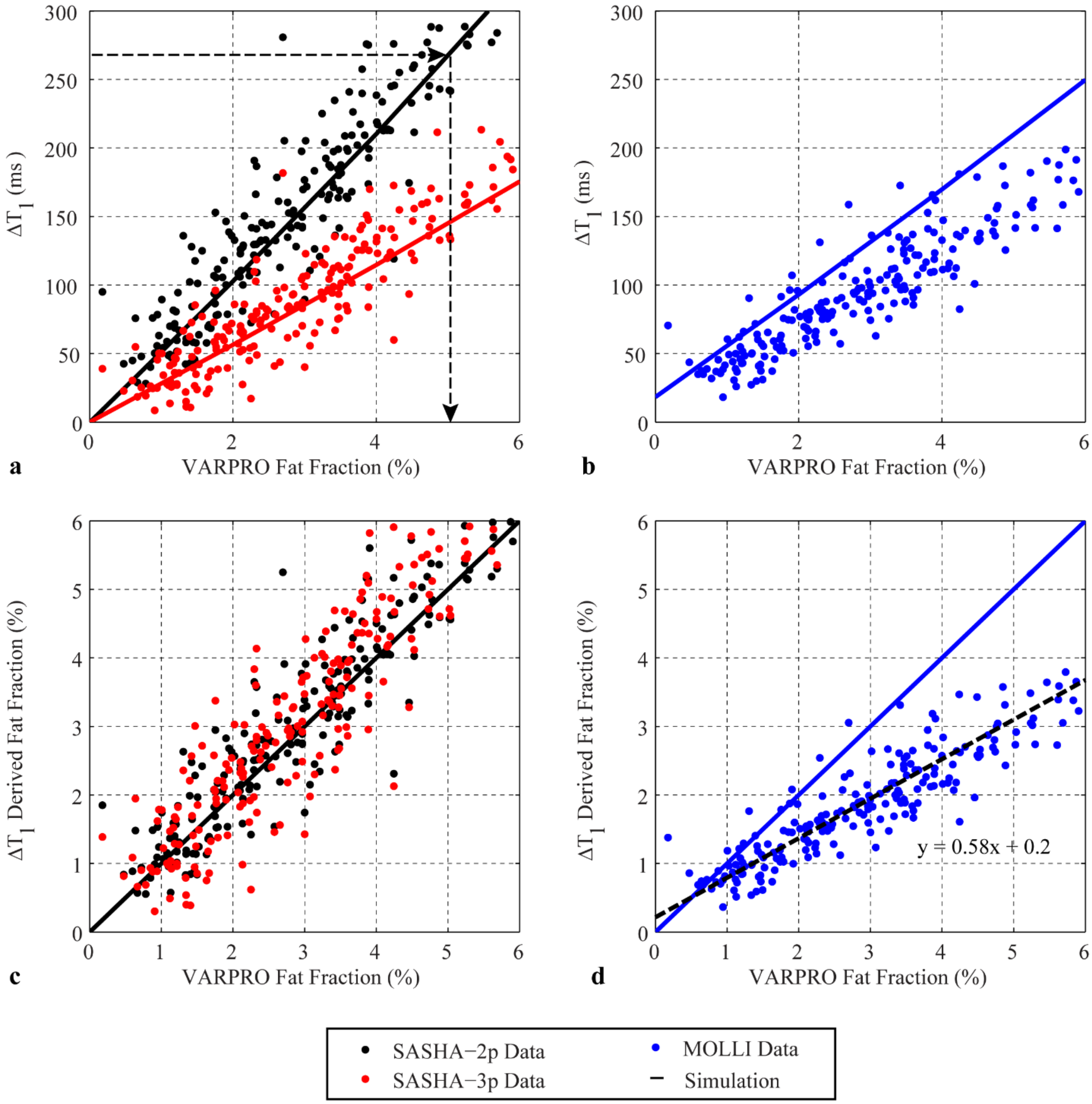

Figure 4.6. ΔT_1, and ΔT_1 derived fat fraction vs VARPRO. In-vivo skeletal muscle SASHA and MOLLI ΔT_1 values (between -70 and +30 Hz, as shown in Figure 4.5) vs. estimated fat fraction (VARPRO) for all 10 healthy volunteers are shown in **(a)** and **(b)**. The solid lines correspond to the ΔT_1 values from numerical simulations, for given fat fractions. The corresponding predicted fat fraction in all skeletal muscle regions, based on the simulated relationship between ΔT_1 vs fat fraction, are shown in **(c)** and **(d)** (i.e. measured ΔT_1 values are converted to fat fractions based on simulated relationship between ΔT_1 and FF, as shown in Figure 4.6a).

maximum TS times (Figure 4.8e). SASHA-2p fitting with single TS times of 350 and 600 ms (9 repetitions at a single TS plus one non-saturation image), shown in Figure 4.8f, have similar variability in FF as compared to the range of TS times (Figure 4.8d), with a standard deviation of ~0.25% for an SNR of 150 to 1 in the non-saturation image, with slightly improved performance with lower TS times.

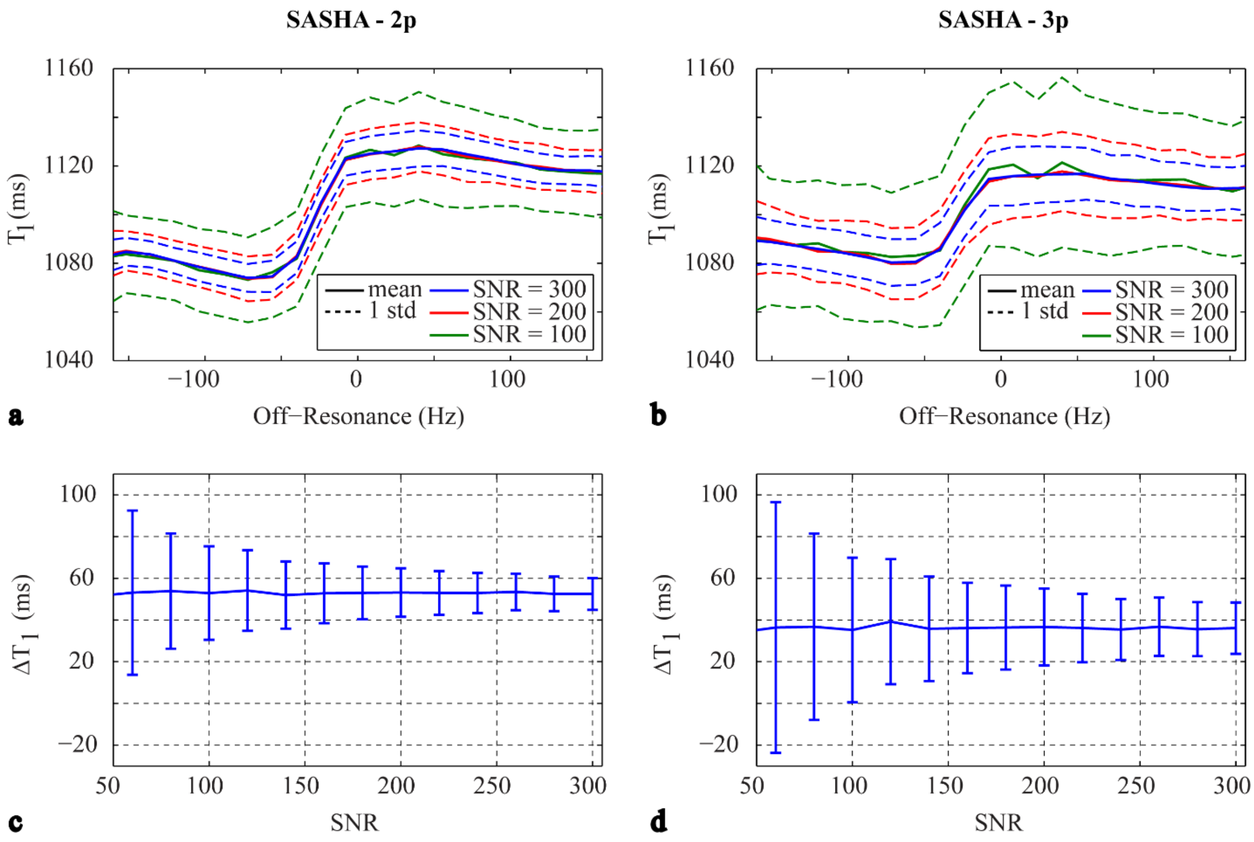

Figure 4.7. Monte Carlo simulations of T_1 vs off-resonance frequency. Results are shown for signal to noise ratios (SNR) = [100 200 300] for SASHA-2p **(a)** and SASHA-3p **(b)** methods. The resulting ΔT_1 values (mean ± std) vs SNR for SASHA-2p and SASHA-3p are shown in **(c)** and **(d)**. All plots are for 1% fat fraction and a sampling scheme identical to that used in phantom and in-vivo studies.

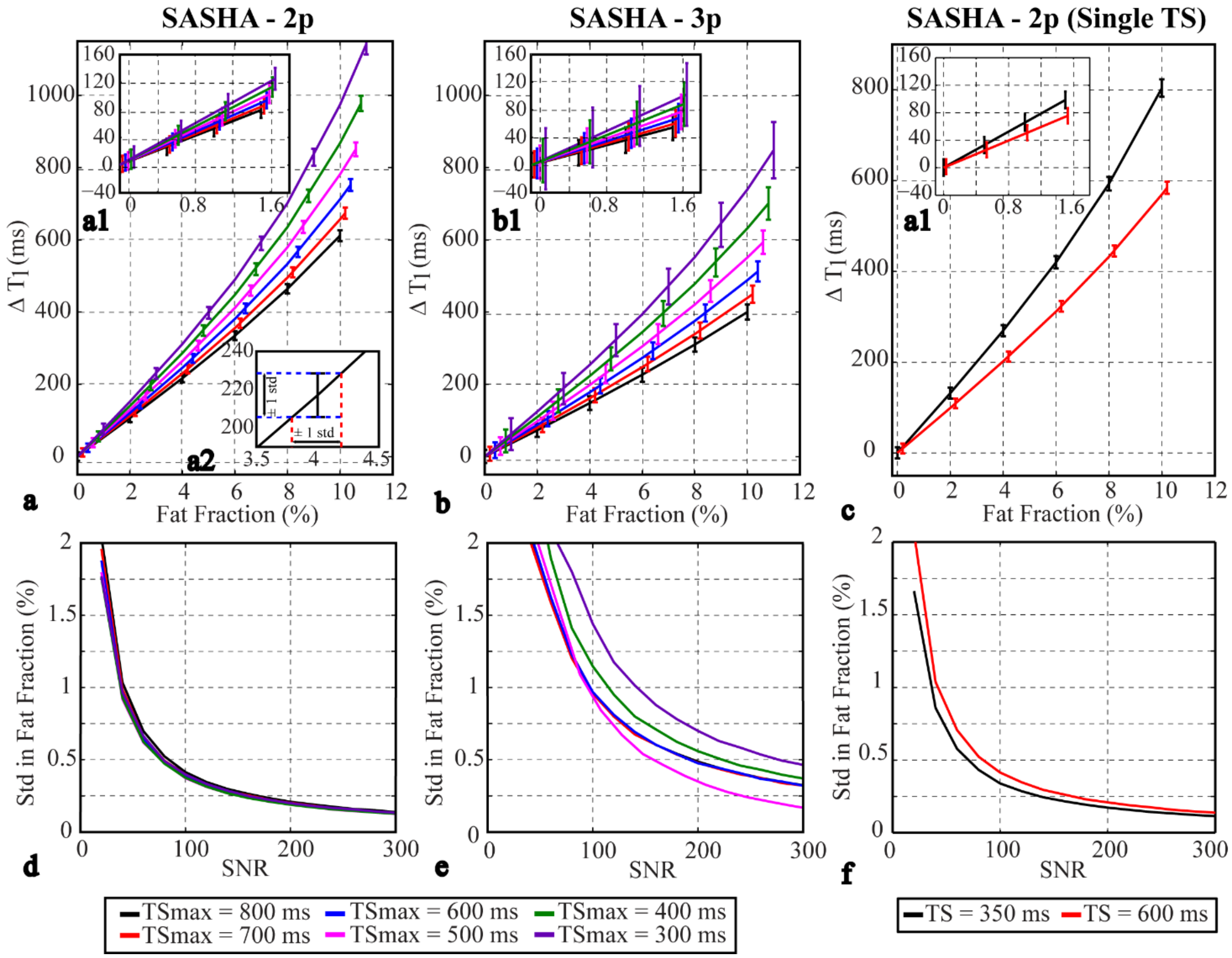

Figure 4.8. ΔT_1 fat fraction variability as a function of SNR. Dependence of the relationship between ΔT_1 and fat fraction for SASHA-2p **(a)** and SASHA-3p (**b**) as function of the maximum TS time (300:100:800 ms) and SASHA-2p with a single TS time (**c**) with error bars for an SNR of 200 to 1. ΔT_1 is defined as the difference between the T_1 at +30Hz and -70Hz. Insets **a-1** and **b-1** zoom in on low fat concentrations. Error bars have been shifted relative to the TS_{max}=800 ms case to improve readability. Inset **a-2** demonstrates how ±1std in ΔT_1 is translated to ±1std in fat percentage (std = standard deviation). The std in fat fraction as a function of SNR is shown for SASHA-2p **(d)** and SASHA-3p **(e)**, for TSmax = 300 ms to 800 ms and for SASHA-2p with single TS times of 350 ms and 600 ms **(f)**.

4.5.4 Accuracy of Fat-Fraction Imaging with T1 Mapping

Figure 4.9a-c illustrates the dependence of ΔT_1, for the case of 1% FF, on the fat T_1, the water T_1, and the error in off-resonance frequency, respectively, for the single TS SASHA-2p method. The corresponding error in FF is shown in Figure 4.9d-f, where the assumed true water and fat

T_1 values are 1100 ms and 250 ms, respectively. As expected, ΔT_1 is reduced with error in off-resonance frequency because the peak minimum and maximum T_1 offsets will not be captured, which results in an underestimation of FF. Figure 4.9g-i shows similar plots to d-f, for increasing FF up to 10% and a TS of 350 ms.

Phantom validation of the proposed FF imaging method is summarized in Figure 4.4b. ΔT_1 predicted FF in all phantoms, for SASHA and MOLLI methods are compared to VARPRO and ^{1}H spectroscopy measurements. Data was corrected for off-resonance prior to extraction of data at -70 and +30 using the off-resonance value to shift the frequency axis. For the SASHA data, the water T_1 for the ΔT_1 derived FF method was estimated as the mean of the two T_1 values used to calculate ΔT_1. The VARPRO data significantly overestimated FF at the lowest (~0.1%) FF as compared to spectroscopy, but with good general agreement for higher FF. The SASHA-2p derived FF had 0.22% or less absolute difference from spectroscopy FF for the 0 to 6% FF phantoms, with similar values for SASHA-3p, but with a systematic FF overestimation for MOLLI (similar to in-vivo results in Figure 4.6).

The relationship between the FF derived from the SASHA and MOLLI data as compared to VARPRO for in-vivo calf muscle experiments from the 10 healthy controls is shown in Figure 4.6c and d. All methods show a linear relationship to the VARPRO fat fractions, but he MOLLI

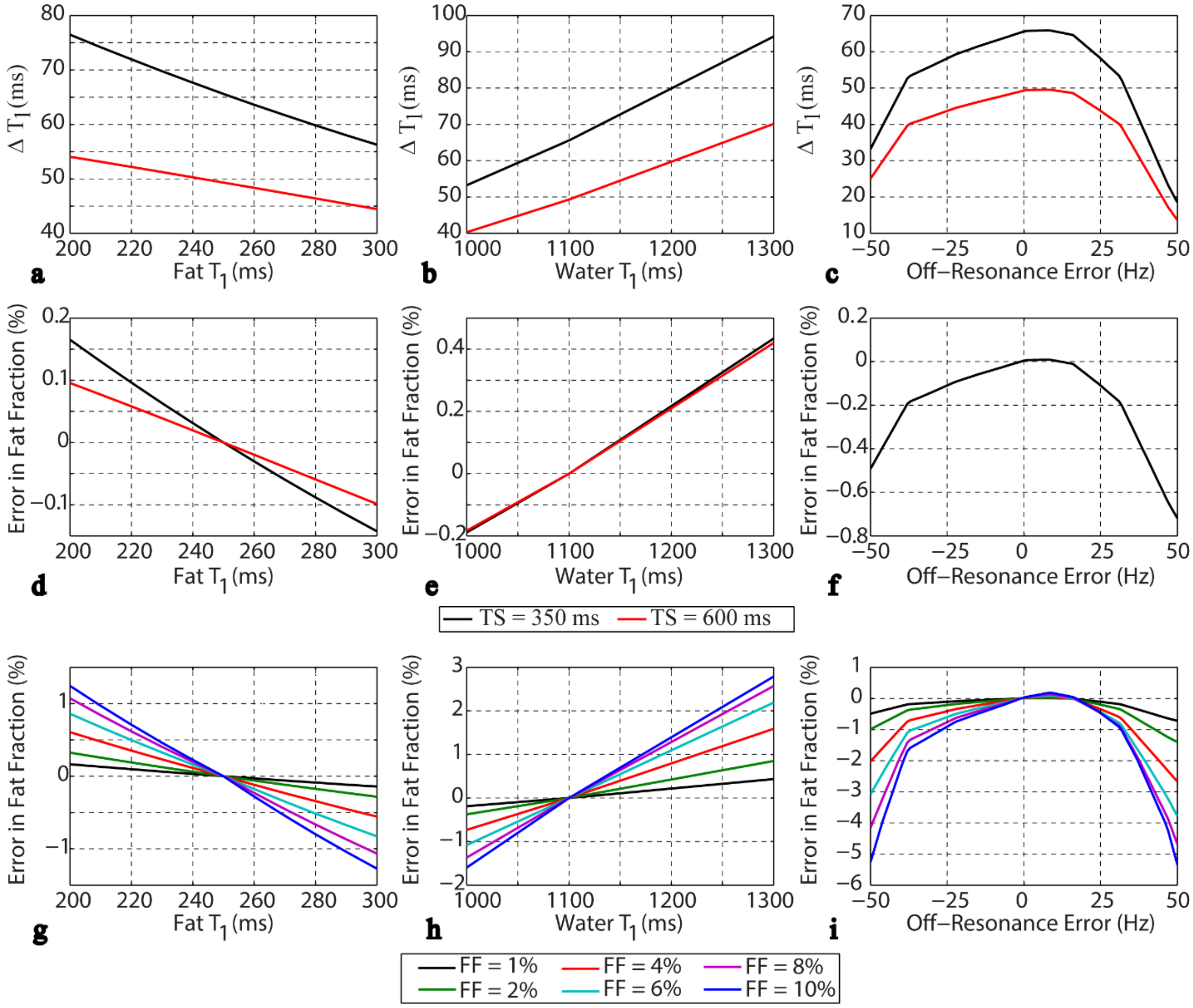

Figure 4.9. ΔT_1 error in fat fraction due to errors in fat T_1 water T_1 and B_0 inhomogeneity. Dependence of ΔT_1 on fat T_1 **(a)**, water T_1 **(b)** and off-resonance frequency offset from B_0 inhomogeneity **(c)** and the corresponding error in predicted fat fraction based on a true water T_1 of 1100 ms and fat T_1 of 250 ms for 1% fat fraction and SASHA-2p single TS times of 350 ms and 600 ms in **(d-f),** and for 1-10% fat fractions and a SASHA-2p single TS time of 350 ms in **(g-i)**.

data shows a systematic overestimation of FF, as a result of underestimation of T_1 as compared to predicted values (Figure 4.6b). Figure 4.10 compares FF pixel maps from three representative subjects, derived from ΔT_1 maps using the SASHA-2p method, to the corresponding VARPRO FF pixel maps. FF (mean±std) from sample regions from the tibialis anterior are shown for each subject. SNR values in the non- saturation recovery images were greater than 120 to 1 in all subjects.

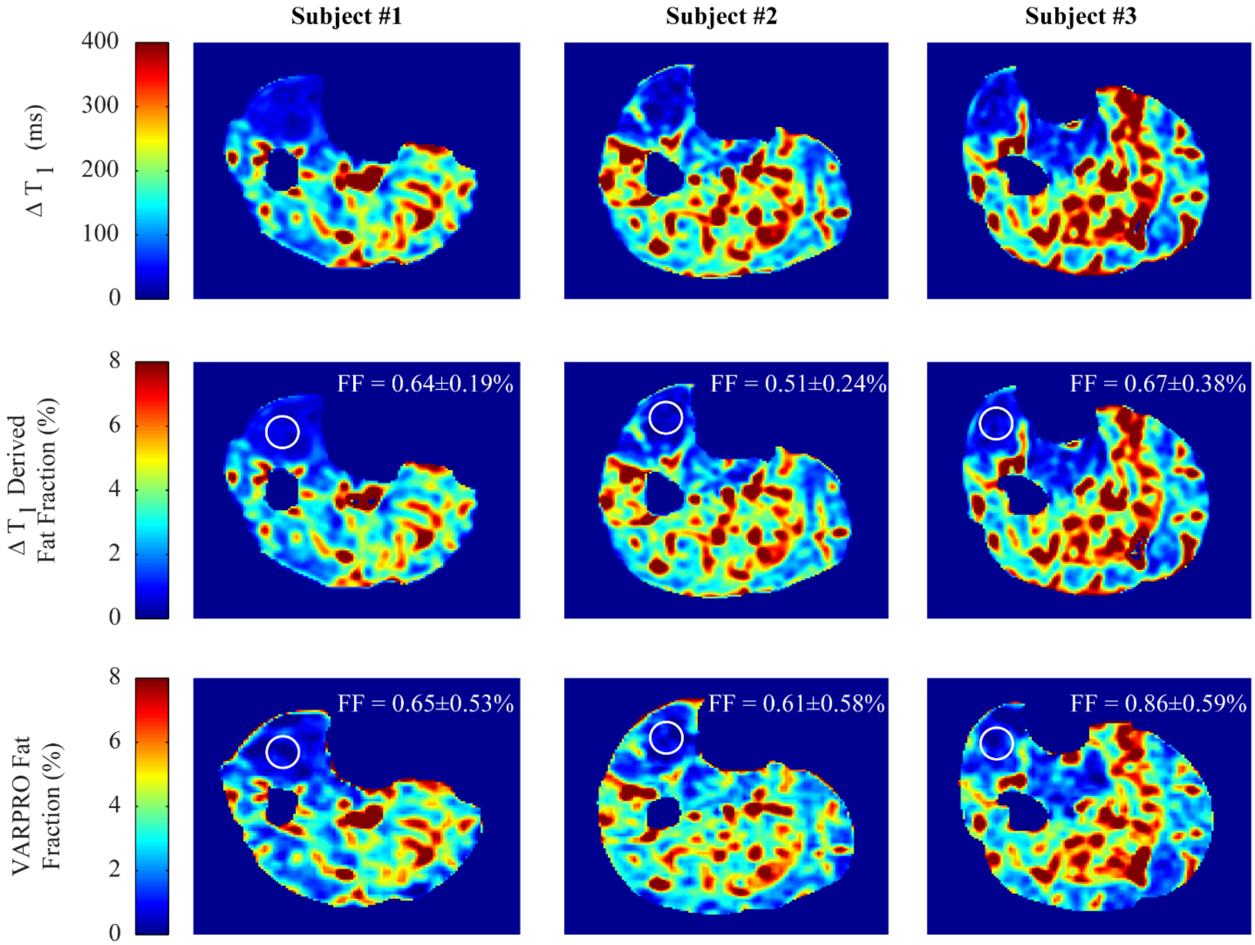

Figure 4.10. ΔT_1 and derived fat fraction pixel maps vs VARPRO. Sample pixel maps of ΔT_1 and derived fat fraction in three healthy controls (SASHA-2p), with comparison to pixel maps derived using VARPRO. ΔT_1 derived fat fraction (FF) and VARPRO FF values (mean±std) are reported for the regions of interest shown in the tibialis anterior.

4.6 Discussion

In response to relatively low fat concentrations (0-10% FF), both SASHA and MOLLI T_1 mapping pulse sequences were shown to yield significantly increased or decreased T_1 values with a characteristic sigmoidal pattern of T_1 offset as a function of off-resonance frequency, in agreement with previous studies (56,57).

The origin of the sigmoidal pattern was shown to be due to the relative offset of the water and fat frequency response to the b-SSFP pulse sequence, giving rise to in-phase and out-of-phase interference between water and fat, which corresponded to reduced and increased best-fit T_1 values, respectively. From this T_1 frequency dependence, a new approach to estimate FF, based on the total difference between the positive and negative T_1 shifts (ΔT_1), was described and validated with simulations, phantoms and in-vivo experiments. Relatively large ΔT_1 values of ~65 ms were shown for the SASHA-2p method for FF values of ~1%.

4.6.1 SASHA and MOLLI T_1 Frequency Dependence

The frequency pattern of the T_1 offset depends on both the b-SSFP TR and the chemical shift difference between water and the predominant fat peak, according to $f_{\text{cross-over}} = (0.5 \cdot \text{TR}^{-1} - 42.576\ \text{MHz}\ \text{T}^{-1} \cdot 3.3\ \text{ppm} \cdot B_0)$, which was -26 Hz for the commonly used TR = 2.7 ms, for 1.5T. Thus, either increased or decreased native T_1 values can potentially be ascribed to fat, depending on off-resonance frequency in conjunction with TR, which can confound underlying increased water T_1 values that would normally be ascribed to fibrosis or edema. At 3T, $f_{\text{cross-over}}$ = -236 Hz for TR = 2.7 ms, with fat and water out of phase for most off-resonance frequencies, resulting in increased T_1 values with increasing fat content for SASHA and MOLLI pulse sequences. As shown in the equation above, $f_{\text{cross-over}}$ can be adjusted to a targeted frequency by adjusting TR.

4.6.2 Relationship between ΔT_1 and FF

The magnitude of the T_1 offset was shown to be approximately linear with FF (0 - 10%) for all three T_1-mapping methods considered, with the slopes (ΔT_1 in ms /% fat) varying as a function of method and specific pulse sequence parameters, as confirmed with Bloch equation simulations, phantom and in-vivo experiments. For the SASHA method, ΔT_1 was shown to depend on the TS sampling times, the use of two or three-parameter fitting, the water and fat T_1 values and the off-resonance frequency. Fortunately, these factors can be either set by the user (two versus three-parameter fitting, TS times), measured (off-resonance frequency, water T_1) or held constant for all studies (fat T_1). In particular, water T_1 can be estimated as the mean value of the increased and decreased T_1 values used to calculated ΔT_1. Fat T_1 values would not be expected to vary considerably between subjects, so should be set to a constant value for all studies (250 ms in the current study). Thus, it is possible to use a single slope relating ΔT_1 and FF to estimate FF from T_1 imaging. The SASHA-2p approach with a single repeated TS time was shown to be the most sensitive to FF and with the optimal SNR performance (50% reduction in FF variability as compared to SASHA-3p). SASHA also has the advantage of negligible sensitivity to off-resonance frequency over a wide range of frequencies (46) (confirmed with simulations and phantom data in Figure 4.3).

MOLLI data showed a similar linear relationship between ΔT_1 and FF, however with a systematic offset from predicted values (in Figure 4.6b and d). These offsets are likely the result of the underlying dependence of MOLLI T_1 and ΔT_1 values on off-resonance frequency, T_2, and several pulse sequence parameters, including the specific pattern of multiple Look-Locker sets. Full characterization of these dependencies were the beyond the scope of this study.

Phantom data shown in Figure 4.4b showed that for FF less than 5%, the SASHA-2p ΔT_1 fat quantification agreed with spectroscopy data, particularly at very low FF (FF<1%), where the Dixon-based methods tend to overestimate FF. In the current study the VARPRO method of reconstruction of multi-echo data for fat-water separated imaging, a bias in FF of approximately 0.7% was observed for the water only phantom despite the high SNR and ideal single echo per acquisition protocol with a 6 min 40 s acquisition time. The source of bias at low FF is unknown but might arise due to regularization or model mismatch in the pre-calibrated spectrum. Noise bias due to magnitude detection was mitigated using method proposed by Liu (67) but may not have been completely effective. In terms of precision, the standard deviation of the derived FF values in homogeneous tissue regions (tibialis anterior, Figure 4.10) were shown to be ~0.2 to 0.4%, in general agreement with the predicated range of values, from Figure 4.8f.

4.6.3 Limitations

The current study has a number of limitations. The effects of an underlying inhomogeneous magnetic field on the quantification of ΔT_1 was not considered in detail, beyond the effects shown in Figure 4.9, which illustrated underestimation of ΔT_1 and FF with increasing off-resonance from B_0 inhomogeneity. In practice, an off-resonance map, potentially in combination with more than two SASHA-2p acquisitions (at more finely spaced off-resonance frequencies), could be used to address off-resonance effects (i.e. to capture the true peak ΔT_1 values and reduce variability). Another potential limitation is that of SNR and associated variability in FF. A smaller FF variability than the 0.25% derived for a relatively high SNR of 150 to 1 would be desirable to examine intracellular FF. Assumedly, this limitation could be addressed by including several pixels in larger regions of interest to assess low FF with this method, where higher SNR would be achieved with the associated signal averaging. Also, no in-vivo data from the heart was shown, and thus the viability of using the proposed method in the heart, including confounders such as motion and magnetic field inhomogeneity, has yet to be determined.

The MOLLI sequence was not thoroughly investigated and the variability and systematic errors in ΔT_1 and FF as compared to the optimal SASHA-2p method are unknown. MOLLI was not considered in more detail in the current study due to larger number of degrees of freedom in defining the MOLLI sequence, and it's more complex T_1 dependence (42) on factors such as flip angle (61) , heart rate (45,68), magnetization transfer (69) and off-resonance effects (65). Nonetheless, it was shown that MOLLI has the same underlying linear relationship between ΔT_1 and FF and has similar potential to SASHA to quantify FF based on measurement of ΔT_1. The findings of the current study apply only to sequences using a b-SSFP readout and thus are not applicable to the inversion-recovery or saturation-recovery gradient-echo T_1-mapping methods.

4.7 Conclusions

Relatively low fat concentrations result in clinically relevant negative or positive shifts in tissue T_1 over a narrow range of off-resonance frequencies with MOLLI and SASHA using standard 1.5T protocols. The difference between positive and negative T_1 shits, ΔT_1, are linearly related to FF for low values, with ΔT_1 values of 65 ms for the SASHA-2p method at FF values of ~1%. An optimized SASHA-2p approach yielded an underlying variability in FF of ~0.25% for a SNR of 150 to 1 in the non-saturation image.

4.8 Chapter 4 References

1. Ferreira VM, Piechnik SK, Dall'Armellina E, Karamitsos TD, Francis JM, Choudhury RP, Friedrich MG, Robson MD, Neubauer S. Non-contrast T1-mapping detects acute myocardial edema with high diagnostic accuracy: a comparison to T2-weighted cardiovascular magnetic resonance. Journal of Cardiovascular Magnetic Resonance 2012;14(1):42-42.

2. Bull S, White SK, Piechnik SK, Flett AS, Ferreira VM, Loudon M, Francis JM, Karamitsos TD, Prendergast BD, Robson MD, Neubauer S, Moon JC, Myerson SG. Human non-contrast T1 values and correlation with histology in diffuse fibrosis. Heart 2013;99(13):932-937.

32. Hernando D, Haldar JP, Sutton BP, Ma J, Kellman P, Liang ZP. Joint estimation of water/fat images and field inhomogeneity map. Magnetic Resonance in Medicine 2008;59(3):571-580.

42. Kellman P, Hansen MS. T1-mapping in the heart: accuracy and precision. Journal of Cardiovascular Magnetic Resonance 2014;16(1):2-22.

45. Messroghli DR, Radjenovic A, Kozerke S, Higgins DM, Sivananthan MU, Ridgway JP. Modified Look-Locker inversion recovery (MOLLI) for high-resolution T1 mapping of the heart. Magnetic Resonance in Medicine 2004;52(1):141-146.

46. Chow K, Flewitt JA, Green JD, Pagano JJ, Friedrich MG, Thompson RB. Saturation recovery single-shot acquisition (SASHA) for myocardial T1 mapping. Magnetic Resonance in Medicine 2014;71(6):2082-2095.

49. Chow K, Spottiswoode BS, Pagano JJ, Thompson RB. Improved precision in SASHA T1 mapping with a variable flip angle readout. Journal of Cardiovascular Magnetic Resonance 2014;16(Suppl 1):M9.

51. Miller KL. Asymmetries of the balanced SSFP profile. Part I: theory and observation. Magnetic Resonance in Medicine 2010;63(2):385-395.

52. Yu H, Shimakawa A, McKenzie CA, Brodsky E, Brittain JH, Reeder SB. Multiecho water-fat separation and simultaneous R2* estimation with multifrequency fat spectrum modeling. Magnetic Resonance in Medicine 2008;60(5):1122-1134.

53. Chow K, Kellman P, Spottiswoode BS, Nielles-Vallespin S, Thompson RB. Optimized saturation pulse trains for SASHA T(1) mapping at 3T. Journal of Cardiovascular Magnetic Resonance 2015;17(1):W20.

54. Kraft KA, Fatouros PP, Clarke GD, Kishore PRS. An MRI phantom material for quantitative relaxometry. Magnetic Resonance in Medicine 1987;5(6):555-562.

55. Machann J, Bachmann OP, Brechtel K, Dahl DB, Wietek B, Klumpp B, Haring HU, Claussen CD, Jacob S, Schick F. Lipid content in the musculature of the lower leg

assessed by fat selective MRI: intra- and interindividual differences and correlation with anthropometric and metabolic data. Journal of magnetic resonance imaging : JMRI 2003;17(3):350-357.

56. Thiesson SB, Thompson RB, Chow K. Characterization of T(1) bias from lipids in MOLLI and SASHA pulse sequences. Journal of Cardiovascular Magnetic Resonance 2015;17(1):W10.

57. Kellman P, Bandettini WP, Mancini C, Hammer-Hansen S, Hansen MS, Arai AE. Characterization of myocardial T1-mapping bias caused by intramyocardial fat in inversion recovery and saturation recovery techniques. J Cardiovasc Magn Reson 2015;17(1):33.

58. Carr H. Steady-State Free Precession in Nuclear Magnetic Resonance. Physical Review 1958;112(5):1693-1701.

59. Thompson R, Aviles R, Faranesh A, Raman V, Wright V, Balaban R, McVeigh E, Lederman R. Measurement of skeletal muscle perfusion during postischemic reactive hyperemia using contrast-enhanced MRI with a step-input function. Magnetic Resonance in Medicine 2005;54(2):289-298.

60. Hatakenaka M, Ueda M, Ishigami K, Otsuka M, Masuda K. Effects of aging on muscle T2 relaxation time: difference between fast- and slow-twitch muscles. Invest Radiol 2001;36(12):692-698.

61. Kellman P, Herzka DA, Hansen MS. Adiabatic inversion pulses for myocardial T1 mapping. Magnetic Resonance in Medicine 2014;71(4):1428-1434.

62. Deichmann R, Haase A. Quantification of T1 values by SNAPSHOT-FLASH NMR imaging. Journal of Magnetic Resonance (1969) 1992;96(3):608-612.

63. Marquardt DW. An Algorithm for Least-Squares Estimation of Nonlinear Parameters. Journal of the Society for Industrial and Applied Mathematics 1963;11(2):431-441.

64. Kellman P, Xue H, Chow K, Spottiswoode BS, Arai AE, Thompson RB. Optimized saturation recovery protocols for T1-mapping in the heart: influence of sampling strategies on precision. Journal of Cardiovascular Magnetic Resonance 2014;16(1):55.

65. Kellman P, Herzka DA, Arai AE, Hansen MS. Influence of Off-resonance in myocardial T1-mapping using SSFP based MOLLI method. J Cardiovasc Magn Reson 2013;15:63.

66. Kellman P. Influence of Off-resonance in myocardial T1-mapping using SSFP based MOLLI method. Journal of Cardiovascular Magnetic Resonance 2013;22(15).

67. Liu CY, McKenzie CA, Yu H, Brittain JH, Reeder SB. Fat quantification with IDEAL gradient echo imaging: correction of bias from T(1) and noise. Magn Reson Med 2007;58(2):354-364.

68. Messroghli DR, Greiser A, Fröhlich M, Dietz R, Schulz-Menger J. Optimization and validation of a fully-integrated pulse sequence for modified look-locker inversion-recovery (MOLLI) T1 mapping of the heart. Journal of Magnetic Resonance Imaging 2007;26(4):1081-1086.

69. Robson MD, Piechnik SK, Tunnicliffe EM, Neubauer S. T1 measurements in the human myocardium: The effects of magnetization transfer on the SASHA and MOLLI sequences. Magnetic Resonance in Medicine 2013;70(3):664-670.

Chapter 5. Conclusion

5.1 Summary

The present work validated a new method for FF quantification using a Phase Sweep b-SSFP sequence which also provided simultaneous T_1 and T_2 imaging. A related method characterized systematic errors in the conventional T_1 mapping methods MOLLI and SASHA as a result of low FF, and validated a method for fat quantification based on the modulation of T_1 values by the fat pool.

5.1.1 Simultaneous Quantification of Fat Fraction, Water T_1 and T_2, and Off-Resonance Frequency Using Phase Sweep b-SSFP

A custom single-shot saturation recovery Phase Sweep b-SSFP pulse sequence has been developed. The sequence exploits the chemical shift between fat and water to create constructive and destructive interference between fat and water signals across the phase sweep signal profile.

The resulting asymmetric profile is the consequence of the summation of the weighted signal profiles of water, S_w, and fat, S_f, where each signal profile is a function of T_1, T_2 and off-resonance. The profile can be decomposed into its elementary contributing components by fitting the acquired signal profile with a weighted water and fat signal profile from predefined basis sets spanning a wide range of T_1 and T_2 values. In this way the proposed Phase Sweep b-SSFP method is able to uniquely quantify FF, T_1, T_2, and off-resonance.

5.1.2 Characterization of T_1 Bias from Fat in MOLLI and SASHA Pulse Sequences: Quantitative Fat-Fraction Imaging with T_1 Mapping

The off-resonance behavior of the combined water and fat b-SSFP signal profile was shown to lead to a sigmoidal relationship between both MOLLI and SASHA T_1 values. Specifically, it was shown that relatively low FF resulted in clinically relevant negative or positive shifts in tissue T_1 (from the underlying water T_1) over a narrow range of off-resonance frequencies. Thus, increased or decreased native T_1 values can potentially be ascribed to fat, which can confound underlying increased water T_1 values ascribed to fibrosis or edema and complicate the use of T_1 mapping for indirect identification of fat via reduced T_1 values.

Based on this phenomenon, a new method has been proposed which uses SASHA T_1 measurements at a minimum of two off-resonance frequencies separated by ~100 Hz at 1.5T to quantify FF based on the measured ΔT_1 (the full range of T_1 values over the range of off-resonance frequencies). Specifically, ΔT_1 was shown to be linearly related to FF with the optimized SASHA T_1 mapping approach (with 2 parameter fitting), yielding an low underlying variability in FF of ~0.25% for a SNR of 150 to 1 in the non-saturation image (which is clinically achievable).

5.2 Future Directions

In its current form the Phase Sweep b-SSFP method provides simultaneous quantification of FF, water T_1, water T_2, and off-resonance frequency. However, achieving these results requires significant processing time on a standard desktop computer (4-6 hrs per calf slice). In order to become a clinically viable method this processing time must drastically reduced through the use of numerically optimized functions (outside of the MATLAB environment) or parallel computing. Further, the dictionary developed was specific to the values expected in the calf muscle of subjects. A dictionary encompassing T_1, and T_2 values commonly observed in the heart, kidney, and liver will need to be developed before the method can be tested in these organs. Underlying effects of an inhomogeneous B_1 magnetic field on the quantification of parameters in both methods should also be considered in further detail.

While both methods developed and validated in this thesis (Chapters 3 and 4) were designed to be compatible with free-breathing acquisitions, being based on rapid single-shot image acquisitions, this form of data acquisition has not been evaluated.

Both methods are applicable for use in any organ system where low FF quantification is required, particularly in those where cardiac or respiratory motion limits acquisition duration (all organs in the chest and abdominal cavity).

References for All Chapters

1. Ferreira VM, Piechnik SK, Dall'Armellina E, Karamitsos TD, Francis JM, Choudhury RP, Friedrich MG, Robson MD, Neubauer S. Non-contrast T1-mapping detects acute myocardial edema with high diagnostic accuracy: a comparison to T2-weighted cardiovascular magnetic resonance. Journal of Cardiovascular Magnetic Resonance 2012;14(1):42-42.

2. Bull S, White SK, Piechnik SK, Flett AS, Ferreira VM, Loudon M, Francis JM, Karamitsos TD, Prendergast BD, Robson MD, Neubauer S, Moon JC, Myerson SG. Human non-contrast T1 values and correlation with histology in diffuse fibrosis. Heart 2013;99(13):932-937.

3. Zia MI, Ghugre NR, Connelly KA, Strauss BH, Sparkes JD, Dick AJ, Wright GA. Characterizing Myocardial Edema and Hemorrhage Using Quantitative T2 and T2* Mapping at Multiple Time Intervals Post ST-Segment Elevation Myocardial Infarction. Circulation: Cardiovascular Imaging 2012;5(5):566-572.

4. Goodpaster BH, Wolf D. Skeletal muscle lipid accumulation in obesity, insulin resistance, and type 2 diabetes. Pediatric Diabetes 2004;5(4):219-226.

5. Burke AP, Farb A, Tashko G, Virmani R. Arrhythmogenic Right Ventricular Cardiomyopathy and Fatty Replacement of the Right Ventricular Myocardium: Are They Different Diseases? Circulation 1998;97(16):1571-1580.

6. Foster MC, Hwang SJ, Porter SA, Massaro JM, Hoffmann U, Fox CS. Fatty kidney, hypertension, and chronic kidney disease: the Framingham Heart Study. Hypertension 2011;58(5):784-790.

7. Calculli L, Festi D, Pezzilli R. Enlarged pancreas: not always a cancer. Hepatobiliary & pancreatic diseases international : HBPD INT 2015;14(1):107-108.

8. Farrell GC, Larter CZ. Nonalcoholic fatty liver disease: From steatosis to cirrhosis. Hepatology 2006;43(S1):S99-S112.

9. Bray GA. Handbook of Obesity --: Epidemiology, Etiology, and Physiopathology, Third Edition: Taylor & Francis; 2014.

10. Hu HH, Kan HE. Quantitative proton MR techniques for measuring fat. NMR in biomedicine 2013;26(12):1609-1629.

11. Gillies AR, Lieber RL. Structure and function of the skeletal muscle extracellular matrix. Muscle & nerve 2011;44(3):318-331.

12. Boesch C, Slotboom J, Hoppeler H, Kreis R. In vivo determination of intra-myocellular lipids in human muscle by means of localized 1H-MR-spectroscopy. Magnetic Resonance in Medicine 1997;37(4):484-493.

13. Leroy-Willig A, Willig TN, Henry-Feugeas MC, Frouin V, Marinier E, Boulier A, Barzic F, Schouman-Claeys E, Syrota A. Body composition determined with MR in patients with Duchenne muscular dystrophy, spinal muscular atrophy, and normal subjects. Magnetic resonance imaging 1997;15(7):737-744.

14. Visser M, Goodpaster BH, Kritchevsky SB, Newman AB, Nevitt M, Rubin SM, Simonsick EM, Harris TB, Study ftHA. Muscle Mass, Muscle Strength, and Muscle Fat Infiltration as Predictors of Incident Mobility Limitations in Well-Functioning Older Persons. The Journals of Gerontology Series A: Biological Sciences and Medical Sciences 2005;60(3):324-333.

15. Goutallier D, Postel JM, Bernageau J, Lavau L, Voisin MC. Fatty muscle degeneration in cuff ruptures. Pre- and postoperative evaluation by CT scan. Clinical orthopaedics and related research 1994(304):78-83.

16. Nakagaki K, Ozaki J, Tomita Y, Tamai S. Fatty degeneration in the supraspinatus muscle after rotator cuff tear. Journal of shoulder and elbow surgery / American Shoulder and Elbow Surgeons [et al] 1996;5(3):194-200.

17. Samara A, Ventura EE, Alfadda AA, Goran MI. Use of MRI and CT for fat imaging in children and youth: what have we learned about obesity, fat distribution and metabolic disease risk? Obesity reviews : an official journal of the International Association for the Study of Obesity 2012;13(8):723-732.

18. Katherine M Flegal MDC, Cynthia L. Ogden, Lester R. Curtin. Prevalence and Trends in Obesity Among US Adults, 1999-2008. Journal of American Medical Association (JAMA) 2010;303(3):235-241.

19. Ogden CL, Carroll MD, Kit BK, Flegal KM. Prevalence of obesity and trends in body mass index among US children and adolescents, 1999-2010. Jama 2012;307(5):483-490.

20. Rutger W. van der Meer HJL, Johannes W.A. Simit, Albert de Roos. MR Imaging Evaluation of Cadiovascular Risk in Metabolic Syndrome. Radiology 2012;264(1).

21. Wattjes MP, Kley RA, Fischer D. Neuromuscular imaging in inherited muscle diseases. European radiology 2010;20(10):2447-2460.

22. Reeder SB, Cruite I, Hamilton G, Sirlin CB. Quantitative assessment of liver fat with magnetic resonance imaging and spectroscopy. Journal of magnetic resonance imaging : JMRI 2011;34(4):729-749.

23. Sado DM, White SK, Piechnik SK, Banypersad SM, Treibel T, Captur G, Fontana M, Maestrini V, Flett AS, Robson MD, Lachmann RH, Murphy E, Mehta A, Hughes D, Neubauer S, Elliott PM, Moon JC. Identification and assessment of Anderson-Fabry disease by cardiovascular magnetic resonance noncontrast myocardial T1 mapping. Circulation Cardiovascular imaging 2013;6(3):392-398.

24. Thompson RB, Chow K, Khan A, Chan A, Shanks M, Paterson I, Oudit GY. T(1) mapping with cardiovascular MRI is highly sensitive for Fabry disease independent of hypertrophy and sex. Circulation Cardiovascular imaging 2013;6(5):637-645.

25. Bloembergen N, Purcell EM, Pound RV. Relaxation Effects in Nuclear Magnetic Resonance Absorption. Physical Review 1948;73(7):679-712.

26. Hamilton G, Yokoo T, Bydder M, Cruite I, Schroeder ME, Sirlin CB, Middleton MS. In vivo characterization of the liver fat 1H MR spectrum. NMR in biomedicine 2011;24(7):784-790.

27. Bley TA, Wieben O, Francois CJ, Brittain JH, Reeder SB. Fat and water magnetic resonance imaging. Journal of magnetic resonance imaging : JMRI 2010;31(1):4-18.

28. Dixon WT. Simple proton spectroscopic imaging. Radiology 1984;153(1):189-194.

29. Glover GH, Schneider E. Three-point dixon technique for true water/fat decomposition with B0 inhomogeneity correction. Magnetic Resonance in Medicine 1991;18(2):371-383.

30. Szumowski J, Coshow WR, Li F, Quinn SF. Phase unwrapping in the three-point Dixon method for fat suppression MR imaging. Radiology 1994;192(2):555-561.

31. Kellman P, Hernando D, Shah S, Zuehlsdorff S, Jerecic R, Mancini C, Liang Z-P, Arai AE. Multi-echo Dixon Fat and Water Separation Method for Detecting Fibro-fatty Infiltration in the Myocardium. Magnetic Resonance in Medicine 2009;61(1):215-221.

32. Hernando D, Haldar JP, Sutton BP, Ma J, Kellman P, Liang ZP. Joint estimation of water/fat images and field inhomogeneity map. Magnetic Resonance in Medicine 2008;59(3):571-580.

33. JC Seidell CB, K van der Kooy. Imaging techniques for measuring adipose-tissue distribution-a comparison between computed tomography and 1.5-T magnetic resonance. . Am J Clin Nutr 1990;51:953-957.

34. Machann J, Thamer C, Schnoedt B, Haap M, Haring HU, Claussen CD, Stumvoll M, Fritsche A, Schick F. Standardized assessment of whole body adipose tissue topography by MRI. Journal of magnetic resonance imaging : JMRI 2005;21(4):455-462.

35. Mercuri E, Pichiecchio A, Allsop J, Messina S, Pane M, Muntoni F. Muscle MRI in inherited neuromuscular disorders: past, present, and future. Journal of magnetic resonance imaging : JMRI 2007;25(2):433-440.

36. Shen W, Chen J, Gantz M, Punyanitya M, Heymsfield SB, Gallagher D, Albu J, Engelson E, Kotler D, Pi-Sunyer X, Gilsanz V. MRI-measured pelvic bone marrow adipose tissue is inversely related to DXA-measured bone mineral in younger and older adults. European journal of clinical nutrition 2012;66(9):983-988.

37. Goldfarb JW, Arnold-Anteraper S. Water-fat separation imaging of the heart with standard magnetic resonance bSSFP CINE imaging. Magnetic Resonance in Medicine 2014;71(6):2096-2104.

38. Aquaro GD, Todiere G, Strata E, Barison A, Di Bella G, Lombardi M. Usefulness of India ink artifact in steady-state free precession pulse sequences for detection and quantification of intramyocardial fat. Journal of magnetic resonance imaging : JMRI 2014;40(1):126-132.

39. Hargreaves BA, Vasanawala SS, Nayak KS, Hu BS, Nishimura DG. Fat-suppressed steady-state free precession imaging using phase detection. Magnetic Resonance in Medicine 2003;50(1):210-213.

40. Kellman P, Bandettini WP, Mancini C, Hammer-Hansen S, Hansen MS, Arai AE. Characterization of myocardial T1-mapping bias caused by intramyocardial fat in inversion recovery and saturation recovery techniques. Journal of Cardiovascular Magnetic Resonance 2015;17(1):33.

41. Wood JC, Otto-Duessel M, Aguilar M, Nick H, Nelson MD, Coates TD, Pollack H, Moats R. Cardiac Iron Determines Cardiac T2*, T2, and T1 in the Gerbil Model of Iron Cardiomyopathy. Circulation 2005;112(4):535-543.

42. Kellman P, Hansen MS. T1-mapping in the heart: accuracy and precision. Journal of Cardiovascular Magnetic Resonance 2014;16(1):2-22.

43. Pennell DJ, Sechtem UP, Higgins CB, Manning WJ, Pohost GM, Rademakers FE, van Rossum AC, Shaw LJ, Yucel EK. Clinical indications for cardiovascular magnetic resonance (CMR): Consensus Panel report. European heart journal 2004;25(21):1940-1965.

44. Hunold P, Schlosser T, Vogt FM, Eggebrecht H, Schmermund A, Bruder O, Schuler WO, Barkhausen J. Myocardial late enhancement in contrast-enhanced cardiac MRI: distinction between infarction scar and non-infarction-related disease. AJR American journal of roentgenology 2005;184(5):1420-1426.

45. Messroghli DR, Radjenovic A, Kozerke S, Higgins DM, Sivananthan MU, Ridgway JP. Modified Look-Locker inversion recovery (MOLLI) for high-resolution T1 mapping of the heart. Magnetic Resonance in Medicine 2004;52(1):141-146.

46. Chow K, Flewitt JA, Green JD, Pagano JJ, Friedrich MG, Thompson RB. Saturation recovery single-shot acquisition (SASHA) for myocardial T1 mapping. Magnetic Resonance in Medicine 2014;71(6):2082-2095.

47. Piechnik SK, Ferreira VM, Dall'Armellina E, Cochlin LE, Greiser A, Neubauer S, Robson MD. Shortened Modified Look-Locker Inversion recovery (ShMOLLI) for clinical myocardial T1-mapping at 1.5 and 3 T within a 9 heartbeat breathhold. Journal of cardiovascular magnetic resonance : official journal of the Society for Cardiovascular Magnetic Resonance 2010;12:69.

48. Schelbert EB, Testa SM, Meier CG, Ceyrolles WJ, Levenson JE, Blair AJ, Kellman P, Jones BL, Ludwig DR, Schwartzman D, Shroff SG, Wong TC. Myocardial extravascular extracellular volume fraction measurement by gadolinium cardiovascular magnetic resonance in humans: slow infusion versus bolus. Journal of cardiovascular magnetic resonance : official journal of the Society for Cardiovascular Magnetic Resonance 2011;13:16.

49. Chow K, Spottiswoode BS, Pagano JJ, Thompson RB. Improved precision in SASHA T1 mapping with a variable flip angle readout. Journal of Cardiovascular Magnetic Resonance 2014;16(Suppl 1):M9.

50. Scheffler K, Lehnhardt S. Principles and applications of balanced SSFP techniques. European radiology 2003;13(11):2409-2418.

51. Miller KL. Asymmetries of the balanced SSFP profile. Part I: theory and observation. Magnetic Resonance in Medicine 2010;63(2):385-395.

52. Yu H, Shimakawa A, McKenzie CA, Brodsky E, Brittain JH, Reeder SB. Multiecho water-fat separation and simultaneous R2* estimation with multifrequency fat spectrum modeling. Magnetic Resonance in Medicine 2008;60(5):1122-1134.

53. Chow K, Kellman P, Spottiswoode BS, Nielles-Vallespin S, Thompson RB. Optimized saturation pulse trains for SASHA T(1) mapping at 3T. Journal of Cardiovascular Magnetic Resonance 2015;17(1):W20.

54. Kraft KA, Fatouros PP, Clarke GD, Kishore PRS. An MRI phantom material for quantitative relaxometry. Magnetic Resonance in Medicine 1987;5(6):555-562.

55. Machann J, Bachmann OP, Brechtel K, Dahl DB, Wietek B, Klumpp B, Haring HU, Claussen CD, Jacob S, Schick F. Lipid content in the musculature of the lower leg assessed by fat selective MRI: intra- and interindividual differences and correlation with anthropometric and metabolic data. Journal of magnetic resonance imaging : JMRI 2003;17(3):350-357.

56. Thiesson SB, Thompson RB, Chow K. Characterization of T(1) bias from lipids in MOLLI and SASHA pulse sequences. Journal of Cardiovascular Magnetic Resonance 2015;17(1):W10.

57. Kellman P, Bandettini WP, Mancini C, Hammer-Hansen S, Hansen MS, Arai AE. Characterization of myocardial T1-mapping bias caused by intramyocardial fat in inversion recovery and saturation recovery techniques. J Cardiovasc Magn Reson 2015;17(1):33.

58. Carr H. Steady-State Free Precession in Nuclear Magnetic Resonance. Physical Review 1958;112(5):1693-1701.

59. Thompson R, Aviles R, Faranesh A, Raman V, Wright V, Balaban R, McVeigh E, Lederman R. Measurement of skeletal muscle perfusion during postischemic reactive

hyperemia using contrast-enhanced MRI with a step-input function. Magnetic Resonance in Medicine 2005;54(2):289-298.

60. Hatakenaka M, Ueda M, Ishigami K, Otsuka M, Masuda K. Effects of aging on muscle T2 relaxation time: difference between fast- and slow-twitch muscles. Invest Radiol 2001;36(12):692-698.

61. Kellman P, Herzka DA, Hansen MS. Adiabatic inversion pulses for myocardial T1 mapping. Magnetic Resonance in Medicine 2014;71(4):1428-1434.

62. Deichmann R, Haase A. Quantification of T1 values by SNAPSHOT-FLASH NMR imaging. Journal of Magnetic Resonance (1969) 1992;96(3):608-612.

63. Marquardt DW. An Algorithm for Least-Squares Estimation of Nonlinear Parameters. Journal of the Society for Industrial and Applied Mathematics 1963;11(2):431-441.

64. Kellman P, Xue H, Chow K, Spottiswoode BS, Arai AE, Thompson RB. Optimized saturation recovery protocols for T1-mapping in the heart: influence of sampling strategies on precision. Journal of Cardiovascular Magnetic Resonance 2014;16(1):55.

65. Kellman P, Herzka DA, Arai AE, Hansen MS. Influence of Off-resonance in myocardial T1-mapping using SSFP based MOLLI method. J Cardiovasc Magn Reson 2013;15:63.

66. Kellman P. Influence of Off-resonance in myocardial T1-mapping using SSFP based MOLLI method. Journal of Cardiovascular Magnetic Resonance 2013;22(15).

67. Liu CY, McKenzie CA, Yu H, Brittain JH, Reeder SB. Fat quantification with IDEAL gradient echo imaging: correction of bias from T(1) and noise. Magn Reson Med 2007;58(2):354-364.

68. Messroghli DR, Greiser A, Fröhlich M, Dietz R, Schulz-Menger J. Optimization and validation of a fully-integrated pulse sequence for modified look-locker inversion-recovery (MOLLI) T1 mapping of the heart. Journal of Magnetic Resonance Imaging 2007;26(4):1081-1086.

69. Robson MD, Piechnik SK, Tunnicliffe EM, Neubauer S. T1 measurements in the human myocardium: The effects of magnetization transfer on the SASHA and MOLLI sequences. Magnetic Resonance in Medicine 2013;70(3):664-670.

Appendix A.

Purpose:

- To construct 6 fat-agarose phantoms for evaluation with MRI and MRS with fat concentrations ranging from 0-9% fat.

Procedure and Materials:

- Dissolve 0.81g of $NiCl_2$ in 1L of distilled water to yield a 6.25 mM stock solution.
- Using a syringe and scale measure the appropriate mass of water (Table 1), $NiCl_2$ stock solution, hand soap, oil, and agarose into each 50ml plastic vial. Gently stir each vial after the addition of each soap, oil and agarose. Note that shaking or aggressive stirring may lead to the formation of undesirable air bubbles in the phantoms.
- After sealing each vial with a screw top lid place the phantoms in a room temperature water bath. Over the following 1 hr. increase the temperature of the water bath on a hot plate. Stir each vial periodically throughout the heating process (5x over the hour).
- During the heating process the temperature of the water bath should remain below the boiling point of water but surpass the melting point of agarose (185^{o}F). If the agarose gets too hot it will form undesirable air bubbles.
- Once all phantoms appear homogeneous and fluid, decrease the temperature of the hot plate by half for 20min. Following these 20 min remove the water bath from the hotplate leaving the vials submerged to cool slowly.
- Using the amounts specified in table 1 will result in phantoms that are 1% soap, 2.5% agarose, and 0.001% $NiCl_{2.}$ Where all percentages are mass percentages.
- Hand soap is used to emulsify the peanut oil and water, while $NiCl_2$ is used to achieve T_1 and T_2 values that are representative of in-vivo values.

Table 1: Lipid Phantom Composition

Phantom (% Fat)	Distilled Water (g)	$NiCl_2$ Stock (ml)	Agarose (g)	Soap (g)	Peanut Oil (g)
0	21.13	3.00	0.62	0.25	0
1	20.87	3.00	0.62	0.25	0.25
3	20.37	3.00	0.62	0.25	0.75
5	19.87	3.00	0.62	0.25	1.25
7	19.87	3.00	0.62	0.25	1.75
9	18.87	3.00	0.62	0.25	2.25